AD-A160 385

Modeling of Electromagnetic Scattering from Ships

D. Y. NORTHAM

Advanced Techniques Branch
Tactical Electronic Warfare Division

September 6, 1985

DTIC
ELECTE
S
OCT 2 1 1985
E
D

NAVAL RESEARCH LABORATORY
Washington, D.C.

DTIC FILE COPY

85 10 21 001

SECURITY CLASSIFICATION OF THIS PAGE

AD-A160385

REPORT DOCUMENTATION PAGE

1a REPORT SECURITY CLASSIFICATION UNCLASSIFIED	1b RESTRICTIVE MARKINGS			
2a SECURITY CLASSIFICATION AUTHORITY	3 DISTRIBUTION/AVAILABILITY OF REPORT Approved for public release; distribution unlimited.			
2b DECLASSIFICATION/DOWNGRADING SCHEDULE				
4 PERFORMING ORGANIZATION REPORT NUMBER(S) NRL Report 8887	5 MONITORING ORGANIZATION REPORT NUMBER(S)			

6a NAME OF PERFORMING ORGANIZATION Naval Research Laboratory	6b OFFICE SYMBOL (If applicable) 5750	7a NAME OF MONITORING ORGANIZATION Naval Electronic Systems Command
6c ADDRESS (City, State, and ZIP Code) Washington, D.C. 20375-5000		7b ADDRESS (City, State, and ZIP Code) Washington, D.C. 20360

8a NAME OF FUNDING/SPONSORING ORGANIZATION Naval Electronic Systems Command	8b OFFICE SYMBOL (If applicable) NAVELEX 615	9 PROCUREMENT INSTRUMENT IDENTIFICATION NUMBER		
8c ADDRESS (City, State, and ZIP Code) Washington, D.C. 20360		10 SOURCE OF FUNDING NUMBERS		

PROGRAM ELEMENT NO 62734N	PROJECT NO XF34- 372-100	TASK NO XF34- 372-100	WORK UNIT ACCESSION NO DN880-063

11 TITLE (Include Security Classification)

Modeling of Electromagnetic Scattering from Ships

12 PERSONAL AUTHOR(S)
Northam, Don Y.

13a TYPE OF REPORT Final	13b TIME COVERED FROM 11/81 TO 11/83	14 DATE OF REPORT (Year, Month, Day) 1985 September 6	15 PAGE COUNT 122

16 SUPPLEMENTARY NOTATION

Previously published as a University of Maryland Ph.D. dissertation, 1983

17	COSATI CODES		18 SUBJECT TERMS (Continue on reverse if necessary and identify by block number)
FIELD	GROUP	SUB-GROUP	Radar cross section Distributed target models
			Ship models Glint
			Stochastic models

19 ABSTRACT (Continue on reverse if necessary and identify by block number)

—The purpose of this research is to develop a stochastic model of distributed radar targets, especially ships, that directly incorporate target structure and motion. The model was required to be especially useful as a tool in the stochastic simulation and analysis of tracking-radar signals over time intervals that are short relative to the time constants of the target motion. The model is based on the observation that distributed targets often appear to radars as being composed of several dominant scatterers. A concept (unit-scatterer) is introduced that quantifies this observation and that leads to a useful model of distributed targets. Based on this concept and assuming the presence of over-water multipath, analytical representations of radar cross section and glint are developed, and implications of the small time-interval requirement are investigated. Using these representations, a simulation is developed and used to investigate the stochastic properties of both radar cross section and glint for an example ship target. Simulation outputs are presented and analyzed to illustrate the implications of the model given variations in the significant parameters.

(Continued)

20 DISTRIBUTION/AVAILABILITY OF ABSTRACT ☐ UNCLASSIFIED/UNLIMITED ☒ SAME AS RPT ☐ DTIC USERS	21 ABSTRACT SECURITY CLASSIFICATION UNCLASSIFIED	
22a NAME OF RESPONSIBLE INDIVIDUAL Don Y. Northam	22b TELEPHONE (Include Area Code) (202) 767-3178	22c OFFICE SYMBOL 5753

DD FORM 1473, 84 MAR 　　　83 APR edition may be used until exhausted
All other editions are obsolete

SECURITY CLASSIFICATION OF THIS PAGE

i

19. ABSTRACT (Cont.)

The model was developed to incorporate the major strengths of the existing deterministic and stochastic models: ability to account directly for target structure and motion, and ease of obtaining target-signature time series, respectively. The deterministic models, though precise, are extremely inefficient in generating these time series and require a great deal of information about target structure and motion. The stochastic models do not directly account for target structure and motion and rely heavily on target measurements. The model presented here efficiently generates target-signature time series given information about target structure and motion. The existing deterministic and stochastic models can be viewed as limiting cases of this new model.

Accession For

NTIS GRA&I

DTIC TAB

Unannounced

Justification

By

Distribution/

Availability Codes

Dist | Avail and/or | Special

A-1

CONTENTS

MODELING OF ELECTROMAGNETIC
SCATTERING FROM SHIPS

1. INTRODUCTION

Scattering of electromagnetic (EM) energy has been a subject of interest to the scientific community since the nineteenth century. The first and most extensively studied scattering object has been the sphere. However, very few scattering problems have solutions that are known and exact although many problems have asymptotic solutions [1]. The problems that have been solved have been problems of scattering from simple geometric shapes [1,2]. The modeling of complex targets is an extremely difficult, inexact task [3]; quoting from Ref. 4, "An exact solution to the scattering problem for a complex target is out of the question...."

Most of the interest in EM scattering has come from the field of radar. Radars obtain information about targets by illuminating the target and then measuring the EM field scattered by the target and environment. Radars have been used for this purpose since World War II. Since then their performance capabilities have improved rapidly. Paralleling the improved radar performance has been an increasing need for better understanding of target scattering properties. This need has directed most of the scattering research since World War II. Almost all targets of interest for military and civilian radars have physical dimensions much larger than the radar wave length (scattering in the optical region); that is, they are distributed targets. Clearly, any scattering model that is to be useful in radar applications must be limited in its ability to fully describe target scattering.

Although EM scattering is the phenomenon which makes radars possible, by producing scattered fields for the radar to sense, it is well known that it is only necessary to understand two projections of these fields to predict the performance of most radar systems. These projections are radar cross section (RCS) and glint. RCS represents the apparent size of the target, and glint represents the apparent location, in angle, of the target, as sensed by the radar. Though generally analyzed as separate phenomena, it is well known that RCS and glint are different manifestations of the same target-induced effects. Most of the research on scattering since the development of radar has been directed to understanding RCS and glint rather than scattering per se.

Distributed targets are typically modeled as a finite number of individual, point-source scatterers whose characteristics are determined by the target's structure. (We refer to such models as N-source models.) Both RCS and glint can be represented by using such models. The various N-source models that have arisen differ depending on how the individual scatterers are characterized. Generally, the scatterer characterizations that are made depend on the intended application of the target model. Building on these earlier N-source models, this report develops a new approach to modeling the scattering from ships.

1.1 The Scattering Problem

Practical solutions to the modeling of distributed targets are approximations that range from extremely complex models that describe many aspects of scattering (and are difficult and/or expensive to use) to simple models that ignore many aspects (but are easy and/or inexpensive to use). Each model is developed subject to constraints imposed by application requirements. We remark that no

1

model can completely describe all aspects of a physical phenomenon and very "crude" models are often the most useful; modeling a resistive element in an electric circuit by $E = IR$ is often quite useful though such a model ignores known resistive element dependencies on temperature, power, frequency, etc., and hence is not useful in predicting failure modes, noise properties, etc., of the element.

1.1.1 Scattering Models

The models that have been developed to represent complex target scattering can be described as being one of three types (or a combination thereof): deterministic, statistical, or stochastic. The simplest deterministic model is one where the target is represented as a fixed-position, point-source radiator with constant RCS and no glint. Deterministic scattering solutions for simply shaped objects can often be obtained by using the geometric theory of defraction or physical optics theory. The most complex deterministic models represent the target as a collection of many, simply shaped objects for which scattering solutions exist. The scattered field of the target then becomes the superposition of the scattered fields of the simple objects, where effects such as shadowing, multiple reflections, etc., are appropriately accounted for.

The statistical models are those in which only the first-order statistics of one or more aspects of the scattering, usually RCS, are modeled. These models are usually developed either from measurements of the target or by deriving the statistics from some broad assumption (e.g., that the target is composed of many independent scatterers of approximately equal scattering areas) regarding the target structure. The well-known Swerling models of RCS are examples of this type.

The stochastic models are those that describe the scattered field as a stochastic process. Stochastic processes are useful because they not only specify first-order statistical properties but they also specify higher order fluctuation properties of the target including, at least, the second-order correlation properties (e.g., the correlation function). Correlation properties of the radar's receive signal must be known if an analysis of the tracking performance of the radar is to be made. The stochastic models used for target modeling are usually second-order stochastic models (i.e., they specify the first- and second-order properties of the process) because to date, radars exploit only the first- and second-order properties of their receive signals and because second-order processes are well developed mathematically.

Stochastic models usually are either extensions or combinations of deterministic and/or statistical models. An example of the extension approach is a model that converts the many scatterer deterministic model described above to a stochastic model by describing the target's range and orientation relative to the radar as stochastic processes and then solving the scattering problem as a function of time. An example of a combination model approach is a model that uses measurements that characterize not only the first-order statistics, but also the correlation properties of a target's scattering as a function of radar-target relative motion. The stochastic model is then a stochastic process that is defined to produce the measured statistics as a function of the measured parameters. We refer to such a model as an empirical stochastic model. We note that when the target being modeled is extremely large (e.g., Earth's surface illuminated by the radar, the moon, etc.) the approach of representing the surface as a stochastic process is often used.

1.1.2 Fundamental Constraint

The fundamental constraint imposed in the development of the model presented here is that the model must be useful in the analysis and simulation of the pulse-by-pulse tracking performance of pulse radars. A major implication of this constraint is that the model must be capable of efficiently producing time-series representations of scattered radar-signals. Both empirical stochastic models and deterministic models using many simple scatterers can be applied under this constraint. However, each of these models has serious drawbacks for the desired application. The stochastic model, although very

efficient for simulation purposes, is strongly dependent on actual measured data to provide the needed statistical information, and so extrapolation of such a model without supporting data is questionable. Further, this type of model is usually only weakly connected to the physical process (target-radar relative motion) that is causing the scattered-signal variations. The deterministic model has two major drawbacks. First, such a model requires an enormous amount of detailed information about the actual target to be modeled; the structure of that target's surface must be precisely known. Second, the simulation of such a model usually is extremly time consuming because many exact scattering solutions must be calculated to produce the required time series.

In view of the above, tracking-radar studies and simulations would benefit from a model that is stochastic, that can be efficiently simulated, and that can be parametrized by the fundamental physical properties of target-radar relative motion and "significant" target structure. Such a model would not be as accurate as the deterministic model when the target structure and motion are precisely known, and it might not be as simple and efficient in simulation as the empirical stochastic model when extensive experimental data is available. However, it would incorporate the fundamental simulation efficiency of a stochastic model and much of the physical basis of the deterministic model. We will refer to this type of model as a phenomenological stochastic model.

1.1.3 Statement of the Problem

The objective of this report is to develop a phenomenological stochastic model for the scattering of radar signals from distributed targets using an N-source formulation. The fundamental parameters on which the model is based are target motion and structure. We assume that the target's motion can be characterized as a stochastic process and that the target's approximate structure and dimensions are known.

We further restrict the model by imposing several additional constraints on its applications. The model is intended for use in analyzing the performance of continuous tracking, monostatic, pulse radars that operate at microwave frequencies and track only in range, azimuth, and elevation. The targets of interest are assumed to be large with respect to the radar wavelength, structurally complex, in the radar antenna's far-field, and uniformly (plane wave) illuminated by the radar.

Because of the importance of RCS and glint (and the existence of associated data bases), the model fidelity is to be inferred from the validity of the resulting RCS and glint representations. Validation of any model of scattering from complex targets must, of practical necessity, be statistical. That is, the model must produce a time series of data that can be tested for statistical accuracy relative to measured target data. For the reasons given in Sec. 1.1.1, we require that the model be accurate to second-order statistics; that is, the model must accurately represent the first-order probability density function, the power spectral density function (and equivalently, the autocorrelation function), and associated parameters over intervals where the process is piecewise-stationary. We do not require that the second-order probability density function be specified because that function is difficult to estimate practically and though it more completely specifies the process, it is less useful in characterizing signal time-correlation properties than is the power spectral density.

The primary targets of concern in this report are surface ships. Relative to aircraft modeling, ship modeling has received limited attention in the literature. Ships are much more complex in structure than aircraft and scattering from them is complicated by sea surface multipath. However, the model developed is of a general nature and should be useful in problems where the assumptions made in its development hold.

1.2 Previous Work

Variations in RCS as a function of time (amplitude scintillation) were first observed during World War II [5]. The early models of amplitude scintillation were developed for application in the detection

of aircraft targets beginning with the work of Marcum [6] and Swerling [7,8]. These models represent the target as a point source whose fluctuation statistics are chosen depending on the type of radar used and the measured or assumed fluctuation properties of the target. During the 1960s, numerous papers and books appeared describing various methods of N-source modeling of RCS. The August 1965 issue of the IEEE Proceedings [9] was devoted to radar reflectivity and is a good reference for the early RCS work.

The glint phenomena were not observed until radar angle tracking capabilities improved in the late 1940s. The first models of glint appeared in Mead et al. [10], De Lano [11], and Howard [12] during the 1950s. Each was based on the N-source concept.

We focus our review on models that are based on the N-source concept because that is the concept on which the analysis of this report is based.

1.2.1 Random Models

One method of modeling complex targets has been to represent the target as an N-source model with scatterers whose individual scattering properties are assumed to be random. When simple random properties are assumed, this type of model allows an analytical solution to be obtained for the target scattering. This method was used by Muchmore [13,14] to describe the RCS of aircraft and reasonable spectral estimates, relative to measured data, were obtained. However, as pointed out by Peters and Weimer [15-17], this method has serious drawbacks when used to analyze radar tracking performance. This is because over short time and aspect intervals the individual scatterers do not behave independently.

This random method was used, for arbitrary complex targets, by De Lano [11], Gubonin [18], and Mumford [19] to study glint statistics; by Mohanty [20], Gruner [21], and Mitchell [22,23] to study RCS statistics; and by Varshavchik [24] and Borden [25] to study the combined RCS-glint problem. Baras [26] used an N-source representation of the target to obtain the fundamental parameters of an equivalent-point-source model of glint.

Jakeman [27,28] and Jakeman and Pusey [29-32] have investigated using K-distributions [27] to describe the amplitude statistics of scattered radiation in a variety of experiments involving scattering from turbulent media (e.g., sea clutter and optical scintillation). This K-distribution model arises when it is assumed not only that the individual sources' amplitudes and phases are independent random variables but also that the number of sources is a random variable.

1.2.2 Deterministic Models

The most common type of model of complex targets based on the N-source concept assumes that the target is composed of scatterers with simple geometric shape for which scattering solutions are known. The field scattered by the target is then the sum of the individual scattered fields for the given radar-target geometry. Physical optics theory, the geometric theory of diffraction, integral equation methods, and combinations thereof are used to obtain scattering solutions for the component scatterers. Discussions of these methods can be found in many papers and books; examples are Crispin and Siegel [33], Bechtel and Ross [34], Bowman et al. [35], Ruck et al. [36], Keller [37], and Oshiro et al. [38,39]. Many examples of aircraft and missile modeling are contained in or referred to by the previous references. Examples of ship models using this approach are given by Toothman [40] and Radza and Stenger [41]. We note that in modeling ships, thousands of scatterers are often required and usually up to twenty generic types of scatterers are used. Further, multipath effects on each scatterer and multiple scattering must be accounted for.

The major studies of glint have been performed without assigning specific properties to the individual scattered fields. This approach has led to generic representations for glint. Howard [12] used this approach to show that glint was equivalent to the slope of the phase front of the reflected field in the radar angular coordinate of interest. Lindsay [42] expanded the concept of phase-front slope to phase-front gradient. He also showed the relationship between glint and Doppler scintillation. Dunn and Howard [43] showed that glint was equivalent to Poynting vector tilt and, independent [5] of Lindsay, showed the relationship between glint and Doppler scintillation.

1.2.3 Unified Scattering Models

Very few attempts have been made to develop a unified RCS and glint model for the time-varying return from a complex target. The geometric models described above can be used to generate time series of data by moving the target randomly and solving for the scattered field as a function of time. Such a procedure is of course extremely time consuming even on a computer, especially for ships. Wright and Haddad [5] developed such a model for an airborne drone where the individual scatterers were represented as ellipsoids. Both RCS and two-dimensional glint were modeled. The stochastic returns from several target aspects were obtained and analyzed, assuming appropriate random motion of the drone. Borden [25] developed a random model for the unified target return of an aircraft, assuming only one-dimensional glint. He modeled the target as N sources and then assigned statistical values to the individual scatterer amplitudes, phases, and Doppler frequencies. Varshavchik [24] investigated the relationship between the amplitude and phase characteristics of targets composed of an array of identical isotropic scatterers. He studied returns resulting from small angle-oscillations of the target in a fixed plane.

1.2.4 Multipath Models

Low grazing-angle, forward-scatter, over-water multipath has been studied extensively during the past quarter century. The most common representation of such scattering has been made in terms of equivalent-point-source models where the scattered field is viewed as being composed of two components: a "specular" (or "coherent") component that is deterministic, and a "diffuse" (or "incoherent") component that is random. Although it is well known that the specular component appears to a radar as coming from a point-source that is located at the geometric image of the transmitting point-source, the apparent point-source location(s) of the diffuse component(s) is not well understood. This lack of understanding has caused difficulty in analyzing the tracking errors induced by diffuse multipath [44,45].

In a series of papers, Beard et al. [46-48] developed a second-order, statistical model of the scattered field. The model is based on empirical measurements and the fundamental parameters are diffuse and specular scattering-coefficients. Beard's model is valid in the sense of predicting the received power at microwave frequencies. It implicitly assumes that the diffuse scattering can be viewed as coming from a point-source located at the specular point. Northam [49] presents a second-order stochastic model, based on this work, that is useful for simulating multipath effects as a function of time. Beckmann and Spizzichino [50] theoretically predicted that the diffuse scattering arose primarily from surface areas near the transmitter and near the receiver. Barton [51] modified the diffuse coefficient that was derived by Beckmann and Spizzichino with a roughness factor and formulated the coefficient in terms of a bistatic scattering parameter for the surface. He showed that diffuse scattering arose from surface areas that vary as a function of geometry and surface structure. Mrstik and Smith [44] investigated the limitations caused by multipath on low-angle tracking using four different models of the poorly understood bistatic scattering parameter. Smith and Mrstik [45] investigated multipath-induced tracking errors in elevation scanning and monopulse radars by assuming that the diffuse tracking errors are small so that the diffuse power can be viewed as a noise-like interference superimposed on the direct-path signal. Baras [52] has summarized the various models from the perspective of stochastic modeling.

2. SUMMARY

This report addresses the modeling of the effects of electromagnetic scattering from complex, distributed targets in a multipath environment. The basic objectives are to develop a scattering model that is useful in analyzing and simulating the correlated processes of RCS and glint, and to develop the equations of these processes appropriate to that model. The model is specifically intended to be useful for studying the tracking performance of pulse-radars. Ships are the major targets of interest. We are primarily concerned with representing scattering over short-time intervals. A digital simulation is developed, and some implications of results from that simulation are discussed.

2.1 Approach

Our approach is to use a (largely) deterministic model for the target scattering and a stochastic model of the target's motion. Using the target's motion as input we obtain a stochastic representation of the received field. Over-water multipath effects are also modeled as stochastic processes.

We model the target as a finite collection of point-source scatterers that represent the dominant scattering components of the target. These "unit-scatterers" are defined to allow a straightforward representation of the received field at the radar. Because the target is represented as a collection of point-source scatterers, we draw on existing models of RCS and glint that were developed assuming point-source scattering. A simulation of correlated RCS and glint is developed for use in studying the effects of model-parameter variations.

2.2 Outline

The concept of unit-scatterer is introduced in Section 3, and an analytic representation of the concept is presented. Methods of identifying and measuring the target's component unit-scatterers are proposed and anticipated properties of the associated amplitudes and phases are discussed.

In Section 4, the usual model of the received field from a collection of point-source scatterers is presented, and for completeness a model of a generic radar system is developed in the context of point-source scatterers. A point-source multipath model is then incorporated into the equation that represents the received field.

The motion equations for the individual unit-scatterers of a ship are derived in Section 5. For completeness, two formulations of these equations are made, each assuming different inputs: the first assumes knowledge of the driving forces and moments that are applied to the ship; the second assumes a frequency-response model of the ship motion.

Section 6 describes a ship-motion simulation that we developed as the stochastic input to the scattering simulation. It is based on the cataloged ship-motion data generated by the David Taylor Naval Ship Research and Development Center (DTNSRDC) using frequency-response models for the ship motions.

In Section 7, equations for RCS are developed in terms of unit-scatterers based on the formulations of Section 4. Because tracking radars process data over short time-intervals, RCS variations over such intervals are analyzed, and the nonstationarity of the resulting processes is illustrated.

In Section 8, two approaches to glint modeling are used to develop correlated azimuth and evaluation glint models for targets that are modeled by unit-scatterers. It is shown that one approach is more useful than the other, especially when point-source multipath effects are included.

Section 9 presents the results of simulation studies. The effects of varying some of the model parameters are investigated.

6

3. THE UNIT-SCATTERER CONCEPT

As described in Section 1, one of the most common approaches to modeling complex targets is to represent them as being comprised of a finite number of point-source scatterers. Using this approach, various scattering models have been developed. The differences in these models are due to the different ways in which the scatterers are characterized. We use this approach but attempt to minimize the number of scatterers and the statistical assumptions made regarding the parameters of those scatterers.

Determining the characteristic parameters of a scatterer given the incident and scattered fields is referred to as an inverse scattering problem. Recent years have seen a rapid growth of interest in such problems in many areas of science, especially in optics and electromagnetics; however, for the EM inverse problem, "the prospects of expressing scattering characteristics of complex shapes successfully and simply are still inadequate" [53].

3.1 Scattering Matrix

When an object is illuminated by a plane wave (implied by large radar-to-scatterer range), the scattered field, $\vec{E}^s$, can be viewed as a linear transformation of the incident field, $\vec{E}^i$. The matrix representation of this transformation is called a scattering matrix [33]. Such matrices have the form

$$S = \begin{bmatrix} S_{11} \exp{(j\psi_{11})} & S_{12} \exp{(j\psi_{12})} \\ S_{21} \exp{(j\psi_{21})} & S_{22} \exp{(j\psi_{22})} \end{bmatrix}. \tag{3.1}$$

(We note that due to phase being relative, the conservation of energy principle, and the reciprocity theorem, only five of the eight parameters of S need to be determined to completely specify S [54].) The scattered field representation is

$$\vec{E}^s = S\vec{E}^i. \tag{3.2}$$

The scattering matrix provides a significant characterization of radar targets; knowledge of it for a given set of radar parameters allows a complete characterization of the target's RCS for those parameters. Further, the scattering matrix for any polarization pair can be obtained from the matrix expressed in terms of any two arbitrary polarization vectors that are orthogonal [33]. As emphasized by Boerner [53] in his paper discussing the utilization of polarization in the EM inverse scattering problem, when measuring target scattering all components of the scattering matrix should be estimated or a loss of information will result.

Given a radar with receiver polarization $\hat{p}_R$, the RCS of the object can be defined to be [54]

$$\sigma = \lim_{r \to \infty} 4\pi r^2 \left(\frac{\vec{E}^s \cdot \hat{p}_R}{|\vec{E}^i|} \right)^2$$

$$\tag{3.3}$$

$$= \lim_{r \to \infty} 4\pi r^2 \left(\frac{S\vec{E}^i \cdot \hat{p}_R}{|\vec{E}^i|} \right)^2,$$

where r is the target-to-radar range. If the transmitter has the polarization $\hat{p}_T$, then we can write $\vec{E}^i = |\vec{E}^i|\hat{p}_T$ and

$$\sigma = \lim_{r \to \infty} 4\pi r^2 (S\hat{p}_T \cdot \hat{p}_R)^2. \tag{3.4}$$

7

In general, polarizations are defined in terms of horizontal and vertical unit vectors, $\hat{p}(H)$ and $\hat{p}(V)$. Using these polarizations, we write the scattering matrix as

$$S = \begin{bmatrix} S(HH) & S(HV) \\ S(VH) & S(VV) \end{bmatrix}. \tag{3.5}$$

It follows from Eqs. (3.4) and (3.5) that there are four fundamental components that characterize the RCS of scattering objects; they are

$$\sigma(IJ) = \lim_{r \to \infty} 4\pi r^2 |S(IJ)|^2, \quad I, J = H, V. \tag{3.6}$$

Therefore, the RCS of an object can be described by the matrix

$$\Sigma = \begin{bmatrix} \sigma(HH) & \sigma(HV) \\ \sigma(VH) & \sigma(VV) \end{bmatrix}. \tag{3.7}$$

The above concept of scattering can be extended to targets composed of individual scatterers for which scattering matrices are known. The procedure is to sum the components of the individual scattering matrices to yield a target scattering matrix; relative phasing and multiple scattering between the scatterers must, of course, be taken into account. The target RCS can then be determined from the resulting matrix. However, the complexity of this procedure, due to the relative phasing, has led to the use of two assumptions to simplify the problem. Because an average value of RCS is often all that is required to be known about the target, it is often assumed that the individual scatterers are phase independent. This allows a straightforward estimate of the RCS (cross products of independent phases cancel). Second, because most radars operate using only one polarization, it is often assumed that the three scattering components associated with the orthogonal polarization can be ignored. Both of these assumptions have proved quite useful for practical problems.

3.2 Definition

It is well known that complex targets produce scattering that appears to result from several apparent "sources" ("dominant scatterers," "bright spots," "hot spots," and "flare spots") that are located at "scattering centers." The number, amplitude, and phase of these sources vary with target aspect and radar frequency, polarization, and resolution. Examples of this phenomenon for measured targets can be found in Refs. 55 through 59. These apparent sources result because scattering arises not from the target's entire surface but from points of discontinuity and specular points of that surface; cancellation of the field occurs along continuously varying surfaces of the target [34]. Kell [60] refers to the portion of the target surface that is near a scattering-center and that produces the return associated with that scattering-center as the "cophased area." The scattering-centers are not necessarily due to specific geometric objects; they may arise from phasing between adjacent objects whose returns, when summed incoherently, would not be significant [34]. This phenomenon may lead to scattering-centers that are not located on the target.

In light of the above, we define a unit-scatterer (US) to be an apparent point-source scatterer as perceived by a radar. Clearly, the definition is radar dependent; such objects depend directly on radar frequency and pulse width. We characterize a US by a complex amplitude-matrix, X. Our definition of this matrix is analogous to that of the scattering matrix:

$$X \triangleq \begin{bmatrix} A_{11} \exp{(j\phi_{11})} & A_{12} \exp{(j\phi_{12})} \\ A_{21} \exp{(j\phi_{21})} & A_{22} \exp{(j\phi_{22})} \end{bmatrix} \tag{3.8a}$$

where

$$A_{ij} = \sigma_{ij}^{1/2} = (\lim_{r \to \infty} 4\pi r^2 |S_{ij}|^2)^{1/2}. \tag{3.8b}$$

The amplitudes and phases are functions of US orientation, and the phase is also a function of radar-US range. The amplitude functions, A_{ij}, are the square roots of the associated component RCSs. The phase functions, ϕ_{ij}, are defined relative to some reference point on the radar-to-target sight line; this allows coherent summing of the matrices that represent the target. For the standard polarizations, Eq. (3.8a) becomes

$$X = \begin{bmatrix} A_{HH} \exp{(j\phi_{HH})} & A_{HV} \exp{(j\phi_{HV})} \\ A_{VH} \exp{(j\phi_{VH})} & A_{VV} \exp{(j\phi_{VV})} \end{bmatrix}. \tag{3.9}$$

The RCS of a US that is characterized by X becomes

$$\sigma = |\hat{p}_T^T X \hat{p}_R|^2 \tag{3.10a}$$

where $\hat{p}_T$ is the transmitter polarization and $\hat{p}_R$ is the receiver polarization. For a target composed of N USs,

$$\sigma = \left| \sum_{i=1}^{N} \hat{p}_T^T X_i \hat{p}_R \right|^2. \tag{3.10b}$$

The significance of X is that the electric field at the receiver antenna and associated received signals can be written (see Section 4) in terms of a scattering function $\Gamma(\cdot, \cdot)$ which we define by

$$\Gamma(\hat{p}_T, \hat{p}_R) \triangleq \hat{p}_T^T \left[\sum_{i=1}^{N} X_i \right] \hat{p}_R. \tag{3.11}$$

Although this approach to modeling scattering is not unique (similar formulations to obtain RCS and glint are implicit in other work), the definition of the unit-scatterer is new in that it is based on the fundamental scattering objects being large, complex, and not necessarily physically identifiable.

Because of the complexity of USs comprising large targets, such as ships, it is likely that experimental methods or detailed simulation studies are necessary to accurately determine the X_i matrices. However, as is discussed in Sec. 3.4, relatively simple representations of the USs may yield good approximations to the components of X_i.

3.3 Identification

Given the above definition of the US we now discuss methods of identifying the USs on complex targets. There are two basic approaches to US identification (and characterization): using analytic or experimental methods. We first consider several analytic methods.

Kell [60] investigated bistatic RCS using the N-source formulation. In this and the next paragraph, we discuss that work as it relates to the monostatic problem. Using the Straton-Chu integral in the definition of RCS, he showed that a target's bistatic RCS could be written in the form

$$\sigma = \frac{\pi}{\lambda^2} \left| \int I(z) e^{j2k_0 z \cos\beta/2} dz \right|^2 \tag{3.12}$$

where

$\quad k_0 \quad$ is the wavenumber of the incident field,

$\quad \beta \quad$ is the bistatic angle, and

$\quad \lambda \quad$ is the radar's wavelength.

Although Eq. (3.1) is an exact expression, the difficulty with using it is that $I(z)$ is rarely known precisely [60]. However, the analytic continuity of $I(z)$ allows it to be divided into a sum of integrals over subregions of the target and "reasonable approximations" to $I(z)$ lead to contributions from these integrals only near the end points of each integral [60]. These contributions are then identified as the scattering centers. He distinguishes between two types of scattering-centers: "simple centers," which result from direct illumination only, and "reflex centers," which result from multiple reflections. He states that it is common for reflex scatterers to produce much larger RCS values than simple scatterers do.

Once the sources are identified, the target RCS can be written as a finite sum of those sources. Kell shows that in terms of N sources, the bistatic RCS can be expressed as (assuming fixed polarizations)

$$\sigma = \left| \sum_{i=1}^{N} \sqrt{\sigma_i} \; e^{j\phi_i} \right|^2 \qquad (3.13a)$$

with

$$\phi_i = 2k_0 r_i \cos \frac{\beta}{2} + \xi_i, \qquad (3.13b)$$

where

r_i is the distance between the ith and first sources' phase-centers, projected on the bistatic axis, and

ξ_i is the "residual phase contributions" of the ith center.

Setting $\beta = 0$ yields the monostatic RCS. (We note that to derive the monostatic-bistatic equivalence theorem in Ref. 60, Kell assumes that the ξ_i do not vary over the range of β considered; we suggest that for USs arising from structurally complex objects, the ξ_i may vary significantly as a function of the monostatic aspect angle.)

When the magnetic field $\vec{H}$ on the surface of a perfectly conducting object is known and the field point is at a large distance from the body, the scattered magnetic field, $\vec{H}^s$, can be approximated by [61]

$$\vec{H}^s \approx \frac{jke^{jkR}}{4\pi R} \int_{S'} (\hat{n} \times \vec{H}) \times \hat{r} e^{-jk\hat{r} \cdot \vec{r}'} \, dS', \qquad (3.14)$$

where $\hat{n}$ is the outward normal to the surface, $k = 2\pi/\lambda$, $\hat{r}$ is the unit vector from the origin to the field point, R is the distance from the origin to the field point, S' is the scattering object's surface, and $\vec{r}'$ is the radius vector from the origin to the integration point on the surface. To solve Eq. (3.14) we must know $\vec{H}$ and S'. Although obtaining S' for a known object is straightforward, though perhaps tedious, determining $\vec{H}$ for an arbitrarily shaped object is in general not feasible. However, for objects that are relatively smooth (large radii of curvature relative to the radar's wavelength), it is well known that the Kirchhoff (physical optics) approximation (i.e., assume that the surface current density is $-2\hat{n} \times \vec{H}^i$ where $\vec{H}^i$ is the incident magnetic field) leads to an accurate description of the scattered field. Assuming an incident field of the form

$$\vec{H}^i = \frac{E_0}{\eta} \, (\hat{r} \times \hat{e}) e^{-jk\hat{r} \cdot \vec{r}'} \qquad (3.15)$$

where $\hat{e}$ is the polarization direction for the incident electric field $\vec{E}^i$, η is the characteristic impedance of free space, and $E_0 = |\vec{E}^i|$, the scattered electric field can be approximated by

$$\vec{E}^s \approx \frac{jke^{jkR}}{2\pi R} \int_{S'} \frac{E_0}{\eta} [\hat{n} \times (\hat{r} \times \hat{e})] \times \hat{r} e^{-2jk\hat{r} \cdot \vec{r}'} \, dS'. \qquad (3.16)$$

If the surface can be separated into N independent (no multiple scattering) surfaces for which solutions to Eq. (3.16) can be obtained, then the object's scattered field can be described by the sum of N fields (due to the N "elementary" scatterers). In general, N will be large and multiple scattering cannot be ignored so that the resulting scattering model will be very complicated (see e.g., Ref. 40). Scattering centers for complex objects will arise from one of two situations: the return from an elementary scatterer dominates (in magnitude) the return from most of the other elementary scatterers, or several elementary scatterers produce scattered fields that add in phase yielding a total field that dominates most of the other returns. However, if we cannot make the above separation but we can represent the (known) surface in cartesian coordinates by

$$z = f(x, y) \qquad (3.17)$$

so that

$$\vec{r}' = x\hat{i} + y\hat{j} + f(x, y)\hat{k}, \qquad (3.18)$$

we can apply the method of stationary phase to the integral in Eq. (3.16) if we can find the points on the surface where

$$\frac{\partial}{\partial x} (\hat{r} \cdot \vec{r}') = \frac{\partial}{\partial y} (\hat{r} \cdot \vec{r}') = 0. \qquad (3.19)$$

The method of stationary phase is an asymptotic expansion technique for evaluating integrals of the form

$$I(x) = \int_{\alpha}^{\beta} g(z) e^{jxh(z)} \, dz, \qquad (3.20)$$

where x is a large positive parameter and $h(z)$ is a real function of the real variable z [62]. The major contribution to the integral arises from the immediate vicinity of the end points, and at stationary points of $h(z)$ (points where $h'(z) = 0$) and in the first approximation, the contribution of the stationary points is more important than the contribution of the end points [62]. If $z, i = 1, \dots, n$ are the points of stationary phase (i.e., where $h(z)$ has extrema), then the integral Eq. (3.16) can be approximated by

$$I(x) \approx \sum_{i=1}^{N} \int_{z_i - \epsilon}^{z_i + \epsilon} g(z) e^{jxh(z)} \, dz \qquad (3.21)$$

where the ϵ_i are small. The ith element of the summation is evaluated by expanding $h(z)$ about z. The method applies to the integral Eq. (3.16) since for wavelengths of interest to us, $2k$ is large (on the order of 400).

Kodis [63] investigated the scattering from a random, perfectly conducting irregular surface whose radii of curvature are continuous and large. Evaluating the scattered-field integral by using the method of stationary phase, he showed that to a first approximation the RCS of the surface is proportional to the average number of specular points which are illuminated. Although he assumed that there was no multiple scattering, implying that the principal radii of the surface have a lower bound that is much greater than the wavelength of the scattered radiation [63], his results also suggest that the scattered-field integral can be approximated by a finite sum and that the method of stationary phase may prove useful in identifying scattering centers of objects that are relatively smooth.

The method of stationary phase is of interest because it identifies scattering centers on the scattering object. When the method can be used we anticipate that the scattering centers identified by it will be USs of the object. The method may yield not only US locations but also analytic representations for those USs; by investigating the scattered field at these points, we may be able to develop analytic representations for USs resulting from "smooth surface" scattering. Examining the structure of ships we see that in general their surfaces are not smooth. In fact there are many flat surfaces connected at right

11

angles (zero radius of curvature). Therefore the method of stationary phase will not in general be useful for identifying USs on targets such as ships. However, the method may prove useful for targets, such as aircraft, whose surfaces are, in general, "smooth."

Precise identification of the USs for a specific target will most likely require actual target measurements. Such measurements must be made by some type of high resolution radar. Possibilities include narrow pulse radar, pulse compression radar, synthetic aperture radar (SAR), and inverse synthetic aperture radar (ISAR). Such radars must measure, as a function of target aspect, the return signal from the target in cells that are small relative to the target's largest dimension. Although our studies will show that even large ship targets can be well represented at a given aspect by as few as six USs, we suggest a cell size at least as small as 1/10 to 1/20 of the target's largest dimension. The cell size cannot be too small because for studies of radars with less resolution than the measured data, the smaller scatterers can be grouped (summed coherently or incoherently) to produce USs appropriate for the desired resolution. High resolution data exists on many targets including ships but analysis of that data has not been done as part of this research; the effort required to obtain and analyze such data is beyond the scope of this report. High resolution radars identify scatterers in range and amplitude for the associated radar-to-target aspect. Figure 3.1 illustrates such a range profile for an aircraft model; for this aspect (nose-on) there are five dominant scatterers. By rotating the target or moving the radar, the amplitudes, relative phases, and position of the dominant scatterers can be determined as a function of aspect. Care must be taken to vary the aspect by increments small enough to yield accurate (smooth) representations of these parameters. Figure 3.2 illustrates scatterer data as a function of aspect for a simple target.
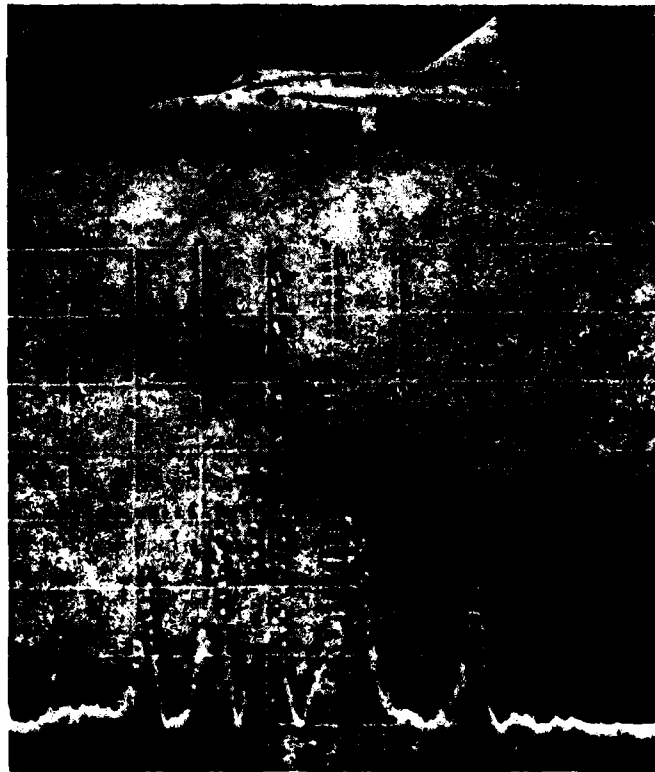

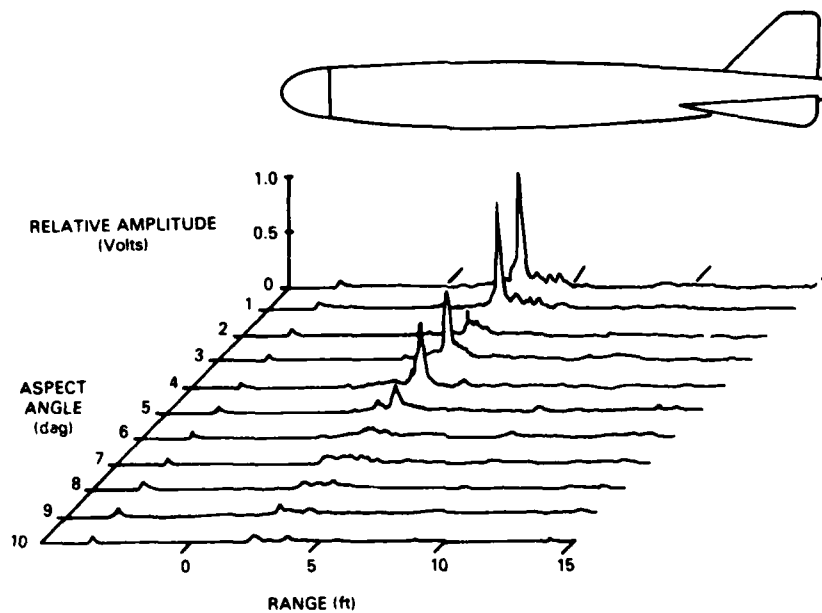Fig. 3.1 — A high range-resolution radar's output (from Ref. 64)

Fig. 3.2 — Amplitude-position data for a high range-resolution radar as a
function of aspect (from Ref. 65)

Another method of identifying the USs is to use existing geometric-model simulations. (Various organizations, including the Naval Research Laboratory (NRL), Georgia Institute of Technology, Technology Services Corporation, and Rockwell International, have developed such simulations.) This method involves running such a simulation for the target of interest and for the desired radar-target geometry. The resulting scattered field would then be examined to identify the major scatterers (say, those that contribute 95% of the total return) and then grouped as appropriate into USs. Similarly, SAR or ISAR simulations could also be used to determine the USs. Figure 3.3 is an illustration of the resulting SAR image from a simulation of a KC-135 aircraft for various SAR resolutions. The "blobs" in these images are candidate USs.

A less accurate but very simple method of identifying some USs is to examine geometric images of the target (photographs, line drawings, blueprints, etc.). This method is useful because scattering from certain generic objects is known. For example, Table 3.1 lists the 22 objects used by Toothman [40] in a geometric type of simulation of ship scattering. An examination of the structure of ships shows that there often are obvious generic scatterers whose dimensions are such that they will dominate the scattering from the ship at specific aspect angles. For example, the broadside and stern aspects of the DD963 (Fig. 3.4) illustrate the presence of flat-plate scatterers in the superstructure. The aft-quarter aspects indicate the presence of large corner reflectors and the two exhaust stacks should have reflections that are analogous to those from cylinders. Using these observations we can obtain a set of USs that, to first-order, approximate the actual USs for a given aspect. This is the method that we will use to obtain USs for the simulation (Section 9). In the next two sections we discuss in some detail the application of this method to obtain US amplitude and phase characterizations.

3.4 Amplitude

The measurement and simulation procedures of the previous section yield amplitude information and can be used to determine the amplitude functions. The visual method, however, does not allow such an accurate determination except for obvious geometric objects. For analysis and simulation purposes we would like to obtain closed form expressions for the amplitude functions. Such expressions,

RANGE

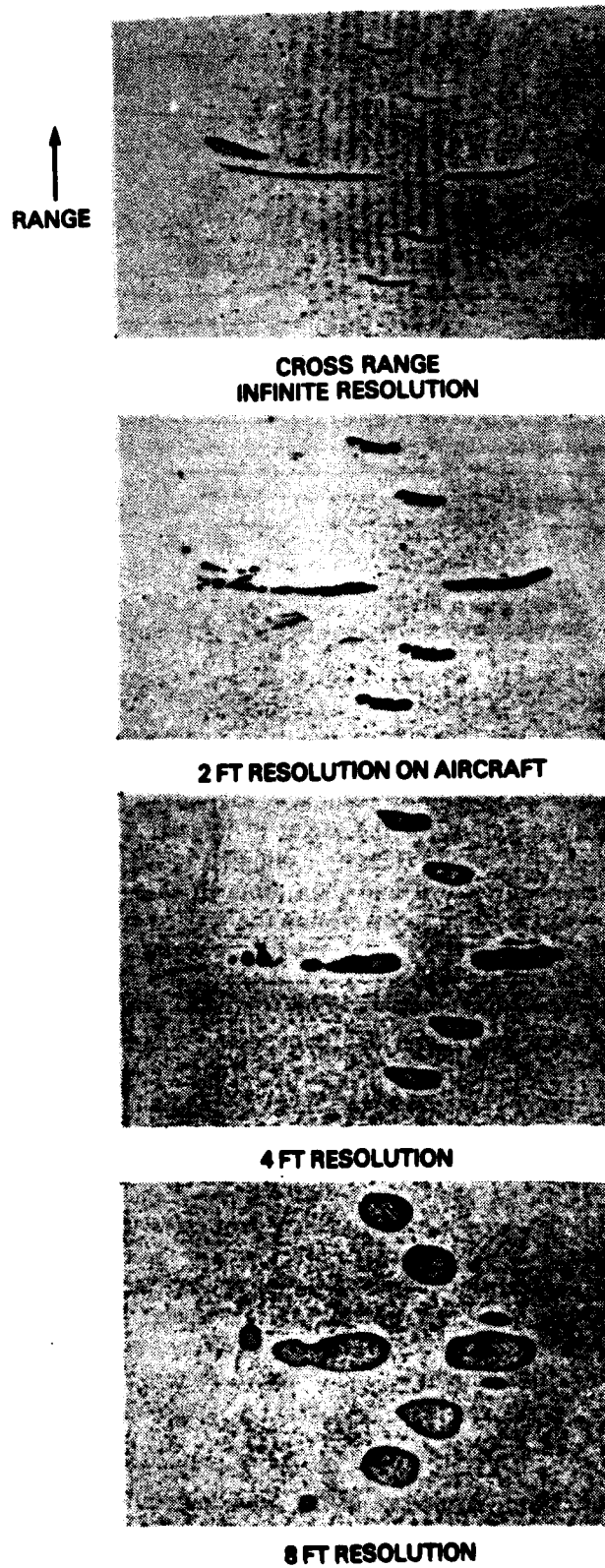**CROSS RANGE
INFINITE RESOLUTION**

2 FT RESOLUTION ON AIRCRAFT

4 FT RESOLUTION

8 FT RESOLUTION

Fig. 3.3 — Simulated SAR images for a KC-135 aircraft
for various resolutions (from Ref. 66)

14

Fig. 3.4 — The DD963 (from Ref. 67)

15

Table 3.1 — Generic Scattering Types
Used by Toothman [40]

Concave Edge	Rectangular Plate
Convex Edge	Paraboloid
Edge Caustic	Ogive
Elliptic Disc	Point
Ellipsoid	Concave Dihedral (2 reflections)
Hyperboloid	Concave Trihedral (3 reflections)
Cylinder	Straight Edge (convex dihedral)
Elliptic Cone	Convex Trihedral (3 plane tip)
Inner Torus	General Curved Surface Specular
Outer Torus	Cavities
Elliptic Tip	Antennas

if accurate, would allow the US model to be more useful in general; the model would not be dependent on detailed information about the target. Therefore, our goal in specifying the amplitudes is to obtain simple, visually identifiable, closed form expressions that are valid over short time-intervals. To achieve this we rely on optical scattering theories and RCS measurements of distributed targets to guide our choice of amplitude functions.

It is well known that the spectrum of the RCS of a distributed target is band-limited and it is often characterized as being low-pass. This implies that a finite (though perhaps large) number of scatterers can be used to accurately approximate the RCS. It is also known that for most targets, due to radar-target relative motion, the target RCS is not a stationary process because the mean, variance, density type, and spectral properties all vary with aspect as indicated by Figs. 3.5, 3.6, and 3.7. The most obvious implication of this is that some of the target's component scatterers have amplitude patterns that vary significantly with aspect. Visual examination of ship structures, for example, finds obvious flat plates, dihedrals, trihedrals, etc. The RCSs of such generic objects have been calculated theoretically and are well known. The flat plate RCS, for example, is strongly dependent on plate orientation; it varies dramatically near vertical incidence where a very large RCS relative to its physical size is generated [70].

Mitchell [23] has suggested that there are only four basic scattering mechanisms within a radar resolution cell. To describe these mechanisms, he defines four basic scattering elements; he claims that for simulation purposes, they describe all scattering effects. The basic elements are:

1. rough surface (diffuse scattering),

2. point source (sphere and dihedral corner),

3. flat plate (specular scattering), and

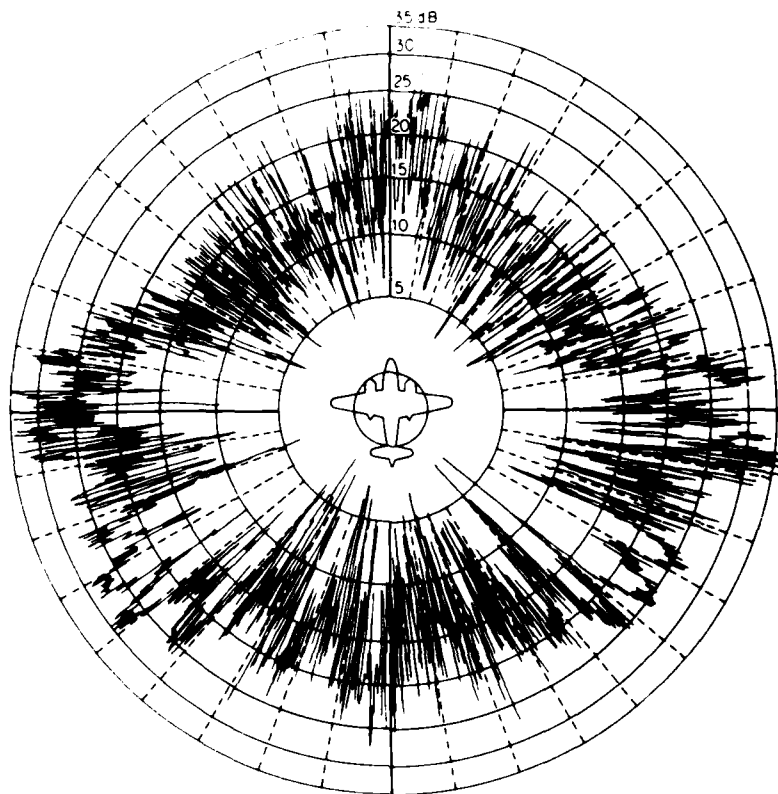4. line source (edge, dihedral corner, thin cylinder, and wire).

Fig. 3.5 — Measured RCS at 10-cm wavelength of a B-26 aircraft
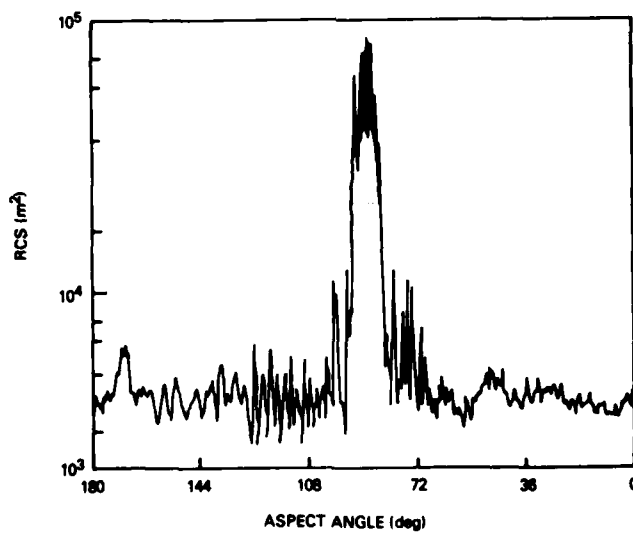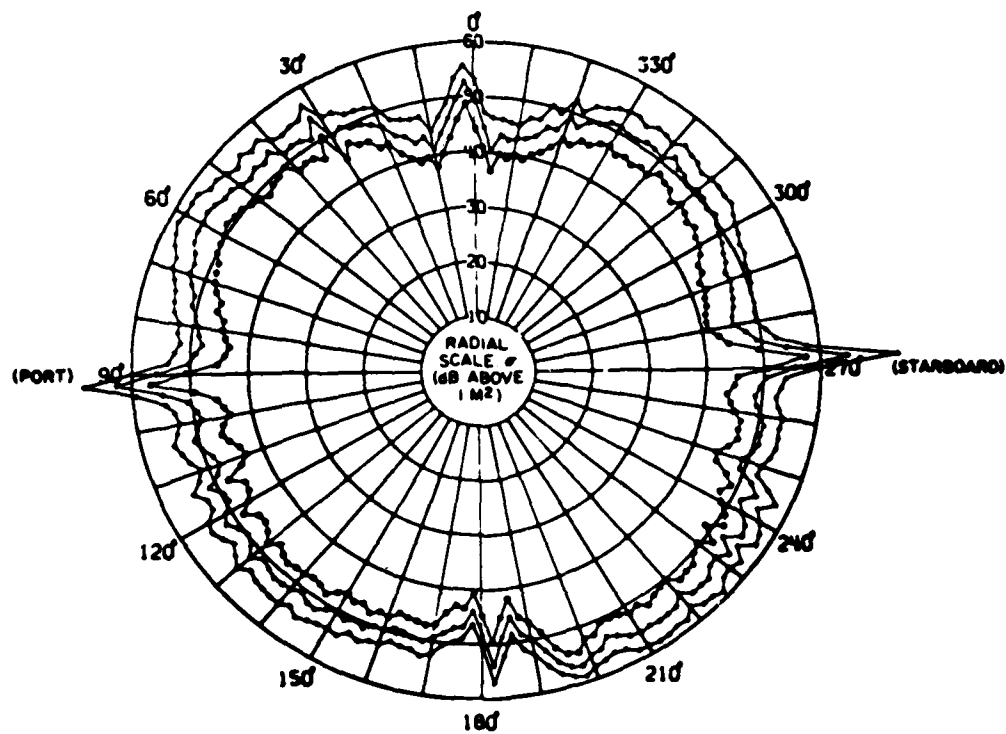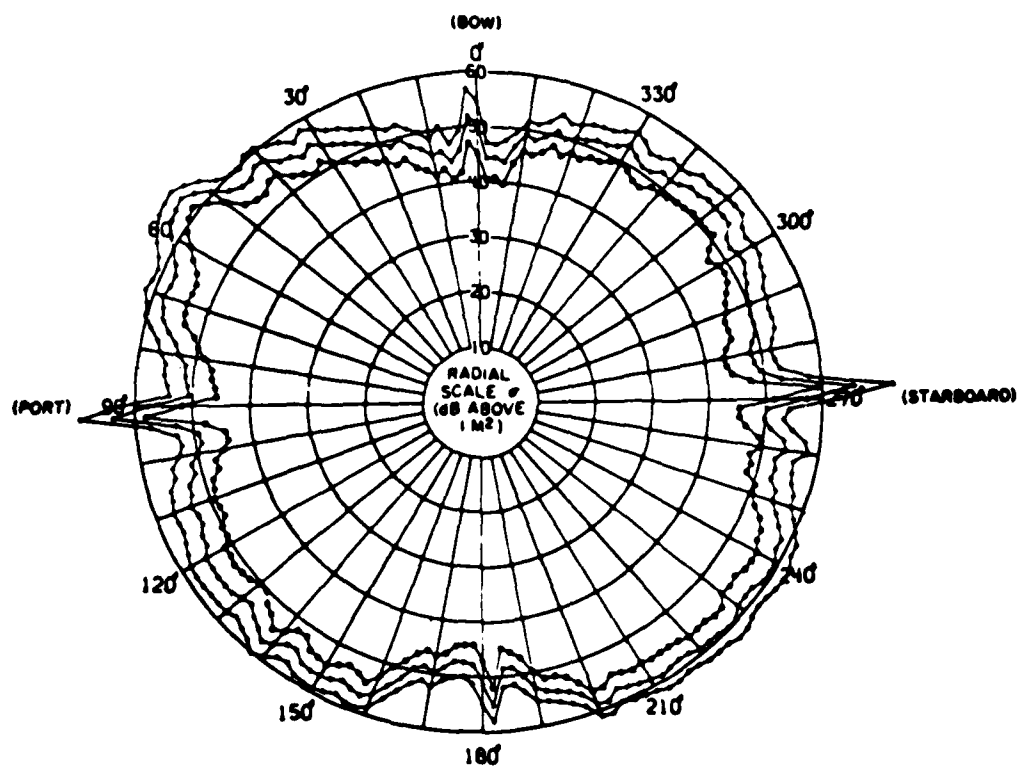as a function of aspect (from Ref. 68)

Fig. 3.6 — Measured RCS at 200 MHz for a scale model of a destroyer (from Ref. 69)

(a)

(b)

Fig. 3 7 — Variation of the 20, 50, and 80 percentiles for an auxiliary ship as a function of
aspect for (a) S-band and (b) X-band (from Ref. 68)

18

In view of this, we propose using a small set of generic functions to model the amplitude functions of the USs. This set may vary depending on the type of target being modeled. For example, ship models would tend to include flat sided scatterer types (plates, dihedrals, ..ihedrals, etc.) whereas aircraft models would tend to include curved surface scatterer types (ogive, paraboloid, etc.).

In the simulations (Section 9), we model the US amplitude functions using only three generic scattering types: sphere, flat plate, and corner reflector. These types were chosen because they represent, to first order, the most obvious scattering effects and they are consistent with the fundamental set proposed by Mitchell. The fidelity of the model by using only these types of scatterers must be determined relative to measured data which we do not have access to for this report.

The sphere type was chosen to represent scattering that is specular but is also significant (in amplitude) over a wide angle of illumination. We model the amplitude of such a scatterer as being proportional to the projected area of the object as viewed by the radar, as it is (in the optical limit) for a sphere [33].

To represent scattering that is specular and highly directional, in analogy with the equation for the RCS of a flat plate near specular incidence we suggest the representation

$$A = \frac{2\sqrt{\pi}}{\lambda} ab \left[\frac{\sin^{\cdot}(2\pi a \sin \theta)}{2\pi a \sin \theta} \cdot \frac{\sin (2\pi b \sin \phi)}{2\pi b \sin \phi} \right]^{1/2}, \tag{3.22}$$

where a and b are the plate dimensions and θ and ϕ are azimuth and elevation angles between the plate and the radar-to-US sight line and a line perpendicular to the flat surface. We anticipate that this type of US will be realized by actual flat plates which for a ship appear primarily at the bow, stern, and broadside aspects. Unlike the sphere type of US, this type is frequency dependent.

The corner-reflector type was chosen to represent frequency-dependent scattering that is nonspecular. This type of scattering results from multiple reflections [61]. We model the associated amplitude by the ratio of the US's projected area to the radar wavelength. This is analogous to the equation for the maximum RCS of a corner reflector,

$$\sigma_{max} = \frac{4\pi a^2}{\lambda^2} \tag{3.23}$$

where a is the area of the reflector's aperture [61].

3.5 Phase

For a point-source scatterer located at some position $\bar{R}$ relative to the radar, the phase of the scattered field at the radar results from the properties of and the range to the scatterer. For a sphere the phase varies as the range to the sphere's center varies but is constant with sphere orientation. However, for nonspherical objects, the phase depends not only on some location point for the object (say, its geometrical center) but also on the object's orientation. This is because as the object rotates, scattering from components of the object (edges, protrusions, etc.) vary as a function of aspect. This apparent point-source location of the object is called the object's scattering center. Aggregating several physical objects may create a US of substantial physical size relative to the radar wave length. As such a scatterer rotates, the scattering-center location may vary rapidly for the wave lengths of interest in this report (on the order of a few centimeters). Therefore, the US phases (the ϕ_{ij} in Eq. (3.8a)) are defined as the apparent location of the US's scattering center relative to some fixed point on the US, as a function of orientation.

The scattering center will also depend on the type of ranging technique employed by the radar. For example, narrow pulse, leading-edge tracking will yield different apparent ranges for scattering

objects than will peak-signal techniques. However, in our development we do not attempt to explicitly include ranging-technique effects primarily because of the lack of existing data describing US phase-variations as a function of orientation.

We suggest that there are two dominant physical causes (excluding multipath effects) of variations in the US phase for small changes in aspect angle. First, we expect the most significant phase varia-tions to be caused by the motion of the surfaces that yield the USs; that is, the relative motion of the geometric center. Second, we expect that US rotation will also introduce phase variations. We expect two types of effects due to US rotation: low frequency and high frequency. The low-frequency effects should result from the objects that generate the US moving closer or farther away from the radar, thus producing a change of phase (due to earlier or later pulse arrivals). The high-frequency variations should result for USs which arise from the relative phasing of various objects. As the objects rotate, their relative phasing may change producing glint [Section 8], which is a high-frequency phenomenon [Section 9]. However, we expect this effect to be small because glint is inversely proportional to RCS and the existence of the US implies a large RCS.

We will model the US phase by

$$\phi(\vec{R}, \vec{\theta}, \omega, t) = \left[\frac{2\pi}{\lambda}\right] 2|\vec{R}| + \beta(\vec{\theta}) + \xi(\omega, t) \qquad (3.24)$$

where

$\vec{R}$ is the location of the geometric center relative to the radar,

$\vec{\theta}$ is the orientation of the US relative to the radar,

λ is the radar's wavelength,

$\beta(\cdot)$ represents the low-frequency orientation effects, and

$\xi(\omega, t)$ represents the high-frequency effects.

Because of the causal relationship between US motion and target motion, the $\xi(\omega, t)$ process should be correlated, to some extent, with the target motion. The variance of $\xi(\omega, t)$ most likely will be small relative to 2π, otherwise $\xi(\omega, t)$ could be approximated by a phase process that is uniformly distributed over $(0, 2\pi)$. This would yield a target RCS that is Rayleigh distributed (see Section 7) which is in general not true. This observation is consistent with our comments in the previous paragraph.

Because of the lack of experimental data and the intractibility of US-phase analysis, we will not attempt to model or simulate the $\xi(\omega, t)$ process by other than uniformly distributed, uncorrelated processes. The interval over which the processes are defined are specified, in a simulation input, as a percentage of the radar wavelength. Simulation results have indicated that if the random phase varia-tions on a pulse-by-pulse basis exceed about 5% of the radar wavelength, then they become a signifi-cant cause of variations in the scattered field, which intuition suggests should not happen.

Finally, we expect that for small changes in aspect angle, scattered-field variations are due pri-marily to phase variations rather than amplitude variations.

4. MODEL OF THE RECEIVED SIGNAL

Although a radar measures the EM field at its antenna aperture, evaluation of a radar's perfor-mance can be made knowing only a few projections of that field. The most useful projections are

20

received power (RCS) and the azimuth and elevation error signals (glint). The validity of any model of the scattered field that is to have practical applications must be measured relative to such projections. In this chapter we formulate the received signal resulting from scattering by an N-source target that is modeled by unit-scatterers. We develop representations for the received field and the associated azimuth and elevation error signals. The received field representation is used in later chapters.

4.1 Scattered Field

Because we are modeling the target as a finite number of USs, the received electric field at the radar is the linear superposition of the fields from each US. We are interested in representing only the pulse-to-pulse variations in the received signal, not intrapulse properties, so we assume that the received pulses are ideal in the sense that they are completely defined by an amplitude, phase, and pulse-width. Further, we assume that the target extent is small relative to the radar-to-target range and that the radar pulse width is large relative to target extent. This allows the assumption that the return pulses are time coincident. This time-coincident assumption would not be acceptable if we were analyzing range tracking errors or the structure of the received pulse's leading or trailing edge.

Assuming uniform target-illumination (due to large radar-to-target range) and identical transmitter and receiver polarizations, the received field at the radar due to scattering by a point-source target is usually represented by an equation of the form

$$E(\vec{R}_i, \vec{\theta}_i, t) = F^2(\vec{R}_i)\, g(\vec{R}_i)\, a_i(\vec{\theta}_i)\, e^{j\psi_i(\vec{R}_i,\vec{\theta}_i)}\, e^{j\omega t} \tag{4.1}$$

where

ω is the radar frequency,

$\vec{R}_i$ defines the location of the scatterer relative to the radar,

$\vec{\theta}_i$ defines the orientation of the scatterer relative to the radar,

$g(\cdot)$ describes the antenna and propagation effects on the signal,

$F(\cdot)$ describes the effects of multipath,

a_i is the amplitude of the scattered field, and

$\psi_i(\cdot, \cdot)$ is the phase angle of the scattered field.

Three transmit path effects are accounted for here: phases due to radar-to-scatterer path lengths, attenuation due to path losses, and variations in the illuminating signal due to multipath. The phases are accounted for in $\psi_i(\cdot, \cdot)$ and the loss effects in $g(\cdot)$. The multipath effects are discussed in detail in Sec. 4.4, so for the remainder of this section we assume that $F^2(\cdot) = 1$ (i.e., no multipath effects).

Summing the individual fields from an N-source target, the received field becomes

$$E(t) = \sum_{i=1}^{N} g(\vec{R}_i)\, a_i(\vec{\theta}_i)\, e^{j\psi_i(\vec{R}_i,\vec{\theta}_i)}\, e^{j\omega t}. \tag{4.2}$$

The assumption of long range implies that

$$g(\vec{R}_i) \approx g(\vec{R}_j), \quad \text{for all } i, j \tag{4.3}$$

21

so that we can approximate $E(t)$ by

$$E(t) = g(\vec{R})e^{j\omega t} \sum_{i=1}^{N} a_i(\vec{\theta}_i)e^{j\psi_i(\vec{R}_i,\vec{\theta}_i)} \qquad (4.4)$$

where $\vec{R}$ locates a fixed point on the target; for example, the target's center-of-gravity. Assuming that the N sources of the target are USs, we see from Eq. (3.11) that

$$E(t) = g(\vec{R})e^{j\omega t}\,\Gamma(\hat{p}_T,\hat{p}_R) = g(\vec{R})e^{j\omega t}\hat{p}_T^T\left[\sum_{i=1}^{N} X_i(\vec{R}_i,\vec{\theta}_i)\right]\hat{p}_R \qquad (4.5)$$

where $\hat{p}_T$ and $\hat{p}_R$ define the polarization that is implicit in Eq. (4.1). If we make the usual assumption that $\hat{p}_R = \hat{p}_R = (1, 0)^T$, then Eq. (4.5) becomes

$$E(t) = g(\vec{R})e^{j\omega t} \sum_{i=1}^{N} A_{11_i}(\vec{\theta}_i)e^{j\phi_{11_i}(\vec{R}_i,\vec{\theta}_i)}. \qquad (4.6)$$

We next discuss the effect of the radar system on the scattered field.

4.2 Radar System Model

Although our primary concern is target-scattering modeling and not radar-system modeling, practical validation of any scattering model will of necessity involve actual target measurements made by specific radars. Further, we are concerned with scattering models from the point of view of analyzing the effects of target scattering on tracking radars rather than that of predicting scattered electric fields. Therefore for completeness, we include a representation of tracking radars that can be used with the US-model formulation.

We view tracking radars as being composed of three basic functional units: a "front-end," error detectors, and feedback loops. Figure 4.1 is a block diagram of a generic amplitude-comparison, monopulse radar with each functional unit indicated. Such a radar is commonly used as a tracking radar at microwave frequencies. Because this type of radar is widely used in practice, we limit our model of radars to this type. This limitation does not significantly restrict the results to be obtained because the primary influence on tracking performance is the fluctuation of the field scattered from the target. Further, phase-comparison monopulse has been shown to be functionally equivalent to amplitude-comparison monopulse [71], and other forms of tracking radars (e.g., sequential lobing, conical scan, etc.) differ primarily in the form of the front-end transformation and error detector implementations. In any event, the US concept is independent of specific radar implementations.

4.2.1 Front-End

We first consider the effects of the radar front-end: the components that transform the input EM field (at the antenna's aperture) to a complex signal at some intermediate frequency (IF). This IF signal is then processed to obtain tracking information. Our approach is to model the components that convert the input field to an IF signal as a simple, memoryless transformation, which we represent by

$$V(t) = H[E(t)] \qquad (4.7)$$

where $V(t)$ is a voltage. In general, the front-end transformation, $H(\cdot)$, is very difficult to specify precisely because it includes the effects of the antenna, waveguide, hybrids, mixers, and IF amplifiers. Clearly, $H(\cdot)$ depends strongly on the specific radar implementation, particularly the antenna used. For the applications of interest here (where target-radar motion is causing the major fluctuations in the received signal), these devices can be accurately characterized by simple models: hybrids with input signals A and B as producing outputs A+B and/or A-B, mixers as transforming signals with spectra $S(\omega)$ ($\omega > 0$) to signals with spectra $S(\omega - \omega_m)$ ($\omega - \omega_m > 0$) where ω_m is the mixer frequency, and IF amplifiers as constant gain (or logarithmic) devices with feedback gain control. An overall power

Fig. 4.1 — A two-coordinate (azimuth and elevation), amplitude-comparison,
monopulse tracking radar (adapted from Ref. 68)

loss, due mainly to the hybrids, and an overall phase shift, due mainly to physical lengths and the mixers, complete the description of the guided signals. The video signal is produced by detectors (amplitude, phase, or sum-and-difference [71]) that transform the guided fields to voltages. The most complex aspect of $H(\cdot)$ is the transformation of an EM field across the antenna aperture to an EM field within an associated waveguide. This transformation is typically represented by the antenna amplitude-gain pattern (to be referred to as the antenna pattern).

Since we assume that the scatterers are point-source radiators which are at long range, it will be sufficient (as has been the case in many other studies; for example, see Refs. 72 and 73) to model the front-end as the antenna pattern coupled with a complex gain factor and a frequency shift. Specifically, if the antenna amplitude-gain (complex in general) is given by $G(\beta_a, \beta_e)$ where β_a and β_e represent azimuth and elevation angles relative to the radar boresight, then for a point-source target whose angular coordinates relative to the radar boresight are given by (β_a, β_e), we model the front-end transformation as

$$V(t) = H[E(t)] = KG(\beta_a, \beta_e)E_0(\beta_a, \beta_e, t) \qquad (4.8)$$

where K is complex and represents the nonantenna front-end gains and phase shift, and $E_0(\beta_a, \beta_e, t)$ is the value of the scattered electric field at the aperture location defined by β_a and β_e. The carrier frequency of $V(t)$ is the frequency of $E_0(\beta_a, \beta_e, t)$ lowered by the mixer frequency.

Because we are assuming tracking, we are only interested in antenna characteristics near boresight, say ± 3 dB about the main beam maximum. Therefore it may be useful to assume an ideal approximation for the antenna pattern that has a simple analytical form yet accurately represents typical antenna amplitude-gain characteristics in this restricted region:

$$G(\theta, \psi) = G_0 - k(\theta - \theta_0)^2 - k(\psi - \psi_0)^2 \qquad (4.9)$$

where θ_0 and ψ_0 define the pattern maximum relative to a given radar axis (say, boresight) and G_0 and k are constants. However, we note that the long range assumption will often allow the antenna pattern to be modeled as a constant gain because of the resulting negligible separations of the unit-scatterers.

4.2.2 Error Detectors

The error detectors transform guided EM waves to video signals useful for determining antenna pointing (angle) errors. Rhodes [71] has shown that in monopulse radars there are only three distinct kinds of angle detection: amplitude, phase, and sum-and-difference. Because any monopulse error law can be described as a function of the difference-to-sum ratio (Δ/Σ) [74], we model the detectors as producing sum and difference signals which yield as output Δ/Σ. Assuming instantaneous automatic gain control (IAGC), the outputs of the phase-sensitive detectors of Fig. 4.1 are the real part of Δ/Σ due to the sum signal being fed back to the various IF amplifiers [71].

4.2.3 Feedback

There are two feedback loops of interest: IF amplifier feedback and antenna servomechanism (servo) feedback. The amplifier feedback is simply a feedback of the sum signal to control the IF amplifier gains.

Angle error signals that are output from the detectors are used to control the pointing direction of the antenna. This is done by feedback of these signals to servos that control the position of the antenna. Type II servos are usually employed for this purpose [68]. We note that the long range assumption (implying small angular separations of the scatterers) will often allow the effects of the servos to be ignored.

4.3 Received Signals

We now describe the received signal in terms of the scattered field. First we define, in earth- or radar-coordinates, the radar boresight direction $\vec{\beta}_{BS} = (\beta_a, \beta_e)$, and the radar-to-$i$th scatterer sight line,

$\vec{\beta}_i = (\beta_{a_i}, \beta_{e_i})$. The antenna gain associated with the ith scatterer is then given by $G(\vec{\beta}_i - \vec{\beta}_{BS})$ where

$$G(\vec{\beta}_i - \vec{\beta}_{BS}) = G(\beta_{a_i} - \beta_a, \beta_{e_i} - \beta_e). \tag{4.10}$$

With this definition each IF signal has the form (from Eqs. (4.8) and (4.5))

$$V(t) = g(\vec{R})e^{j(\omega - \omega_m)t} \sum_{i=1}^{N} KG(\vec{\beta}_i - \vec{\beta}_{BS})\hat{p}_T^T X_i(\vec{R}_i, \vec{\theta}_i)\hat{p}_R. \tag{4.11}$$

More specifically, there are three signals of interest: one sum and two difference signals. Each signal has an associated sum and difference pattern ($G_\Sigma(\vec{\beta})$, $G_{\Delta_a}(\vec{\beta})$, and $G_{\Delta_e}(\vec{\beta})$) and complex, front-end gains (K_Σ, K_{Δ_a}, and K_{Δ_e}). Suppressing the first two terms of Eq. (4.11), the sum, azimuth-difference, and elevation-difference signals become

$$V_\Sigma(t) = K_\Sigma \sum_{i=1}^{N} G_\Sigma(\vec{\beta}_i - \vec{\beta}_{BS})\hat{p}_T^T X_i(\vec{R}_i, \vec{\theta}_i)\hat{p}_R, \tag{4.12a}$$

$$V_{\Delta a}(t) = K_{\Delta a} \sum_{i=1}^{N} G_{\Delta a}(\vec{\beta}_i - \vec{\beta}_{BS})\hat{p}_T^T X_i(\vec{R}_i, \vec{\theta}_i)\hat{p}_R, \text{ and} \tag{4.12b}$$

$$V_{\Delta e}(t) = K_{\Delta e} \sum_{i=1}^{N} G_{\Delta e}(\vec{\beta}_i - \vec{\beta}_{BS})\hat{p}_T^T X_i(\vec{R}_i, \vec{\theta}_i)\hat{p}_R. \tag{4.12c}$$

The three antenna patterns are derived from Eq. (4.9) where we have assumed that each of the four radiators that comprise the antenna have identical patterns and that each is offset relative to the radar boresight. The sum pattern is represented by

$$G_\Sigma(\vec{\beta}_i) = G_\Sigma(\beta_{a_i}, \beta_{e_i}) = \sum_{j=1}^{4} G(\beta_{a_i} - \beta_{a_j}, \beta_{e_i} - \beta_{e_j}) = \sum_{j=1}^{4} G(\vec{\beta}_i - \vec{\beta}_j) \qquad (4.13a)$$

where $\vec{\beta}_j = (\beta_{a_j}, \beta_{e_j})$ represents the associated radiator's offset relative to the radar boresight. The difference patterns are represented by

$$G_{\Delta a}(\vec{\beta}_i) = G(\vec{\beta} - \vec{\beta}_1) + G(\vec{\beta} - \vec{\beta}_3) - G(\vec{\beta} - \vec{\beta}_2) - G(\vec{\beta} - \vec{\beta}_4) \qquad (4.13b)$$

and

$$G_{\Delta e}(\vec{\beta}_i) = G(\vec{\beta} - \vec{\beta}_1) + G(\vec{\beta} - \vec{\beta}_2) - G(\vec{\beta} - \vec{\beta}_3) - G(\vec{\beta} - \vec{\beta}_4). \qquad (4.13c)$$

Equation (4.11) is our fundamental representation of the monopulse-radar received-signal due to N point-sources. Representations of this for radar-system have been used for analyses by others; the most common use assumes a mix of independent processes and deterministic functions for one or several of the target parameters (e.g., Refs. 11, 19, 20, 23, 24, 25, 75, and 76).

4.4 Sea-Surface Multipath Effects

If the target is a surface ship, then for small and moderate radar-to-ship grazing angles, sea-surface multipath affects the received signals. These multipath effects alter both the signal illuminating the ship and the scattered field.

As discussed in the introduction, the effects of multipath on the received power of a signal transmitted by a point source is well understood, but an apparent-point-source representation of the scattered field has only been determined for the specular component. However, because the diffuse scattering arises from scattering over a large area, there are at least several scatterers comprising the ship at any aspect, and because we are interested in only a representation of "average" seas (determined only by a sea-state parameter), we will model the diffuse vector's location point as the associated target's image-point. Although we will develop glint equations using this model, clearly it is not restrictive and the method applies for other diffuse models as well.

To be consistent with the multipath models employed, we assume that the radar's antenna has a beamwidth wide enough to fully illuminate the first several Fresnel zones about the specular point (defined in Fig. 4.2). We note that this assumption will hold even for relatively narrow beams if the radar-to-target range is large. Because of our assumption of low grazing angles and the reasons stated above, we also ignore time delays associated with the multipath signals, noting that when analyzing range-tracking errors such delays should be accounted for.
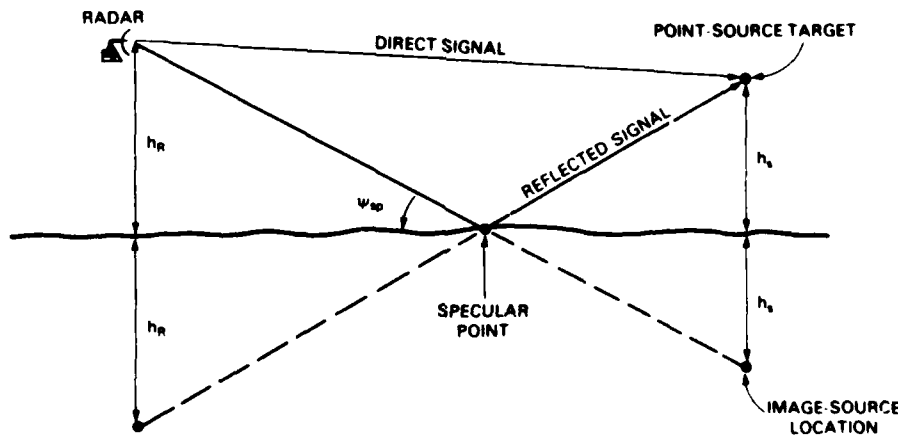

Fig. 4.2 — Multipath geometry

scatterer has the form $E = FE_0$ where E is the direct field (no multipath). Then if we view the scatterer as transmitting the signal FE_0, then the signal received at the radar will be F^2E_0. From the point of view of the radar, the received signal appears to have a direct component $D = FE_0$ and a reflected component $R = (\rho_C + \rho_I)FE_0$. Therefore we separate the two-way multipath coefficient F^2 for the ith US into direct and reflected coefficients:

$$E_i = F_i^2 E_0 = (1 + \rho_{C_i} + \rho_{I_i})F_i E_0$$

$$= F_i E_0 + (F_i - 1)F_i E_0 = D_i + R_i. \tag{4.18}$$

Finally, we need the direction of propagation for D_i and R_i.

If in a given coordinate system $\vec{R}_i$ locates the ith scatterer and $\vec{R}_R$ locates the receiver, then the direction of propagation for the ith direct signal is given by

$$\vec{R}_{D_i} = \vec{R}_R - \vec{R}_i. \tag{4.19}$$

In Earth-axis, cartesian coordinates,

$$\vec{R}_{D_i} = (R_{x_R} - R_{x_i}, R_{y_R} - R_{y_i}, h_R - h_i) \tag{4.20}$$

where h_R and h_i are the heights of the radar and the ith source above Earth. Therefore the direction of propagation for the direct and reflected field components are

$$\hat{r}_{D_i} = \frac{\vec{R}_{D_i}}{|\vec{R}_{D_i}|} \tag{4.21a}$$

and

$$\hat{r}_{R_i} = \frac{\vec{R}_{R_i}}{|\vec{R}_{R_i}|} \tag{4.21b}$$

where

$$\vec{R}_{R_i} \triangleq (R_{x_R} - R_{x_i}, R_{y_R} - R_{y_i}, h_R + h_i). \tag{4.22}$$

With the separation of Eqs. (4.18) and (4.21), we see that by viewing the reflected fields as an additional set of N scatterers, Eq. (4.11) becomes

$$V(t) = g(\vec{R})e^{j(\omega - \omega_m)t}K \sum_{i=1}^{N} \{G(\vec{\beta}_i - \vec{\beta}_{BS})F_i + G(\vec{\beta}_{i+N} - \vec{\beta}_{BS})F_i(F_i - 1)\}\hat{p}_T^T X_i \hat{p}_R^T. \tag{4.23}$$

Though we use this point-source model to account for the effects of multipath, USs result from surfaces that are distributed in space. When there is no multipath we can represent the scattered field from a US by

$$\vec{E}^s \approx \frac{jke^{jkR}}{2\pi R} \int_{S'} \frac{E_0}{\eta} [\hat{n} \times (\hat{r} \times \hat{e})] \times \hat{r}e^{-2jk\hat{r} \cdot \vec{r}'}dS'. \tag{3.16}$$

Using the point-source multipath model to represent the incident field, we represent the scattered field in the presence of multipath by

$$\vec{E}^s_{mp} \approx \frac{jke^{jkR}}{2\pi R} \int_{S'} \frac{E_0 F^2(\vec{r}\,')}{\eta} [\hat{n} \times (\hat{r} \times \hat{e})] \times \hat{r}e^{-2jk\hat{r} \cdot \vec{r}'}dS' \tag{4.24}$$

where $F(\vec{r}')$ represents the complex multipath factor at the point $\vec{r}'$. If over S',

$$F(\vec{r}') = F_0,\tag{4.25}$$

then we have the point-source representation described above:

$$\vec{E}^s_{mp} = F_0^2 \vec{E}^s.\tag{4.26}$$

Although data collected by NRL and analyzed by the author indicate that $F(\vec{r}')$ can often be approximated by an azimuth-independent process over relatively large variations in azimuth, other data have shown [77] that $F(\vec{r}')$ rapidly decorrelates in elevation. Therefore for most USs, representing $\vec{E}^s_{mp}$ by Eq. (4.26), with $F_0 = F(\vec{r}_i')$ where $\vec{r}_i'$ is the ith US location, will not be valid. The difficulty raised here is, to our knowledge, an open question: can the target effects and the multipath effects be represented in Eq. (4.24) in a way that yields an equivalent-point-source model for the scattering?

As stated above, the point-source multipath model is valid when the transmitting and receiving amplitude patterns (gain pattern for an antenna) are not narrow. This constraint will likely hold for the sphere type and corner-reflector type of US amplitude functions. For the highly specular flat-plate type a modification to the multipath effects may be required analogous to the antenna gain-pattern correction suggested in Ref. 49. Such a modification was not made in the simulation.

Because multipath is but one parameter (though an important one) affecting the ship scattering and because the point-source model presented here is the only validated stochastic model of over-water multipath that we are aware of, we have used it in our simulation studies. In Section 9 we discuss results obtained using this modeling approach in the simulation.

5. UNIT-SCATTERER-MOTION MODELS

In this section we develop equations of motion for an arbitrary US location because this motion determines the amplitude and phase variations in the received field. Our purpose is not ship-motion modeling per se but US-motion modeling for use in analyzing and simulating scattered fields. However, for completeness we investigate two basic approaches to ship-motion modeling. In Sec. 5.2 we formulate a motion model that assumes knowledge of the sea forces that cause ship motion. Then in Sec. 5.3, we discuss a frequency-response model that has been quite useful in ship-motion modeling given knowledge of the sea spectrum. The DTNSRDC has used the model to generate libraries of center-of-gravity-motion (cg-motion) spectra for various ships (e.g., Refs. 78 and 79). In later chapters we begin our analyses and simulations by assuming knowledge of these cg-motion spectra. Because these motions are zero-mean Gaussian, the associated spectra are all that is required to completely specify them as stochastic processes.

Our reliance on the DTNSRDC spectra is not without its costs. Because of a strong desire to develop models that are intuitively appealing and easy to work with (assuming a minimal background in mathematics), the sea-surface model that has been developed by the oceanographic community is in a form that is nonstandard relative to the system-theoretic formulation. The differences are slight but confusing and can lead to errors if not correctly accounted for: the spectrum is defined for positive frequencies only and so that the integral of the spectrum is the energy in the sea surface (at a point on the surface). To minimize the confusion that would result when the tabulated spectra are used in a simulation, we have chosen to follow the nonstandard, oceanographic spectrum-formulation. This allows us to directly use the tabulated (nonstandard) spectra.

5.1 Approaches to Linearization

We use linear equations because they are widely used in the study of both ship and aircraft motion and are easy to work with. We are interested primarily in small deviations in the target's

motion from a nominal trajectory, and also in target motion modeling only over relatively short periods of time (usually on the order of seconds to no more than several minutes). There are two basic approaches used in developing linear equations of ship motion. The first approach is to transform Newton's six nonlinear force and moment equations from the target's cg axis-system to an axis system that is determined by target symmetry. The equations are then linearized in the symmetry axis-system. We call this the transform-first approach. The second approach is to assume linear, second-order differential equations in the cg axis-system to describe the six forces and moments. The various coefficients are then estimated via calculations or measurements. We call this the linearize-first approach. The choice of approach usually depends on the ease of obtaining values for the equation coefficients and the feasibility of measuring the modeled forces and moments for the target of interest.

The transform-first approach to linearization is strongly dependent on target structure, especially symmetry. Using this approach, various sets of linear equations have been developed for ships and aircraft. The form of these equation sets varies depending on intended applications.

The linearize-first approach begins with a set of linear, second-order differential equations for the ship's cg-motion. Therefore assuming rigid body motion, the equations of motion for an individual US have the same form regardless of target structure. We will use the linearize-first approach in developing ship motion models that are useful in ship scattering studies.

5.2 Motion Equations Given the Driving Forces and Moments

We begin by deriving a set of motion equations for an arbitrary US location by assuming knowledge of linearized equations of motion for the target's cg and the driving forces and moments. We also assume that the target undergoes only rigid-body motion and that the six motions of the target are uncoupled (i.e., $u = \dot{x}, v = \dot{y}, \ldots, r = \dot{\psi}$).

5.2.1 Definition of the Axis Systems

We use two axis-systems in describing US motion: an Earth-axis system and a target-body axis system. Each system is right handed with z-axes that are positive upward (relative to Earth).

The Earth-axis system is fixed relative to Earth's surface (assumed to be flat) with its origin located at some fixed but arbitrary point relative to Earth's surface. The x-y axes-plane is located parallel to the plane of Earth's surface and the z-axis is oriented positive upward. Vectors represented in Earth coordinates have no superscript.

The target-body axis-system is fixed relative to the target with its origin at the target's cg. The x-axis is parallel to a longitudinal line-of-symmetry for the target, positive forward. The y-axis is parallel to a transverse line-of-symmetry for the target. The z-axis is positive upward. Vectors represented in target-body coordinates are superscripted with B.

Figure 5.1 illustrates these axis systems.

5.2.2 Motion Equations for the Target's Center of Gravity

Following the notation in Ref. 80, the six equations of cg motion have the form

$$M_i \frac{d^2 x_i}{dt^2} + N_i \frac{dx_i}{dt} + R_i x_i = F_i(\omega, t), \quad i = 1, \ldots, 6. \tag{5.1}$$
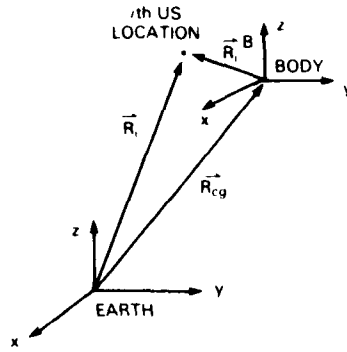
Fig. 5.1 — The fundamental axis systems and position vectors

In Eq. (5.1) we use the notation $F_i(\omega, t)$ to describe each input force and moment. We assume that the $F_i(\omega, t)$ are stochastic processes. For convenience we rewrite Eq. (5.1) as

$$\frac{d^2 x_i}{dt^2} + 2h_i \frac{dx_i}{dt} + \nu_i x_i = f_i(\omega, t), \quad i = 1, \ldots, 6 \tag{5.2}$$

where $2h_i$ represents a damping factor and ν_i represents a natural undamped frequency of oscillation of the target. Writing Eq. (5.2) in state-variable format we have

$$\dot{\vec{x}}_i = A_i \vec{x}_i + B_i \vec{f}_i \tag{5.3a}$$

where

$$A_i = \begin{bmatrix} 0 & 1 \\ -\nu_i & -2h_i \end{bmatrix} \tag{5.3b}$$

and

$$B_i = \begin{bmatrix} 0 \\ 1 \end{bmatrix} \tag{5.3c}$$

$$\vec{x}_i = (x_i, \dot{x}_i)^T \tag{5.3d}$$

$$\vec{f}_i = (0, f_i)^T.$$

We define the state of the target-motion system as the vector of position and velocity variables of the six motion equations:

$$\vec{x} = (x, \dot{x}, y, \dot{y}, z, \dot{z}, \phi, \dot{\phi}, \theta, \dot{\theta}, \psi, \dot{\psi})^T \tag{5.4}$$

where x, y, and z are the linear coordinates, and ϕ, θ, and ψ are the angular coordinates of the target's cg. Because the motions are assumed to be uncoupled, the state vector becomes

$$\vec{x} = (x, u, y, \nu, z, w, \phi, p, \theta, q, \psi, r)^T \tag{5.5}$$

where u, ν, w, p, q, and r are the usual variables of a six degrees-of-freedom model; that is, u, ν, and w are the linear rates of change and p, q, and r are the angular rates of change. The system differential equations can now be written in the form

$$\dot{\vec{x}} = \overline{A}\vec{x} + \overline{B}f \tag{5.6}$$

where $\bar{A}$ is a 12 × 12 matrix with the form

$$\bar{A} = \begin{bmatrix} A_x & & & & & 0 \\ & A_y & & & & \\ & & A_z & & & \\ & & & A_\phi & & \\ & & & & A_\theta & \\ 0 & & & & & A_\psi \end{bmatrix} \tag{5.7}$$

with the A_i defined by Eq. (5.3b). The $\bar{B}$ matrix is the 12 × 6 matrix (from Eq. (5.3c))

$$\bar{B} = \begin{bmatrix} 0 & 0 & 0 & 0 & 0 & 0 \\ 1 & 0 & 0 & 0 & 0 & 0 \\ 0 & 0 & 0 & 0 & 0 & 0 \\ 0 & 1 & 0 & 0 & 0 & 0 \\ 0 & 0 & 0 & 0 & 0 & 0 \\ 0 & 0 & 1 & 0 & 0 & 0 \\ 0 & 0 & 0 & 0 & 0 & 0 \\ 0 & 0 & 0 & 1 & 0 & 0 \\ 0 & 0 & 0 & 0 & 0 & 0 \\ 0 & 0 & 0 & 0 & 1 & 0 \\ 0 & 0 & 0 & 0 & 0 & 0 \\ 0 & 0 & 0 & 0 & 0 & 1 \end{bmatrix}. \tag{5.8}$$

The input vector is

$$\vec{f} = (f_x, f_y, f_z, f_\phi, f_\theta, f_\psi)^T. \tag{5.9}$$

For given h_i and ν_i coefficients Eq. (5.6) can now be solved. The solution is

$$\vec{x}(t) = \Phi(t)\vec{x}(0) + \int_0^t \Phi(t - \tau)\bar{B}\vec{f}(\tau)d\tau \tag{5.10}$$

where $\Phi(t)$ is the 12x12 block diagonal matrix

$$\Phi(t) = \begin{bmatrix} \Phi_x(t) & & & & & \\ & \Phi_y(t) & & & & 0 \\ & & \Phi_z(t) & & & \\ & & & \Phi_\phi(t) & & \\ & 0 & & & \Phi_\theta(t) & \\ & & & & & \Phi_\psi(t) \end{bmatrix}. \tag{5.11}$$

Each $\Phi_i(t)$ in Eq. (5.11) is the 2 × 2 transition matrix associated with the appropriate A_i from Eq. (5.3a).

5.2.3 Motion Equations for the Unit-Scatterer Locations

The location of the ith US (ith point) on the target (in Earth coordinates) is given by

$$\vec{R}_i(t) = \vec{R}_i(0) + \int_0^t \vec{V}_i(\tau)d\tau$$
$$= (R_{x_i}, R_{y_i}, R_{z_i})^T \tag{5.12}$$

where $\vec{V}_i(t)$ is the velocity of the ith point, and $\vec{R}_i(0)$ is the initial location of the ith point. Now

$$\vec{V}_i(t) = \vec{V}_{cg}(t) + \vec{\omega}(t) \times \vec{R}_i^B \tag{5.13}$$

where $\vec{V}_{cg}(t)$ is the linear velocity of the target's cg ($\vec{V}_{cg}(t) = (u, \nu, w)^T$), $\vec{\omega}(t)$ is the angular velocity of the target ($\vec{\omega}(t) = (p, q, r)^T$), and $\vec{R}_i^B = (x_i, y_i, z_i)^T$ is the location of the ith point relative to the target cg in target-body coordinates (which, for rigid bodies, is constant) so that

$$\vec{R}_i(t) = \vec{R}_i(0) + \int_0^t [\vec{V}_s(\tau) + \vec{\omega}(\tau) \times \vec{R}_i^B(\tau)]d\tau. \tag{5.14}$$

Expanding the cross-product term we have

$$\vec{\omega} \times \vec{R}_i^B = (z_i q - y_i r)\hat{i} + (x_i r - z_i p)\hat{j} + (y_i p - x_i q)\hat{k}. \tag{5.15}$$

Equation (5.14) can now be written in the form

$$
\begin{bmatrix} R_{x_i}(t) \\ R_{y_i}(t) \\ R_{z_i}(t) \end{bmatrix} = \begin{bmatrix} R_{x_i}(0) \\ R_{y_i}(0) \\ R_{z_i}(0) \end{bmatrix} + \int_0^t \begin{bmatrix} u + (z_i q - y_i r) \\ \nu + (x_i r - z_i p) \\ w + (y_i p - x_i q) \end{bmatrix} d\tau
$$

$$
= \begin{bmatrix} R_{x_i}(0) \\ R_{y_i}(0) \\ R_{z_i}(0) \end{bmatrix} + \int_0^t \begin{bmatrix} 1 & 0 & 0 & 0 & z_i & -y_i \\ 0 & 1 & 0 & -z_i & 0 & x_i \\ 0 & 0 & 1 & y_i & -x_i & 0 \end{bmatrix} \begin{bmatrix} u \\ \nu \\ w \\ p \\ q \\ r \end{bmatrix} d\tau. \tag{5.16}
$$

By the decoupling assumption (Eqs. (5.4) and (5.5)), Eq. (5.16) becomes

$$
\vec{R}_i(t) = \vec{R}_i(0) + \int_0^t \begin{bmatrix} 1 & 0 & 0 & 0 & z_i & -y_i \\ 0 & 1 & 0 & -z_i & 0 & x_i \\ 0 & 0 & 1 & y_i & -x_i & 0 \end{bmatrix} \begin{bmatrix} \dot{x} \\ \dot{y} \\ \dot{z} \\ \dot{\phi} \\ \dot{\theta} \\ \dot{\psi} \end{bmatrix} d\tau \tag{5.17a}
$$

$$= \vec{R}_i(0) + \int_0^t T_i \dot{\vec{x}} d\tau \tag{5.17b}$$

$$= \vec{R}_i(0) + T_i[\vec{x}(t) - \vec{x}(0)] \tag{5.17c}$$

where $\vec{x}$ is defined by Eq. (5.4) and

$$
T_i = \begin{bmatrix} 1 & 0 & 0 & 0 & 0 & 0 & 0 & 0 & z_i & 0 & -y_i & 0 \\ 0 & 0 & 1 & 0 & 0 & 0 & -z_i & 0 & 0 & 0 & x_i & 0 \\ 0 & 0 & 0 & 0 & 1 & 0 & y_i & 0 & -x_i & 0 & 0 & 0 \end{bmatrix}. \tag{5.18}
$$

Substituting Eq. (5.10) into Eq. (5.17c) we have the position of the ith US as

$$\vec{R}_i(t) = \vec{R}_i(0) + T_i \left[\Phi(t)\vec{x}(0) + \int_0^t \Phi(t-\tau)\bar{B}\vec{f}(\tau)d\tau \right] - T_i\vec{x}(0)$$

$$= \vec{R}_i(0) + T_i \left[(\Phi(t) - \Phi(0)) + \int_0^t \Phi(t-\tau)\bar{B}\vec{f}(\tau)d\tau \right]. \tag{5.19}$$

Next we wish to obtain the components of the impulse response matrix for the motion of the ith scatterer (in Earth coordinates). Relabeling (see Eq. (5.11)) the transition matrix as

$$\Phi(t) = \begin{bmatrix} \Phi_1 & & & & & \\ & \Phi_2 & & & 0 & \\ & & \Phi_3 & & & \\ & & & \Phi_4 & & \\ & 0 & & & \Phi_5 & \\ & & & & & \Phi_6 \end{bmatrix} \tag{5.20}$$

where

$$\Phi_i = \begin{bmatrix} \Phi_{i,11} & \Phi_{i,12} \\ \Phi_{i,21} & \Phi_{i,22} \end{bmatrix}, \tag{5.21}$$

we have

$$T_i\Phi(t) = \begin{vmatrix} \phi_{1,11} & 0 & 0 \\ \phi_{1,12} & 0 & 0 \\ 0 & \phi_{2,11} & 0 \\ 0 & \phi_{2,12} & 0 \\ 0 & 0 & \phi_{3,11} \\ 0 & 0 & \phi_{3,12} \\ 0 & -z_i\phi_{4,11} & y_i\phi_{4,11} \\ 0 & -z_i\phi_{4,12} & y_i\phi_{4,12} \\ z_i\phi_{5,11} & 0 & -x_i\phi_{5,11} \\ z_i\phi_{5,12} & 0 & -x_i\phi_{5,12} \\ -y_i\phi_{6,11} & x_i\phi_{6,11} & 0 \\ -y_i\phi_{6,12} & x_i\phi_{6,12} & 0 \end{vmatrix} \tag{5.22}$$

so that the impulse response matrix becomes

$$T_i\Phi\bar{B} = \begin{bmatrix} \phi_{1,12} & 0 & 0 & 0 & z_i\phi_{5,12} & -y_i\phi_{6,12} \\ 0 & \phi_{2,12} & 0 & -z_i\phi_{4,12} & 0 & x_i\phi_{6,12} \\ 0 & 0 & \phi_{3,12} & y_i\phi_{4,12} & -x_i\phi_{5,12} & 0 \end{bmatrix}. \tag{5.23}$$

Finally we note that

$$T_i[\Phi(t) - \Phi(0)]\bar{x}(0) = \begin{vmatrix} (\phi_{1,11} - 1) & 0 & 0 \\ \phi_{1,12} & 0 & 0 \\ 0 & (\phi_{2,11} - 1) & 0 \\ 0 & \phi_{2,12} & 0 \\ 0 & 0 & (\phi_{3,11} - 1) \\ 0 & 0 & \phi_{3,12} \\ 0 & -z_i(\phi_{4,11} - 1) & y_i(\phi_{4,11} - 1) \\ 0 & -z_i\phi_{4,12} & y_i\phi_{4,12} \\ z_i(\phi_{5,11} - 1) & 0 & -z_i(\phi_{5,11} - 1) \\ z_i\phi_{5,12} & 0 & -x_i\phi_{5,12} \\ -y_i(\phi_{6,11} - 1) & x_i(\phi_{6,11} - 1) & 0 \\ -y_i\phi_{6,12} & x_i\phi_{6,12} & 0 \end{vmatrix}^T \begin{bmatrix} x_0 \\ u_0 \\ y_0 \\ v_0 \\ z_0 \\ w_0 \\ \phi_0 \\ p_0 \\ \theta_0 \\ q_0 \\ \psi_0 \\ r_0 \end{bmatrix}$$

$$(\phi_{1,11} - 1)x_0 + \phi_{1,12}u_0 + z_i(\phi_{5,11} - 1)\theta_0 + z_i\phi_{5,12}q_0 - y_i(\phi_{6,11} - 1)\psi_0 - y_i\phi_{6,12}r_0$$
$$(\phi_{2,11} - 1)y_0 + \phi_{2,12}v_0 - z_i(\phi_{4,11} - 1)\theta_0 - z_i\phi_{4,12}q_0 - x_i(\phi_{6,11} - 1)\psi_0 + x_i\phi_{6,12}r_0 \tag{5.24}$$
$$(\phi_{3,11} - 1)z_0 + \phi_{3,12}w_0 + y_i(\phi_{4,11} - 1)\theta_0 + y_i\phi_{4,12}q_0 - x_i(\phi_{5,11} - 1)\psi_0 - x_i\phi_{5,12}r_0.$$

33

5.3 Motion Equations Given the Sea Spectrum

Although ship-motion studies date back to Froude [81] and Krylov [82], it has only been within the last 30 years that ship motions in realistic seas have become predictable with some confidence [83]. The sea surface (waves) causes most of the nonmaneuvering ship motion and the major difficulty in modeling ship motion was the lack of an accurate model of this surface. The early sea-surface models were deterministic and therefore, because of the complexity of the surface, quite limited. In 1952, a stochastic model for the sea surface was introduced by Pierson [84]. Then in 1953, St. Denis and Pierson [80] introduced a ship motion model that coupled the stochastic sea-surface model with linear ship-motion equations to produce a method of describing ship motion that is still used today. The linearize-first model of this section is based on this method.

5.3.1 Assumptions

There are four fundamental assumptions made by St. Denis and Pierson that allow the linearization of the ship motion equations. They are [80]:

(1) The theory is restricted to vessels of the displacement type (e.g., this excludes planing and hydrofoil craft).

(2) The Froude-Krylov hypothesis holds: the waves act on the ship but the ship does not act on the waves.

(3) The theory is restricted to uncoupled motions, and the motions are assumed to be independent (e.g., this restricts the theory to vessels where the water-planes are quasi-symmetric fore and aft).

(4) The motion response is assumed to be a linear function of the exciting, restoring, damping, and inertia forces (e.g., this restricts the theory to vessels that are wall sided).

Given these assumptions, each of the six (decoupled) motions can be described by a linear equation of the form

$$\frac{d^2x}{dt^2} + 2h \frac{dx}{dt} + \nu x = \frac{1}{M} f(t). \tag{5.25}$$

Of the six possible motions (referred to as roll, pitch, yaw, surge, sway, and heave), three are dominant contributors to the ship motion: heave, pitch, and roll. However, for generality we include all six motions in the solutions.

5.3.2 Sea Surface Model

As stated previously, the Pierson sea-surface model is the basis for describing ship motion. This model describes the height of the surface (wave height) relative to its mean-level as a function of position and time. The model is a second-order, Gaussian stochastic process with a spectrum that is directional. The spectrum is the most important parameter of this model, and various models for it have been developed including those by Neumann [85], Bretschneider [86], and Pierson and Moskowitz [87]. In general, experimentally measured wave height spectra have the following major characteristics ($\omega > 0$):

- The spectra are smooth.
- There is a dominant frequency (single mode).
- The spectral shape is "bandpass."
- There is asymmetry to the spectra; there is more energy in the higher frequencies.

Figure 5.2 is an illustration of a spectrum exemplifying these characteristics. Next we present a description of the sea surface using the nonstandard, oceanographic approach.
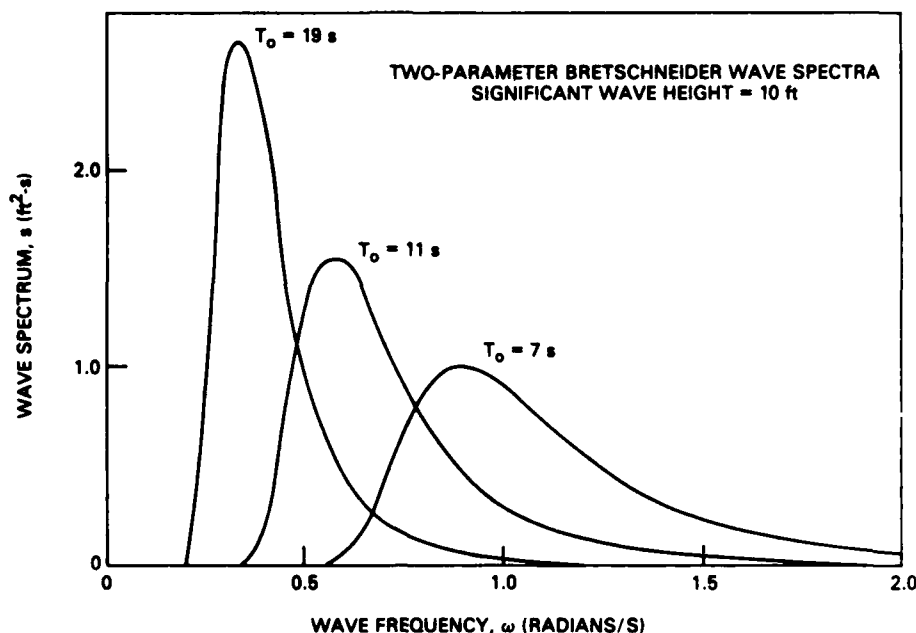

Fig. 5.2 — Sample Bretschneider wave spectrum: T_0 is the modal wave
period (from Ref. 78)

Given a process $\eta(t)$ that is stationary, an autocovariance $R(\tau)$ and a spectrum $F(\omega)$ for the process can be defined by the relations

$$R(\tau) = \int_{-\infty}^{\infty} e^{j\omega\tau} F(\omega) d\omega \qquad (5.26a)$$

and

$$F(\omega) = \frac{1}{2\pi} \int_{-\infty}^{\infty} e^{-j\omega\tau} R(\tau) d\tau. \qquad (5.26b)$$

Note that associating the 2π with the forward transform allows the variance to be defined as simply "the integral of the spectrum." The "spectrum" of the sea surface, $S(\omega)$, is defined for positive frequencies only by

$$S(\omega) = 2F(\omega). \qquad (5.27)$$

Because wave height is a real process, Eqs. (5.26) are usually expressed as the real cosine transforms

$$R(\tau) = \int_{0}^{\infty} \cos \omega\tau \, S(\omega) d\omega \qquad (5.28a)$$

and

$$S(\omega) = \frac{2}{\pi} \int_{0}^{\infty} \cos \omega\tau \, R(\tau) d\tau. \qquad (5.28b)$$

The Gaussian sea-surface is represented by the stochastic integral

$$\eta(t) = \int_{0}^{\infty} \cos(\omega t + \phi(\omega)) \sqrt{2S(\omega) d\omega}. \qquad (5.29a)$$

The integral in Eq. (5.29) is defined as a quadratic-mean limit of a sequence of random partial sums,

$$\eta(t) = \underset{\substack{\omega_{2N} \to \infty \\ \omega_{2N+2} - \omega_{2N} \to 0}}{\text{l.i.m.}} \sum_{i=1}^{N} \cos[\omega_{2i+1} t + \phi(\omega_{2i+1})] \sqrt{S(\omega_{2i+1})(\omega_{2i+2} - \omega_{2i})}, \qquad (5.29b)$$

35

where $\phi(\omega_i)$ is a sequence of independent random variables that are uniformly distributed over $(0, 2\pi)$. This integral was formally introduced by Levy [88] and was used in sea-surface modeling by Pierson [89] (and noise-current modeling by Rice [90]). It allows the intuitive interpretation that $\eta(t)$ is made up of an infinite number of randomly phased sinusoids with amplitudes that are determined by the sea spectrum. Most importantly, Eq. (5.28a) is useful for simulating samples of the process $\eta(t)$ by making the approximation

$$\eta(t) \approx \eta_a(t) = \sum_{i=1}^{N} \cos [\omega_i t + \phi(\omega_i)] \sqrt{2S(\omega_i)\Delta\omega_i}. \tag{5.30}$$

Also, samples of the solution of

$$\frac{d^2x}{dt^2} + 2h \frac{dx}{dt} + \nu x = \eta(t) \tag{5.31}$$

can be simulated by

$$x(t) \approx \sum_{i=1}^{N} x_i(t) \tag{5.32}$$

where $x(t)$ is the solution of Eq. (5.31) for

$$\eta(t) \approx \eta_a(t) = \cos [\omega_i t + \phi(\omega_i)] \sqrt{2S(\omega_i)\Delta\omega_i}. \tag{5.33}$$

This is the equation that we use in Section 6 to simulate the various ship-motion processes.

Although Eq. (5.29a) describes the vertical motion (force magnitude) of the sea at some location on the surface, it contains no information describing the "direction of propagation" (force direction) of the sinusoidal components. Though we do not require a two-dimensional representation in later chapters, for completeness we present a brief description of the one commonly used. This model also follows the nonstandard formulation.

The directional effects are accounted for by a simple heuristic modification of the sea-surface spectrum. (Note that because of the nonstandard formulation, the directional sea-spectrum is not a spectral density in the sense of two-dimensional random fields [91] and that it must also be used with caution.) The directional sea-surface spectrum $S(\omega, \theta)$ where θ represents an angle measured relative to a fixed direction, has been described [92], based on empirical measurements, by

$$S(\omega, \theta) = \begin{cases} c\frac{\pi}{2} \omega^{-6}e^{-2g^2\omega^{-2}u^{-2}} \\ \quad \cdot \frac{1}{\pi} \{1 + (0.50 + 0.82 \, e^{-1/2g^{-4}\omega^4u^4}) \cos 2\theta \\ \quad +(0.32 \, e^{-1/2g^{-4}\omega^4u^4}) \cos 4\theta\}, \quad \begin{cases} \omega_0 \leqslant \omega \leqslant \infty \\ -\frac{\pi}{2} \leqslant \theta \leqslant \frac{\pi}{2} \end{cases} \\ 0 \qquad\qquad\qquad\qquad\qquad\qquad , \text{ otherwise.} \end{cases} \tag{5.34}$$

(The gravitational constant is g, and the mean wind speed is u.) Another model, used by Pierson, Neumann, and James [93], is

$$S(\omega, \theta) = \begin{cases} C\omega^{-6}e^{-2g^2\omega^{-2}u^{-2}\cos^2\theta} \\ 0 \end{cases} , \quad \begin{cases} \omega_0 \leqslant \omega \leqslant \infty \\ -\dfrac{\pi}{2} \leqslant \theta \leqslant \dfrac{\pi}{2} \\ \text{, otherwise} \end{cases} \tag{5.35}$$

where $g = 980$ cm/s^2, and $C \approx 1.53 \times 10^4$ cm^{2}s^{-5}. Not only is Eq. (5.35) simpler than Eq. (5.34), but it has been found to be a very good approximation for actual seas [92,94] where high-frequency components (frequencies greater than about 1 Hz) are not significant. The "spectral representation" of the sea surface at some point (x, y) as a function of $S(\omega, \theta)$ is [89]

$$\eta(x, y, t) = \int_0^\infty \int_{-\pi/2}^{\pi/2} \cos\left[\frac{\omega^2}{g}(x\cos\theta + y\sin\theta) - \omega t + \phi(\omega, \theta)\right]\sqrt{2S(\omega, \theta)d\omega d\theta}. \tag{5.36}$$

The usefulness of Eq. (5.36) is that it represents $\eta(t)$ as a summation of sinusoids of frequency ω and direction θ, traveling in the mean wind-direction ($\theta = 0$), distributed in energy and direction as described by Eq. (5.35). Figure 5.3 is a qualitative illustration of this interpretation.
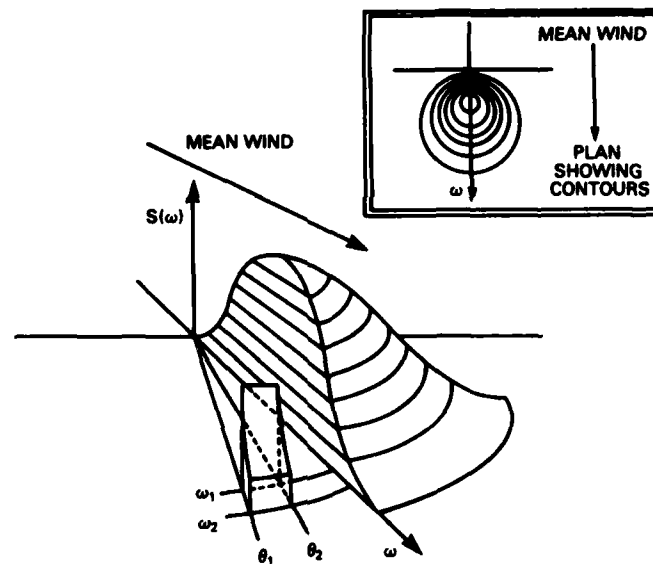
Fig. 5.3 — Qualitative description of the two-dimensional wave spectrum (from Ref. 94)

5.3.3 Response Amplitude Operators

As we saw in the previous subsection, the sea surface can be modeled as a Gaussian process so that different seas are described by specifying their associated "spectra." Building on this fundamental role for the spectrum, St. Denis and Pierson [80] developed a frequency response model of ship motions. The system response functions describing the interactions between the ship and sea are called response amplitude operators (RAOs). The RAOs are the frequency response of the various degrees of freedom of the ship to the wave motion. Given the wave-height directional spectrum, $S(\omega, \theta)$, and the ith degree-of-freedom (dof) RAO, $R_i(\omega, \theta)$, the associated response spectrum is

$$S_i(\omega) = \int_{-\pi/2}^{\pi/2} S_i(\omega, \theta)d\theta = \int_{-\pi/2}^{\pi/2} |R_i(\omega, \theta)|^2 S(\omega, \theta)d\theta, \quad i = 1, \ldots, 6. \tag{5.37}$$

In terms of system theory, one can think of $R_i(\omega, \theta)$ as the frequency response of a system whose input is the stochastic wave motion along direction θ and whose output is the ith dof ship motion. The total motion due to the sea is then computed by incoherent, linear superposition (Eq. (5.37)) of the contributions from each wave direction. Figure 5.4 illustrates this concept assuming a finite number N of wave directions.
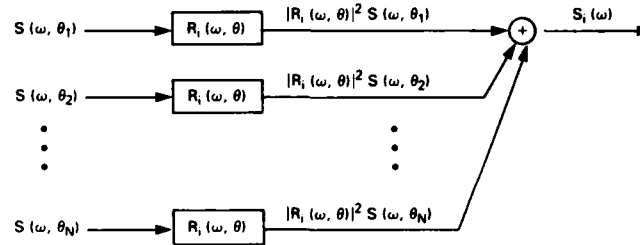

Fig. 5.4 — A linear system interpretation of a ship's response to a directional sea, Eq. (5.38)

When a ship moves in a directional sea, the response of the ship to the sea is a function of both ship speed and heading relative to the sea-wave direction. The RAOs are derived with reference to a system of coordinates fixed in space and oriented so that the x-axis is positive in the direction of the ship's heading. To account for the speed and direction effects, a transformation from the fixed coordinate system to the ship's coordinate system is introduced. This is simply a frequency transformation that maps ω into the "frequency of encounter" ω_e by [80]

$$\omega_e = \omega - \frac{\omega^2}{g} V \cos \chi \tag{5.38}$$

where V is the ship's speed $(V > 0)$, χ is the ship's heading (relative to the sea), and g is the gravitational constant. Equation (5.37) now becomes

$$S_i(\omega) = \int_{-\pi/2}^{\pi/2} S_i(\omega, \theta)d\theta = \int_{-\pi/2}^{\pi/2} |R_i(\omega_e, \theta)|^2 S(\omega, \theta)d\theta, \quad i = 1, \ldots, 6. \tag{5.39}$$

6. UNIT-SCATTERER-MOTION SIMULATION

Our goal in this chapter is to develop a simulation of the 6 dof motions for the US geometric-centers which are caused by sea surface motion and ship maneuvering. It is well known that sea-induced motions can be accurately described as zero-mean Gaussian processes. The DTNSRDC has used the St. Denis-Pierson model of ship motion (described in Section 5) to generate, via simulations, libraries of ship-motion "spectra," which complete the specification of the processes. These "spectra" have been generated for various ships assuming various sea conditions and ship speeds. The method of RAOs described in Sec. 5.3.3 is used to generate the ship-motion "spectra" and time-domain realizations for the 6 dof motions of various locations on each ship. Some results of this work are presented in Refs. 78 and 79. Because we are interested in studying the ship motions per se and not in studying the physical processes by which these motions are generated, we base our motion model on the DTNSRDC "spectra."

6.1 Motion Model

Because we are assuming rigid body motion and that the sea-induced motions are small and uncoupled (assumptions consistent with the St. Denis-Pierson model), we only require knowledge of the cg motions and of the scatterer locations relative to the ship's cg. Given these, we use Eq. (5.17) to yield the position of the ith scatterer (relative to an Earth-coordinate system) as a function of time. We modify those equations here to be

$$\vec{R}_i(t) = \vec{R}_i(0) + T_i[\vec{x}_{cg}(t) - \vec{x}_{cg}(0)] \tag{6.1}$$

and

$$T_i = \begin{bmatrix} 1 & 0 & 0 & 0 & z_i & -y_i \\ 0 & 1 & 0 & -z_i & 0 & x_i \\ 0 & 0 & 1 & y_i & -x_i & 0 \end{bmatrix} \tag{6.2}$$

where $\vec{x}_{cg}(t)$ is the position vector (reduced state vector) of the ship's cg, and $\vec{R}_i(t)$ is the position vector of the ith scatterer, both in Earth coordinates.

Equation (6.1) was derived assuming small uncoupled motions. For our studies we are interested in scattering from various aspect angles. These aspect angles result from apparent translations and/or rotations of the ship relative to the radar. For example, the ship may be located at some position $\vec{R}_0$ and aspect angle ψ_0 relative to the radar boresight axis (Fig. 6.1). These large aspect variations are due to our choice of radar-ship orientation and to ship maneuvering. Our approach to accounting for these effects is to specify the sea-induced motions in a local coordinate system and then transform that solution to an Earth-coordinate system located at the radar. This allows us to retain the linear uncoupled solution Eq. (6.1), rather than the general nonlinear solution (from Eq. (5.16)),

$$\vec{R}_i(t) = \vec{R}_i(0) + \int_0^t \begin{bmatrix} u \\ v \\ w \\ p \\ q \\ r \end{bmatrix} d\tau. \tag{6.3}$$
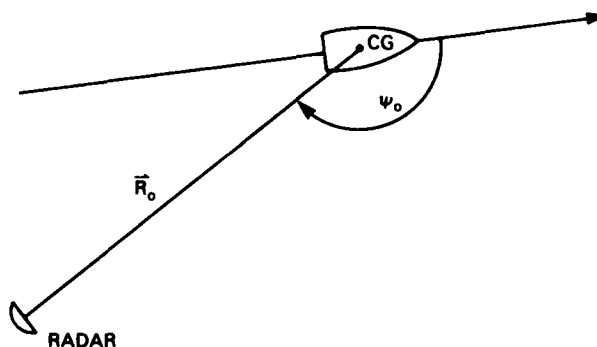
Fig. 6.1 — Aspect angle due to radar-ship positioning

We start building the simulation by assuming knowledge of the sea-induced ship-cg motion, $\vec{x}_{cg}(t)$. This motion is given in local (ship) Earth-axis coordinates. This local system is defined by the ship-axis and the Earth-axis systems being coincident for $\vec{x}_{cg}(t) = \vec{0}$. We then locate the ship-axis system in space according to ship maneuvering and positioning by the translation

$$\vec{R}_s(t) = \vec{R}_s(0) + \int_0^t \vec{V}_s(\tau)d\tau \tag{6.4a}$$

and the rotation

$$T_s(t) = \begin{bmatrix} \cos\psi\,\cos\theta & \cos\psi\,\sin\theta\,\sin\phi - \sin\psi\,\cos\phi & \cos\psi\,\sin\theta\,\cos\phi + \sin\psi\,\sin\phi \\ \sin\psi\,\cos\theta & \sin\psi\,\sin\theta\,\sin\phi + \cos\psi\,\cos\phi & \sin\psi\,\sin\theta\,\cos\phi - \cos\psi\,\sin\phi \\ -\sin\theta & \cos\theta\,\sin\phi & \cos\theta\,\cos\phi \end{bmatrix} \tag{6.4b}$$

where $\vec{V}_s(t)$ is the linear velocity of the ship's cg in Earth-coordinates, and ϕ, θ, and ψ here denote ship-axis system orientation relative to the radar-site Earth-axis system, not components of a motion vector. The position of the ith scatterer now becomes

39

$$\vec{R}_i^E(t) = T_s(t)\{\vec{R}_i^L(0) + T_i[\vec{x}_{cg}^L(t) - \vec{x}_{cg}^L(0)]\} + \vec{R}_s^E(t) \qquad (6.5a)$$

$$= T_s(t)\vec{R}_i^L(t) + \vec{R}_s^E(t) \qquad (6.5b)$$

where the superscript L denotes local Earth-coordinates and the superscript E denotes radar-site Earth-coordinates. We note that the sea-induced motion $\vec{x}_{cg}(t)$ is, in general, a function of ship maneuvering. Ship rotations due to maneuvering (included in $T_s(t)$) are not accounted for in the DTNSRDC data, and it is well known that in hard turns, ships' responses to the sea are not the same as in straight-line motion. Therefore we restrict our studies to maneuvers characterized by straight-line motions with constant forward speeds and/or turning maneuvers in which we assume that the turns are small enough that their resulting motions are independent of the sea-induced motions. This allows us to use the solutions $\vec{x}_{cg}(t)$ that are tabulated by DTNSRDC as a function of ship speed. Once we choose a ship speed (i.e., $\vec{V}_s(t)$) we then obtain the appropriate $\vec{x}_{cg}(t)$ processes.

Summarizing to this point: we begin our scatterer-motion model by assuming that the sea-induced and maneuvering motions are independent except that $\vec{V}_s(t)$ determines the choice of cataloged motions $\vec{x}_{cg}(t)$. We then solve Eq. (6.1) for sea-induced scatterer motions and then Eq. (6.5a) for maneuvering effects. Note that the sea-induced motions can be viewed as Gaussian perturbations of the maneuvering motion.

6.2 Model of the Spectrum

Equations (6.5) are our fundamental equations for calculating phase due to scatterer motion. They require three parameters for solution: ship position and orientation due to maneuvering, scatterer locations relative to the ship's cg, and ship's cg motion. Maneuvering is application-dependent and the scatterer locations are determined by target structure. The third parameter, $\vec{x}_{cg}(t)$, is always a zero-mean Gaussian process with spectra that are functions of ship type, ship speed, and sea conditions. This section discusses the simulation of $\vec{x}_{cg}(t)$.

We simulate $\vec{x}_{cg}(t)$ by using the method discussed in Sec. 5.3. There it is shown that we can approximate a Gaussian process with arbitrary energy "spectrum" $S(\omega)$ by Eq. (5.30),

$$\eta(t) \approx \sum_{i=1}^{N} \sqrt{2S(\omega_i)\Delta\omega_i} \cos(\omega_i t + \phi(\omega_i)) \qquad (6.6)$$

where the $\phi(\omega_i)$ are independent random variables uniformly distributed on $(0, 2\pi)$. The processes are completely determined by specifying the "spectrum" $S(\omega)$ for each component process. The "spectrum" can be defined by an analytical expression or by tabulated data.

Clearly, the motion spectra are our fundamental model inputs. DTNSRDC has calculated and tabulated, on microfiche, "spectra" for various ships and operating conditions. An example of this data is shown in Table 6.1. Reference 78 describes the DTNSRDC method and illustrates it with specific examples: cg motion for the DD963 moving at 10 knots in two sea conditions. Because detailed data for these examples are presented in Ref. 78, we use one of them to obtain the motion processes for the studies of this report. In particular, we use the processes resulting from the DD963 moving at 10 knots in a fully developed, shortcrested (irregular) Bretschneider-spectrum (Table 6.2) sea and moving at a 30°-heading relative to the dominant sea-wave direction. The associated motion "spectra" are shown in the third column of Fig. 6.2. Figure 6.3 illustrates the cosine-squared spectral weighting used to produce the shortcrested wave spectrum. Clearly, the spectral shapes vary considerably as a function of ship type, speed, heading, and sea conditions. Although the simulation can use the DTNSRDC data directly in specifying $S(\omega)$ in Eq. (6.6), we prefer to use an analytical expression. This allows analytical formulations in analyses involving the motion processes and more flexibility in the simulation. However, in doing so, we must approximate the spectral forms. This is not a significant problem because we are concerned with very short time periods (on the order of 1 s) for the scattered signal to evolve relative to the time required for the motion processes to evolve significantly (on the order of tens of

Table 6.1 — An example of the Tabulated DTNSRDC Motion-Spectra (from Ref. 78)

DD 963

SHORTCRESTED
RMS VER DISP IN FEET/ENCOUNTERED MODAL PERIOD, T_{OE}, IN SECONDS
CENTER OF GRAVITY - 258.7 FT FORWARD OF AP AND 21.9 FT FROM DL
SHIP HEADING ANGLE IN DEGREES

VT		0	15	30	45	60	75	90	105	120	135	150	165	180
5	7	.034/ 9.5	.048/ 8.3	.074/ 7.9	.101/ 7.5	.124/ 7.0	.141/ 7.0	.149/ 7.0	.148/ 7.0	.138/ 6.8	.120/ 6.7	.098/ 6.7	.075/ 6.7	.064/ 6.8
	9	.071/12.6	.081/12.1	.105/11.6	.132/10.1	.155/ 9.8	.172/ 9.5	.181/ 9.2	.179/ 9.0	.169/ 9.0	.151/ 9.0	.128/ 9.0	.107/ 9.0	.098/ 9.2
	11	.114/14.0	.121/14.0	.138/13.4	.160/13.1	.180/12.6	.195/12.1	.202/11.6	.200/11.2	.190/11.2	.176/11.2	.155/11.2	.139/11.2	.133/11.2
	13	.150/15.7	.155/15.3	.167/15.3	.184/14.6	.200/14.3	.211/13.7	.217/13.6	.215/13.1	.207/12.8	.194/12.6	.180/12.6	.168/12.6	.163/12.6
	15	.177/17.5	.181/17.0	.190/17.0	.202/16.5	.214/61.1	.223.15.7	.228/15.3	.226/15.0	.220/14.6	.210/14.3	.199/14.3	.190/14.3	.187/14.3
	17	.195/19.0	.198/19.0	.205/19.0	.214/18.5	.224/15.0	.231/17.5	.236/17.0	.233/17.0	.224/16.5	.206/16.5	.220/16.5	.206/16.5	.203/16.5
	19	.208/19.6	.210/19.6	.216/19.6	.223/19.6	.230/19.6	.236/19.0	.238/19.0	.238/18.5	.234/18.0	.228/18.0	.222/18.0	.217/17.5	.215/17.5
	21	.219/22.4	.221/22.4	.225/22.4	.230/21.7	.236/21.7	.240/20.9	.242/20.9	.242/20.3	.239/20.3	.234/12.6	.230/19.6	.216/19.6	.225/19.6
10	7	.032/13.4	.046/10.1	.073/ 7.9	.101/ 7.5	.126/ 7.0	.143/ 7.0	.153/ 7.0	.153/ 6.8	.144/ 6.8	.127/ 6.8	.104/ 7.0	.081/ 7.1	.071/ 7.3
	9	.069/15.0	.079/15.0	.103/12.1	.131/10.5	.157/ 9.8	.176/ 9.2	.187/ 9.0	.188/ 9.0	.180/ 8.7	.164/ 8.5	.143/ 8.5	.124/ 8.5	.116/ 8.5
	11	.111/16.1	.118/16.1	.136/15.7	.159/15.3	.180/13.4	.197/12.1	.207/11.6	.208/11.2	.201/11.2	.187/10.8	.171/10.8	.157/10.4	.151/10.8
	13	.146/17.5	.151/17.5	.164/17.0	.182/16.5	.199/15.7	.212/14.6	.220/13.7	.221/13.4	.215/12.8	.204/12.6	.192/12.6	.181/12.6	.177/12.6
	15	.173/19.0	.177/19.0	.187/18.5	.200/18.0	.213/17.5	.223/16.5	.229/15.7	.230/15.0	.226/14.4	.217/14.6	.208/14.3	.200/14.3	.197/14.5
	17	.192/20.9	.194/20.3	.202/20.3	.212/19.6	.222/19.0	.230/18.0	.235/17.5	.235/17.0	.232/16.5	.226/ 1.5	.219/16.5	.213/ 1.6	.211/16.5
	19	.205/21.7	.207/21.7	.213/21.7	.221/21.7	.229/20.9	.235.20.3	.239/19.6	.239/19.0	.237/18.5	.232/18.0	.227/18.0	.222/18.0	.221/17.5
	21	216/24.2	.218/24.2	.222/24.2	.228/23.3	.234/22.4	.239/21.7	.242/20.9	.243/20.3	.241/20.3	.237/19.6	.233/19.6	.230/19.6	.229/19.6
15	7	.031/14.6	.045/ 8.7	.072/ 8.3	.101/ 7.0	.126/ 7.0	.145/ 7.0	.155/ 7.0	.156/ 7.0	.147/ 7.0	.131/ 7.1	.108/ 7.3	.086/ 7.5	.075/ 7.5
	9	.067/19.6	.077/19.6	.101/12.5	.131/12.1	.159/ 9.2	.180/ 9.0	.196/ 8.7	.198/ 8.5	.193/ 8.3	.179/ 8.3	.161/ 8.3	.144/ 8.3	.137/ 8.3
	11	.108/20.3	.115/20.3	.133/20.3	.157/20.3	.181/12.8	.200/12.6	.213/11.6	.218/11.2	.214/10.8	.205/10.5	.192/10.1	.180/10.1	.175/10.1
	13	.143/20.3	.148/20.3	.161/20.3	.180/20.3	.198/15.7	.214/15.3	.224/14.0	.228/13.4	.226/12.8	.219/12.6	.209/12.6	.201/12.6	.197/12.6
	15	.170/21.7	.173/21.7	.183/21.2	.197/20.9	.212/20.3	.224/17.5	.235/15.7	.236/15.3	.236/15.0	.228/14.6	.221/14.3	.215/14.3	.213/14.3
	17	.188/22.4	.191/22.4	.191/22.4	.209/22.4	.221/20.9	.230/20.3	.237/14.0	.240/17.5	.238/17.0	.234/16.3	.229/16.5	.224/16.5	.222/16.5
	19	.202/24.2	.200/24.2	.210/24.2	.218/23.3	.227/22.4	.235/20.9	.240/20.3	.242/19.6	.241/19.0	.238/18.0	.234/18.0	.231/17.5	.229/17.5
	21	.213/26.2	.215/26.2	.219/25.1	.226/25.1	.233/24.2	.239/23.3	.243/20.9	.245/20.°	.244/20.3	.242/19.6	.239/19.6	.236/19.6	.235/19.6
20	7	.030/13.7	.044/13.7	.071/13.7	.100/ 7.0	.126/ 7.0	.145/ 7.0	.155/ 7.0	.156/ 7.0	.148/ 7.1	.132/ 7.1	.109/ 7.7	.087/ 7.7	.076/ 7.7
	9	.064/19.0	.075/19.0	.100/19.0	.130/19.0	.160/ 9.5	.184/ 9.0	.200/ 8.5	.206/ 8.3	.204/ 8.3	.192/ 8.5	.177/ 8.5	.162/ 8.5	.155/ 8.5
	11	.104/23.3	.111/23.3	.131/23.3	.156/23.3	.182/19.0	.204/11.6	.220/11.2	.228/10.8	.229/10.1	.223/ 9.8	.213/ 9.5	.204/ 9.2	.201/ 9.2
	13	.138/26.2	.144/26.2	.158/26.2	.158/26.2	.178/23.3	.198/23.3	.217/15.0	.230/14.0	.238/13.7	.239/12.6	.235/12.4	.229/12.1	.223/11.6
	15	.166/26.2	.169/26.2	.180/26.2	.195/26.2	.211/23.3	.226/19.0	.235/15.7	.243/15.3	.244/15.0	.242/14.6	.237/16.3	.233/14.3	.232/14.3
	17	.184/27.3	.187/27.3	.195/27.3	.207/26.2	.220/26.2	.231/19.6	.240/19.0	.245/17.5	.246/17.0	.244/16.5	.241/16.5	.238/16.5	.237/16.5
	19	.199/27.3	.201/27.3	.207/27.3	.216/27.3	.226/26.2	.235/23.3	.242/20.3	.246/19.6	.247/19.6	.246/18.0	.244/18.0	.242/17.5	.241/17.5
	21	.211/28.6	.212/27.3	.217/27.3	.224/27.3	.232/27.3	.239/26.2	.245/23.3	.248/20.9	.249/20.3	.248/19.6	.247/19.4	.245/19.6	.244/19.6
25	7	.030/16.5	.044/16.5	.071/16.5	.100/16.5	.125/16.5	.144/ 7.0	.154/ 7.0	.155/ 7.1	.146/ 7.5	.130/ 7.5	.107/ 7.7	.084/ 7.9	.073/ 8.1
	9	.062/16.5	.073/16.5	.099/16.5	.130/16.5	.161/16.5	.186/16.5	.204/16.5	.212/ 8.5	.211/ 8.5	.201/ 8.7	.186/ 8.7	.172/ 8.7	.166/ 8.7
	11	.101/33.1	.109/33.1	.129/16.5	.155/16.5	.183/16.5	.208/16.5	.226/11.2	.238/10.5	.241/ 9.8	.238/ 9.2	.231/ 9.2	.224/ 9.2	.221/ 9.2
	13	.136/33.1	.141/33.1	.156/33.1	.176/24.2	.199/.24.2	.219/16.5	.236/13.4	.247/13.1	.252/12.6	.252/12.1	.248/11.2	.245/11.2	.243/11.2
	15	.163/33.1	.167/33.1	.178/33.1	.194/33.1	.211/24.2	.228/16.5	.241/16.5	.250/16.5	.255/14.6	.256/14.3	.256/14.3	.252/14.3	.251/14.3
	17	.182/33.1	.185/33.1	.194/33.1	.206/33.1	.219/24.2	.233/24.2	.243/18.0	.251/17.5	.255/17.0	.256/16.5	.255/16.5	.253/16.5	.253/16.5
	19	.197/33.1	.199/33.1	.206/33.1	.215/33.1	.226/33.1	.236/24.2	.245/20.3	.251/19.6	.256/19.6	.255/18.0	.255/18.0	.254/17.5	.253/17.5
	21	.209/33.1	.211/33.1	.216/33.1	.223/33.1	.232/33.1	.240/24.2	.247/24.2	.252/20.9	.255/20.3	.256/19.6	.255/19.6	.255/19.6	.254/19.6

NOTE: V is ship speed in knots and T_0 is model wave period in seconds.

Table 6.2 — Bretschneider Spectrum and Associated Statistics (from Ref. 78)

Single Amplitude Statistics	σ	Bretschneider Spectrum $S_\zeta(\omega)$		
Root mean square amplitude, rms	1.00	$S_\zeta(\omega)$	=	$A\omega^{-5} \exp[-\beta/\omega^4]$ in ft^2/s
Average amplitude	1.25	A	=	$483.5\ (\tilde{\zeta}_w)^2_{1/3}/T_0^4$, ft^{2}s^{-4}
Average of highest 1/3 amplitudes, significant	2.00	B	=	$1944.5/T_0^4$, s^{-4}
Highest expected amplitude in 10 successive amplitudes	2.15	$(\tilde{\zeta}_w)_{1/3}$	=	Average of highest 1/3 wave heights
Average of highest 1/10 amplitudes	2.55	T_0	=	Modal period of spectrum, i.e., period corresponding to peak of spectrum
Highest expected amplitude in 30 successive amplitudes	2.61			
Highest expected amplitude in 50 successive amplitudes	2.80			
Highest expected amplitude in 100 successive amplitudes	3.03			
Highest expected amplitude in 200 successive amplitudes	3.25			
Highest expected amplitude in 1000 successive amplitudes	3.72			

N = Number of successive amplitudes

CONSTANT = $\sqrt{2}\,(\ln N)^{1/2}$, where CONSTANT relates σ to the highest expected amplitude in N successive amplitudes.

The highest expected amplitude in N amplitudes is the most probable extreme value in N amplitudes. This value may be exceeded 63% of the time.

To obtain wave height or double amplitude statistics from rms values, multiply single amplitude constants by 2.0.

DD 963 SHORTCRESTED RESPONSE SPECTRA
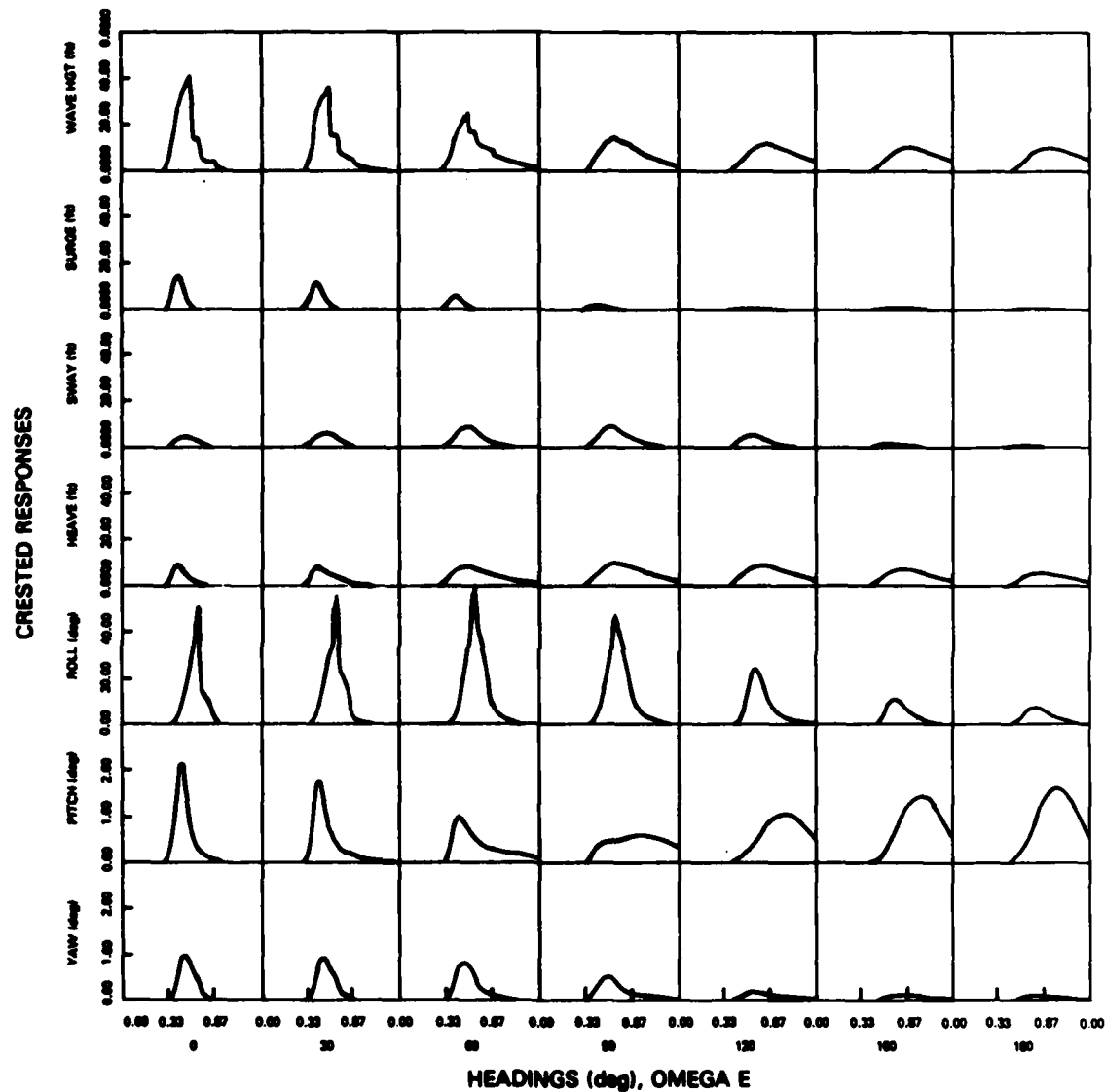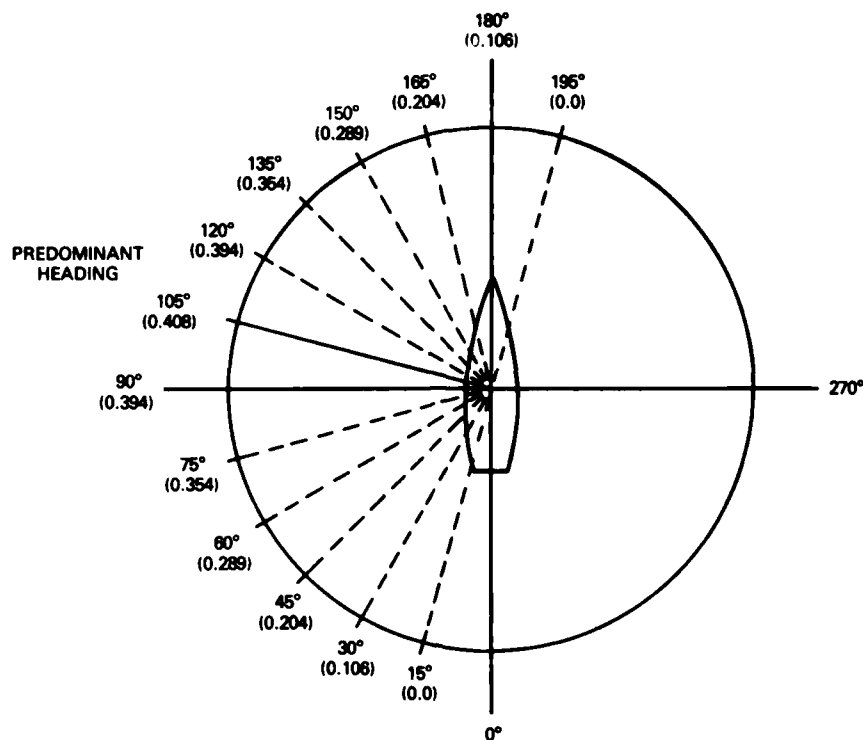SPEED = 10.0000 SIGWH = 10.0000 TMODL = 11.0000

CRESTED RESPONSES

HEADINGS (deg), OMEGA E

Fig. 6.2 — Tabulated spectra for the DD963 (from Ref. 78)

Fig. 6.3 — Shortcresting scheme for the example wave spectrum (from Ref. 78)

seconds). In other words, a ship does not move very far in 1 s. Therefore, in generating the scattering processes we generate very short "pieces" (realizations) of the motion processes. We quantify this observation in later paragraphs.

6.3 Spectrum Algorithm in the Simulation

Visual examination of the spectra yields the following observations: they typically are unimodal, are band-pass, are asymetrical about the mode with more energy in the higher frequencies, and have negligible energy in very low frequencies. These characteristics and the desire for simplicity led us to propose using a spectrum of the form (following the notation of Eqs. (5.28a) and (5.28b))

$$F_a(\omega) = \frac{\alpha}{\alpha^2 + (\omega - \omega_0)^2} + \frac{\alpha}{\alpha^2 + (\omega + \omega_0)^2} \qquad (6.7)$$

to approximate the motion spectra. For the appropriate choice of ω_0 and α, the spectral approximation is, for $\omega > 0$, characterized as being unimodal, band-pass, symmetric about the mode, of simple analytic form, and $F(0) \ll F(\omega_0)$ (Fig. 6.4). In the simulation we alter the upper and lower spectral tails to introduce assymetry. (The author's experience has been that Eq. (6.7) often well characterizes the spectrum of measured data and may be a better approximation to the spectra of physical processes than the commonly used low-pass form

$$F(\omega) = \frac{2\alpha}{\alpha^2 + \omega^2}, \qquad (6.8)$$
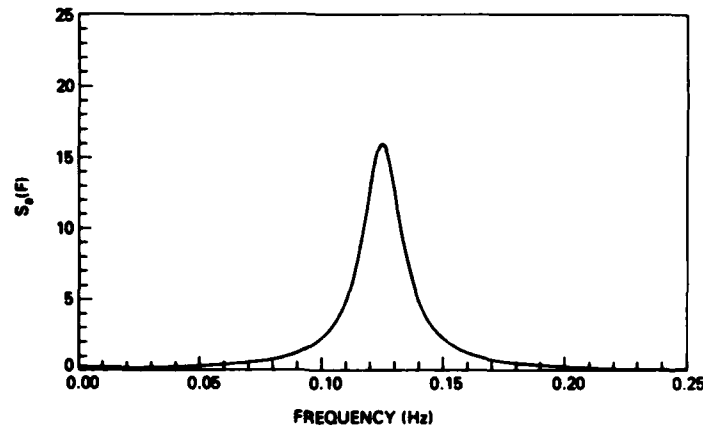
Fig. 6.4 — Approximation spectrum for $\omega \geqslant 0$ and $S_a(0) \ll S_a(\omega_0)$

especially when $\omega_0 \approx \alpha$ so that $F(\omega)$ has the form shown in Fig. 6.5; note that Eq. (6.7) becomes Eq. (6.8) when $\omega_0 = 0$.) The autocovariance function of the associated energy spectrum $(S_a(\omega) = 2F(\omega), \omega \geqslant 0)$ is

$$R_a(\tau) = \int_0^\infty 2F_a(\omega) \cos (\omega\tau) d\omega$$

$$= 2\pi e^{-\alpha|\tau|} \cos \omega_0\tau. \tag{6.9}$$
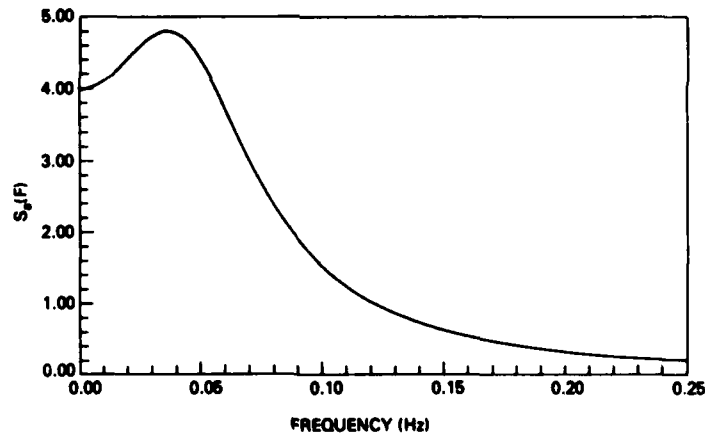
Fig. 6.5 — Approximation spectrum for $\omega > 0$ and $\alpha \approx \omega_0$

In fitting Eq. (6.7) to the forms of Fig. 6.2, we specify five parameters: ω_0, α, σ^2 (the process variance), f_l, and f_u (lower and upper cutoff frequencies). Clearly, ω_0 corresponds to the center frequency of the process. We choose α based on the concept of bandwidth. If $S_a(0) \ll S_a(\omega_0)$, we define the half-power bandwidth BW as the distance (in radians) between the frequencies where $S_a(\omega) = \frac{1}{2} S_a(\omega_0)$. Since

$$S_a(\omega_0) \approx \frac{1}{\alpha},$$

we solve

$$S_a(\omega_{1/2}) = \frac{1}{2\alpha} = \frac{\alpha}{\alpha^2 + (\omega - \omega_0)^2}$$

45

yielding

$$\omega_{1/2} - \omega_0 = \pm \, \alpha$$

or

$$\omega_{1/2}^{\pm} = \omega_0 \pm \alpha. \tag{6.10}$$

The process half-power bandwidth is defined by

$$BW = \omega_{1/2}^{+} - \omega_{1/2}^{-}$$

so that

$$\alpha = \frac{BW}{2}. \tag{6.11}$$

We modify Eq. (6.7) for the simulation to introduce an asymmetry effect by specifying asymmetric upper and lower cutoff frequencies. For simplicity, we choose the lower frequency to be $f_l = \omega_0 - BW$ and the upper frequency to be $f_u = \omega_0 + 2BW$. The resulting spectral shape is illustrated in Fig. 6.6. Finally, we must specify the variance of the process. Reference 71 gives the spectral forms and the associated rms values (standard deviations) for the component processes. To generate a realization with the same rms value, we first generate a realization with a variance of one and then multiply by the desired rms value. The variance σ^2 of the truncated spectrum process is

$$\sigma^2 = \int_{\omega_0 - BW}^{\omega_0 + 2BW} \left\{ \frac{2\alpha}{\alpha^2 + (\omega - \omega_0)^2} + \frac{2\alpha}{\alpha^2 + (\omega + \omega_0)^2} \right\} d\omega$$

$$= 2 \left\{ \tan^{-1} \frac{2BW}{\alpha} + \tan^{-1} \frac{BW}{\alpha} + \tan^{-1} \left[\frac{2\omega_0 + 2BW}{\alpha} \right] - \tan^{-1} \left[\frac{2\omega_0 - BW}{\alpha} \right] \right\}$$

$$= 2 \left\{ \tan^{-1} 4 + \tan^{-1} 2 + \tan^{-1} \left[4 \frac{\omega_0}{BW} + 4 \right] - \tan^{-1} \left[4 \frac{\omega_0}{BW} - 2 \right] \right\}. \tag{6.12}$$

For our example (Appendix A), ω_0/BW varies from about 2.5 to about 3.5. For simplicity, and with minimal loss of accuracy, we set $\omega_0/BW = 3$ so that $\sigma^2 \approx 4.940$. Therefore we normalize the simulated process by

$$F = \left[\frac{1}{4.940} \right]^{1/2} \text{rms} \{\eta(t)\}$$

$$= 0.45 \text{ rms} \{\eta(t)\} \tag{6.13}$$

where rms $\{\eta(t)\}$ is the desired rms value for the simulated $\eta(t)$ process.
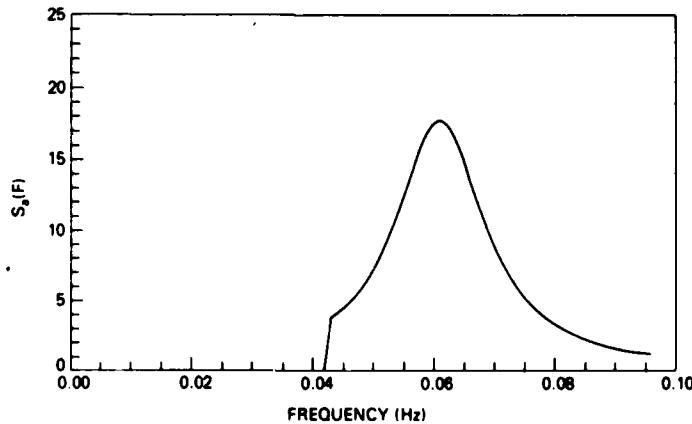

Fig. 6.6 — Truncated spectral form used in the simulation

7. RADAR CROSS SECTION

In this section we develop equations for the RCS of an N-source target in terms of unit-scatterers. Multipath effects are accounted for by using the model described in Section 4. The transmit and receive polarizations are assumed to be the same; no cross-polarization effects are considered. We will focus our attention on the correlation properties of RCS over short time-intervals.

7.1 Fundamental Representation

In Section 3 we showed that the RCS of a target comprised of N USs is

$$\sigma(t) = \left| \sum_{i=1}^{N} \hat{p}_T^T X_i(\vec{R}_i, \vec{\theta}_i) \hat{p}_R \right|^2 \tag{7.1}$$

where, for the ith US, $\hat{p}_T$ is the transmitter polarization vector, $\hat{p}_R$ is the receiver polarization vector, $\vec{\theta}_i$ defines the US orientation (as a function of time), and R_i defines the US-to-radar range (as a function of time). For simplicity we assume that $\hat{p}_T = \hat{p}_R = (1, 0)^T$ so that (from Eq. (3.8a))

$$\sigma(t) = \left| \sum_{i=1}^{N} A_{11_i}(\vec{\theta}_i) e^{j\phi_{11_i}(\vec{R}_i, \vec{\theta}_i)} \right|^2. \tag{7.2}$$

For practical reasons, measurements of ship RCS at low-grazing angles must include the effects of sea-surface multipath. Therefore we include a model of multipath effects in our representation of RCS by modifying Eq. (7.2) by the complex multipath factor $F(\vec{R}, \vec{\theta})$ (described in Sec. 4.4) yielding

$$\sigma = \left| \sum_{i=1}^{N} F^2(\vec{R}_i, \vec{\theta}_i) A_{11_i}(\vec{R}_i, \vec{\theta}_i) e^{j\phi_{11_i}(\vec{R}_i, \vec{\theta}_i)} \right|^2. \tag{7.3}$$

As discussed in Section 4, $F^2(\vec{R}_i, \vec{\theta}_i)$ was obtained assuming that the US reradiates equally toward the radar and toward the sea-surface specular point (Fig. 4.2). This is a good approximation for small radar-grazing-angles and when the US amplitudes are not strongly dependent on elevation. Otherwise, the elevation radiation pattern must be viewed as an antenna pattern. This pattern is then accounted for by using the same method as was used to account for the radar's pattern in Sec. 4.4.

7.2 Useful Equations

Equation (7.3) is the fundamental equation that we use to model RCS. In this section we derive from Eq. (7.3) several other equations for RCS. These equations will prove useful for analysis and simulation. Suppressing the $\vec{R}_i$ and $\vec{\theta}_i$ terms of Eq. (7.3),

$$\sigma(t) = \left| \sum_{i=1}^{N} F_i^2 A_{11_i} e^{j\phi_{11_i}} \right|^2 \tag{7.4}$$

and associating $|F_i|^2$ with A_{11_i},

$$\sigma(t) = \left| \sum_{i=1}^{N} |F_i^2| A_{11_i} e^{j(\phi_{11_i} + \gamma_i)} \right|^2$$

$$= \left| \sum_{i=1}^{N} A_i e^{j\Psi_i} \right|^2. \tag{7.5}$$

Expanding Eq. (7.5),

$$\sigma(t) = \left[\sum_{i=1}^{N} A_i \cos \Psi_i\right]^2 + \left[\sum_{i=1}^{N} A_i \sin \Psi_i\right]^2$$

$$= \sum_{i=1}^{N} A_i \cos \Psi_i \sum_{j=1}^{N} A_j \cos \Psi_j + \sum_{i=1}^{N} A_i \sin \Psi_i \sum_{j=1}^{N} A_j \sin \Psi_j$$

$$= \sum_{i=1}^{N} \sum_{j=1}^{N} A_i A_j [\cos \Psi_i \cos \Psi_j + \sin \Psi_i \sin \Psi_j] \tag{7.6}$$

and hence

$$\sigma(t) = \sum_{i=1}^{N} \sum_{j=1}^{N} A_i A_j \cos (\Psi_i - \Psi_j) \tag{7.7a}$$

and

$$\sigma(t) = 2 \sum_{\substack{i=1 \\ i \neq j}}^{N} \sum_{j=1}^{N} A_i A_j \cos (\Psi_i - \Psi_j) + \sum_{i=1}^{N} A_i^2. \tag{7.7b}$$

For the ith US, let $\beta_i(\cdot)$ account for the orientation effects on phase and $\gamma_i(\cdot)$ the multipath effects so that

$$\Psi_i(\vec{R}_i, \vec{\theta}_i) = \left[\frac{2\pi}{\lambda}\right] 2 |\vec{R}_i| + \beta_i(\vec{\theta}_i) + \gamma_i(\vec{R}_i, \vec{\theta}_i) \tag{7.8}$$

and

$$\Psi_i - \Psi_j = \frac{4\pi}{\lambda} (|\vec{R}_i| - |\vec{R}_j|) + \beta_i(\vec{\theta}_i) - \beta_j(\vec{\theta}_j) + \gamma_i(\vec{R}_i, \vec{\theta}_i) - \gamma_j(\vec{R}_j, \vec{\theta}_j). \tag{7.9}$$

Equations (7.7a) and (7.9) are our fundamental equations for simulating RCS. In the simulation, the $A_i(\cdot)$ and $\beta(\cdot)$ functions are user controlled, the $\vec{R}_i$ terms are generated by the ship motion (Section 5), and the $\gamma_i(\cdot)$ terms are generated by using the model in Section 4.

As suggested by Eqs. (7.5) and (7.2), we define a complex scattering function $s(t)$ to simplify notation:

$$s(t) = \sum_{i=1}^{N} A_i e^{j\Psi_i}. \tag{7.10}$$

Note that $\sigma(t) = s(t)s^*(t)$.

7.3 Statistics for an N-Source Target

In this section we investigate the first and second moments of the RCS process. We show that over short time-intervals the RCS process can be nonstationary and analytically complex even when simplifying assumptions are made regarding the scatterers. We also investigate in what sense the well-known random-phase model (resulting in Rayleigh-amplitude statistics) is a limiting case of the general formulation. We use the notation of $\sigma(t)$ for RCS and $\sigma_i(t)$ for standard deviation of the ith phase process; no confusion will result given both the context and the subscripting (standard deviations only).

7.3.1 Mean and Correlation Functions

Because the amplitude functions are much less sensitive to target motion than the phase functions are, over short time intervals they can be well approximated by deterministic functions (typically as

constants, except for specular scatterers). However, even ignoring the US orientation and multipath effects, the phase functions are rapidly varying, nonlinear functions of target motion. Therefore we view the phase terms as stochastic processes.

Given an N-source target with deterministic amplitudes $A_i(t)$ and stochastic phases $\theta_i(t)$, the target RCS is

$$\sigma(t) = \sum_{i=1}^{N} \sum_{k=1}^{N} A_i(t) A_k(t) \, e^{j[\theta_i(t) - \theta_k(t)]} \tag{7.11}$$

and the associated mean and autocorrelation functions are

$$E\{\sigma(t)\} = \sum_{i=1}^{N} \sum_{k=1}^{N} A_i(t) A_k(t) E\{e^{j[\theta_i(t) - \theta_k(t)]}\}, \tag{7.12}$$

and

$$E\{\sigma(t_1)\sigma(t_2)\} = \sum_{i=1}^{N} \sum_{k=1}^{N} \sum_{l=1}^{N} \sum_{m=1}^{N} A_i(t_1) A_k(t_1) A_l(t_2) A_m(t_2) E\{e^{j[(\theta_i - \theta_k)(t_1) + (\theta_l - \theta_m)(t_2)]}\}. \tag{7.13}$$

The expectations in Eqs. (7.12) and (7.13) suggest characteristic functions. Such functions are useful when the joint densities of the phase processes are known. Writing the characteristic functions in the form

$$\Phi_{ik}(\omega_i, t_i, \omega_k, t_k) = E\{e^{j\omega_i\theta_i(t_i) + j\omega_k\theta_k(t_k)}\} \tag{7.14a}$$

$$\Phi_{iklm}(\omega_i, t_i, \omega_k, t_k, \omega_l, t_l, \omega_m, t_m) = E\{e^{j\omega_i\theta_i(t_i) + \ldots + j\omega_m\theta_m(t_m)}\}, \tag{7.14b}$$

we have

$$E\{e^{j(\theta_i - \theta_k)(t)}\} = \Phi_{ik}(1, t, -1, t) \tag{7.15a}$$

(where we use the notation $(\theta_i - \theta_k)(t) = \theta_i(t) - \theta_k(t)$) and

$$E\{e^{j[(\theta_i - \theta_k)(t_1) + (\theta_l - \theta_m)(t_2)]}\} = \Phi_{iklm}(1, t_1, -1, t_1, 1, t_2, -1, t_2). \tag{7.15b}$$

Using this formulation in Eqs. (7.12) and (7.13) we obtain

$$E\{\sigma(t)\} = \sum_{i=1}^{N} A_i^2(t) + \sum_{\substack{i=1 \\ i \neq k}}^{N} \sum_{k=1}^{N} A_i(t) A_k(t) \Phi_{ik}(1, t, -1, t)$$

$$= \sum_{i=1}^{N} A_i^2(t) + 2 \sum_{i=1}^{N} \sum_{\substack{k=i+1 \\ i \neq k}}^{N} A_i(t) A_k(t) \Phi_{ik}(1, t, -1, t), \tag{7.16a}$$

$$E\{\sigma(t_1)\sigma(t_2)\} = \sum_{i=1}^{N} A_i^2(t_1) A_i^2(t_2) + \sum_{\substack{i=1 \\ i \neq l}}^{N} \sum_{l=1}^{N} A_i^2(t_1) A_l^2(t_2)$$

$$+ \sum_{\substack{i=1 \\ \text{except } i=k=l=m \\ \text{and } i=k \neq l=m}}^{N} \sum_{k=1}^{N} \sum_{l=1}^{N} \sum_{m=1}^{N} A_i(t_1) A_k(t_1) A_l(t_2) A_m(t_2) \Phi_{iklm}(1, t, -1, t_1, 1, t_2, -1, t_2), \tag{7.16b}$$

and

$$E\{r^2(t)\} = \sum_{i=1}^{N} A_i^4(t) + \sum_{\substack{i=1 \\ i \neq l}}^{N} \sum_{l=1}^{N} A_i^2(t) A_l^2(t) + \sum_{\substack{i=1 \\ i \neq k}}^{N} \sum_{k=1}^{N} A_i^2(t) A_k^2(t)$$

$$+ \sum_{\substack{i=1 \\ \text{except } i=k=l=m \\ \text{and } i=k \neq l=m}}^{N} \sum_{k=1}^{N} \sum_{l=1}^{N} \sum_{m=1}^{N} A_i(t) A_k(t) A_l(t) A_m(t) \Phi_{iklm}(1, t, -1, t_1, 1, t, -1, t). \tag{7.17}$$

49

In general the phase processes are complicated functions with probability laws that at best can only be approximated. Over long periods of time (relative to target-motion time constants) they most likely have probability density functions that are unimodal and symmetric when they are not viewed as modulo 2π (i.e., distributed over $(-\infty, \infty)$). This suggests a Gaussian approximation. If the phases can be represented by joint Gaussian processes, then the form of the associated characteristic functions are known; they are [95]

$$\Phi_{ik}(\omega_i, t_i, \omega_k, t_k) = e^{j[\omega_i \eta_i(t_i) + \omega_k \eta_k(t_k)] - \frac{1}{2}[\sigma_i^2(t_i)\omega_i^2 + 2r_{ik}(t_i, t_k)\omega_i \omega_k + \sigma_k^2(t_k)\omega_k^2]} \tag{7.18a}$$

and

$$\Phi_{iklm}(\omega_i, t_i, \omega_k, \omega_l, t_l, \omega_m, t_m) = e^{j\sum_{p=i}^{m}\omega_p \eta_p(t_p) - \frac{1}{2}\Omega^T \mu \Omega} \tag{7.18b}$$

where

$$\eta_i(t_i) = E\{\theta_i(t_i)\}, \tag{7.18c}$$

$$\sigma_i^2(t_i) = E\{[\theta_i(t_i) - \eta_i(t_i)]^2\}, \tag{7.18d}$$

$$r_{ik}(t_i, t_k) = \frac{E\{[\theta_i(t_i) - \eta_i(t_i)][\theta_k(t_k) - \eta_k(t_k)]\}}{\sigma_i(t_i)\sigma_k(t_k)} \tag{7.18e}$$

$$\Omega = (\omega_i, \omega_k, \omega_l, \omega_m)^T, \tag{7.18f}$$

and μ is the covariance matrix for θ_i, θ_k, θ_l, and θ_m with

$$\mu_{pq}(t_p, t_q) = E\{[\theta_p(t_p) - \eta_p(t_p)][\theta_q(t_q) - \eta_q(t_q)]\} \text{ for } p, q = i, k, l, n. \tag{7.18g}$$

We note that from Eq. (7.18a)

$$\Phi_{ik}(1, t, -1, t) = e^{j[\eta_i(t) - \eta_k(t)] - 1/2[\sigma_i^2(t) - 2r_{ik}(t,t) + \sigma_k^2(t)]} \tag{7.19a}$$

and from Eq. (7.18b),

$$\Phi_{iklm}(1, t_1, -1, t_1, 1, t_2, -1, t_2) = e^{jF_1 - 1/2F_2} \tag{7.19b}$$

where

$$F_1 = \eta_i(t_i) - \eta_k(t_k) + \eta_l(t_l) - \eta_m(t_m) \tag{7.19c}$$

and

$$\begin{aligned}
F_2 = &\mu_{ii}(t_1, t_1) - \mu_{ik}(t_1, t_1) + \mu_{il}(t_1, t_2) - \mu_{im}(t_1, t_2) \\
&- \mu_{ki}(t_1, t_1) + \mu_{kk}(t_1, t_1) - \mu_{kl}(t_1, t_2) + \mu_{km}(t_1, t_2) \\
&+ \mu_{li}(t_2, t_1) - \mu_{lk}(t_2, t_1) + \mu_{ll}(t_2, t_2) - \mu_{lm}(t_2, t_2) \\
&- \mu_{mi}(t_2, t_1) + \mu_{mk}(t_2, t_1) - \mu_{ml}(t_2, t_2) + \mu_{mm}(t_2, t_2).
\end{aligned} \tag{7.19d}$$

7.3.2 Random-Phase Model

We define a random phase model for RCS to be an N-source model in which the phases are represented by independent, uniformly distributed (over $(0, 2\pi)$) processes. Such models are widely used in analyzing the RCS of complex targets. They are useful because they greatly simplify the RCS analysis. They are valid when the time period of interest (for analysis) is large relative to the correlation times of the phase processes.

Because we are interested in RCS analysis and simulation over short time-intervals, it is important to consider in what sense the general formulation can be replaced by a random-phase model. Therefore in the following we examine the behavior of the first and second moments of RCS as the random-phase assumptions are approached.

We now consider the simplest random-phase model: assume that the scatterer amplitudes are equal and constant and that the individual phases are white-noise processes. To obtain the first two moments of this model we write

$$s(t) = \sum_{i=1}^{N} A_i e^{j\theta_i} = \sum_{i=1}^{N} A_i \cos \theta_i + j \sum_{i=1}^{N} A_i \sin \theta_i \qquad (7.20)$$

where we recall that $\sigma(t) = s(t) \, s^*(t)$. By the central limit theorem, the real and imaginary sums in Eq. (7.20) approach being Gaussian distributed for large N. Further, they are uncorrelated because

$$E\left\{ \sum_{i=1}^{N} A_i \cos \theta_i \sum_{k=1}^{N} A_k \sin \theta_k \right\} = A^2 \sum_{i=1}^{N} \sum_{k=1}^{N} E\{\cos \theta_i \sin \theta_k\}$$

$$= A^2 \sum_{i=1}^{N} E\{\cos \theta_i \sin \theta_i\} = A^2 \sum_{i=1}^{N} E\left\{ \frac{\sin^2 \theta_i}{2} \right\} = 0. \qquad (7.21a)$$

Clearly, the mean of each sum is zero. Now consider the variances:

$$E\left\{ \left(\sum_{i=1}^{N} A_i \cos \theta_i \right)^2 \right\} = A^2 E\left\{ \sum_{i=1}^{N} \cos \theta_i \sum_{k=1}^{N} \cos \theta_k \right\}$$

$$= A^2 \sum_{i=1}^{N} E\{\cos^2 \theta_i\}$$

$$= A^2 \sum_{i=1}^{N} \int_0^{2\pi} \frac{\cos^2 \theta_i}{2\pi} \, d\theta_i = \frac{NA^2}{2} \qquad (7.21b)$$

and similarly,

$$E\left\{ \left(\sum_{i=1}^{N} A \sin \theta_i \right)^2 \right\} = A^2 \sum_{i=1}^{N} E\{\sin^2 \theta_i\} = \frac{NA^2}{2}. \qquad (7.21c)$$

Because of the white-noise assumption, RCS is also a white-noise process. Finally, the RCS process,

$$\sigma(t) = |s(t)|^2 = \left(\sum_{i=1}^{N} A \cos \theta_i \right)^2 + \left(\sum_{i=1}^{N} A \sin \theta_i \right)^2, \qquad (7.22)$$

approaches being exponentially distributed because the summations are independent Gaussian processes (approximately) with zero means and equal variances [95]. From Eqs. (7.21b) and (7.21c),

$$E\{\sigma(t)\} = NA^2 \qquad (7.23a)$$

and because $\sigma(t)$ is exponentially distributed,

$$E\{\sigma^2(t)\} = 2N^2 A^4. \qquad (7.23b)$$

Next we consider Eqs. (7.16) in the context of the random-phase assumption. We assume that the phases can be represented by Gaussian processes and, for simplicity, we assume that the means of the individual phase processes are zero. Therefore Eqs. (7.16) become

$$E\{\sigma(t)\} = \sum_{i=1}^{N} A_i^2(t) + 2 \sum_{i=1}^{N} \sum_{k=i+1}^{N} A_i(t) A_k(t) e^{-1/2[\sigma_i^2(t) - 2r_{ik}(t,t) + \sigma_k^2(t)]} \qquad (7.24)$$

and

$$E\{\sigma(t_1)\sigma(t_2)\} = \sum_{i=1}^{N} A_i^2(t_1)A_i^2(t_2) + \sum_{i=1}^{N}\sum_{\substack{l=1 \\ i \neq l}}^{N} A_i^2(t_1)A_l^2(t_2)$$

$$+ \sum_{\substack{i=1 \\ \text{except } i=k=l=m \\ \text{and } i=k \neq l=m}}^{N}\sum_{k=1}^{N}\sum_{l=1}^{N}\sum_{n=1}^{N} A_i(t_1)A_k(t_1)A_l(t_2)A_m(t_2)e^{-1/2\Sigma_{iklm}(t_1,t_2)} \qquad (7.25a)$$

where

$$\Sigma_{iklm}(t_1, t_2) = \sigma_i^2(t_1) + \sigma_k^2(t_1) + \sigma_l^2(t_2) + \sigma_m^2(t_2)$$

$$- 2r_{ik}(t_1, t_1)\sigma_i(t_1)\sigma_k(t_1) - 2r_{lm}(t_2, t_2)\sigma_l(t_2)\sigma_m(t_2)$$

$$+ 2r_{il}(t_1, t_2)\sigma_i(t_1)\sigma_l(t_2) + 2r_{km}(t_1, t_2)\sigma_k(t_1)\sigma_m(t_2)$$

$$- 2r_{im}(t_1, t_2)\sigma_i(t_1)\sigma_m(t_2) - 2r_{kl}(t_1, t_2)\sigma_k(t_1)\sigma_l(t_2). \qquad (7.25b)$$

Now assume that the θ_is are not cross correlated. In the limit of large variances,

$$\lim_{\substack{\sigma_i^2 \to \infty \\ \forall i}} E\{\sigma(t)\} = \sum_{i=1}^{N} A_i^2(t) \qquad (7.26)$$

and

$$\lim_{\substack{\sigma_i^2 \to \infty \\ \forall i}} E\{\sigma(t_1)\sigma(t_2)\} = \sum_{i=1}^{N} A_i^2(t_1)A_i^2(t_2) + \sum_{i=1}^{N}\sum_{\substack{l=1 \\ i \neq l}}^{N} A_i^2(t_1)A_l^2(t_2)$$

$$+ \sum_{i=1}^{N}\sum_{\substack{l=1 \\ i \neq l}}^{N} A_i(t_1)A_i(t_2)A_l(t_1)A_l(t_2)e^{-1/2\Sigma_{illi}^{uc}(t_1,t_2)} \qquad (7.27a)$$

where the function in the exponent is

$$\Sigma_{illi}^{uc}(t_1, t_2) = [\sigma_i^2(t_1) + \sigma_i^2(t_2) + \sigma_l^2(t_1) + \sigma_l^2(t_2) - 2R_i(t_1, t_2) - 2R_l(t_1, t_2)] \qquad (7.27b)$$

($R_i(t_1, t_2)$ is an autocovariance function). (The third sum-term in Eq. (7.27a) remains because even for σ_i^2 large, as $(t_2 - t_1)$ approaches zero Eq. (7.27b) approaches zero; in other words as t_2 approaches t_1, even for σ_i^2 large, $[\theta_i(t_1) - \theta_m(t_2)]$ and $[\theta_k(t_1) - \theta_l(t_2)]$ approach zero when $i = m$ and $k = l$.) For $t_1 = t_2 = t$, Eq. (7.27a) becomes

$$\lim_{\substack{\sigma_i^2 \to \infty \\ \forall i}} E\{\sigma^2(t)\} = \sum_{i=1}^{N} A_i^4(t) + 2 \sum_{i=1}^{N}\sum_{\substack{k=1 \\ i \neq k}}^{N} A_i^2(t)A_k^2(t). \qquad (7.28)$$

Equations (7.26) and (7.27) imply that even if the variances are time-varying, as they become large the RCS process becomes wide-sense stationary, assuming the amplitudes are constant. Equation (7.27b) shows that the RCS process can remain correlated even for large $\sigma_i(\cdot)$ if the individual phase processes remain strongly correlated.

Next we assume that $A_i(t) = A_j(t) = A$. Then Eqs. (7.26) and (7.28) become

$$\lim_{\substack{\sigma_i^2 \to \infty \\ \forall i}} E\{\sigma(t)\} = NA^2 \qquad (7.29a)$$

and

$$\lim_{\substack{\sigma_i^2 \to \infty \\ \forall i}} E\{\sigma^2(t)\} = [N + 2N(N-1)]A^4 = 2N^2 \left(\frac{2N-1}{2N}\right)A^4, \qquad (7.29b)$$

and Eq. (7.27a) becomes

$$\lim_{\substack{\sigma_i^2 \to \infty \\ \forall i}} E\{\sigma(t_1)\sigma(t_2)\} = NA^4 + N(N-1) A^4 + A^4 \sum_{i=1}^{N} \sum_{l=1}^{N} e^{-1/2\Sigma \frac{uc}{lll}}. \tag{7.30}$$

Assuming equal and constant variance functions in Eq. (7.30), $(R_i = R_A, \sigma_i = \sigma_A, i = 1, \ldots, N)$,

$$\lim_{\substack{\sigma_i^2 \to \infty \\ \forall i}} E\{\sigma(t_1)\sigma(t_2)\} = N^2 A^4 + A^4 \sum_{i=1}^{N} \sum_{l=1}^{N} e^{-2[\sigma_A^2 - R_A(t_1, t_2)]}$$

$$= N^2 A^4 \left[1 + \frac{N(N-1)}{N^2} e^{-2[\sigma_A^2 - R_A(t_1, t_2)]} \right]. \tag{7.31}$$

We see from Eq. (7.31) that the RCS process remains correlated if the individual phase processes remain correlated (not white noise).

For real targets the phase variances remain finite and the phase processes are not white-noise processes. It is likely to be the case that for target motions that produce large phase variances (over $(-\infty, \infty)$), the phase process (due primarily to geometric-center motion) will be strongly correlated. Clearly, for high sampling rates (short time between samples), the correlation of the phase processes cannot be ignored.

7.3.3 Range-Variation Effects

Next we consider a specific model of the geometric-center motion to further illustrate the difficulty of modeling phase variations over short time-intervals. Ignoring US orientation and multipath effects we have

$$\sigma(t) = \sum_{i=1}^{N} \sum_{j=1}^{N} A_i A_j \cos \frac{4\pi}{\lambda} (|\vec{R}_i(\omega, t)| - |\vec{R}_j(\omega, t)|). \tag{7.32}$$

The range process, $\vec{R}_i(\omega, t)$, is (Eq. (6.5)),

$$\vec{R}_i^E(\omega, t) = T_s(t)\vec{R}_i^L(\omega, t) + \vec{R}_s^E(t). \tag{7.33}$$

The stochastic component of Eq. (7.33) is $\vec{R}_i^L(\omega, t)$; it is a linear combination of Gaussian processes and therefore is Gaussian. The ship maneuvering terms, $T_s(t)$ and $\vec{R}_s^E(t)$, are deterministic, and over small time-intervals can be approximated by linear functions of time. If $T_s(t)$ and $\vec{R}_s^E(t)$ were constant, then $\vec{R}_i^E(\omega, t)$ would be a three-dimensional Gaussian process. If in addition, each component of $\vec{R}_i^E(\omega, t)$ had a mean of zero and equal variances (which they do not), then $|\vec{R}_i^E(\omega, t)|$ would be Maxwell distributed [95].

Clearly, the $|\vec{R}_i(\omega, t)|$ process is in general nonstationary and analytically complex. Even assuming that the ship does not maneuver, all that can be said in general about $|\vec{R}_i^E(\omega, t)|$ is that it is a nonlinear transformation of large-time-constant Gaussian processes (relative to a radar's PRI), is oscillatory and positive, and probably has a density function that is symmetric about a mode. Relative to a radar's PRI, long time periods may be required to produce realizations of $|\vec{R}_i(\omega, t)|$ that exhibit stationary statistics.

As a specific example, we investigate range-induced variations in the RCS phase for our example ship. We assume a (moderately high) radar frequency of 10 GHz ($\lambda = 3$ cm). Over short intervals the $|\vec{R}_i(\omega, t)|$ processes vary slowly (a numerical estimate is made in Appendix B) and therefore we will model them as linear functions of the form

$$|\vec{R}_i(\omega, t)| = R_i^0(\omega) + V_i(\omega, t)t. \tag{7.34}$$

53

Normalizing by $4\pi/\lambda$, we obtain the phase angle process

$$\psi_i(\omega, t) = \psi_i^0(\omega) + c_i(\omega, t)t \tag{7.35}$$

where $\psi_i^0(\omega)$ is a uniformly distributed random variable (over $(0, 2\pi)$). For nonmaneuvering motions, $c_i(\omega, t)$ is a slowly varying process whose density function is determined by the ship's motion. Because this motion is oscillatory, the density function of $V_i(\omega, t)$ will likely be symmetric with mean equal to zero. For short periods we approximate $V_i(\omega, t)$ by a random variable and the RCS process becomes

$$\sigma(t) = \sum_{i=1}^{N} \sum_{k=1}^{N} A_i(t)A_k(t) \, e^{j[\psi_i^0(\omega) - \psi_k^0(\omega) + (c_i - c_k)t]}. \tag{7.36}$$

The RCS which is generated by the target over the short periods are "pieces" of realizations of the RCS process. Because the radar must process only these pieces, we examine the "apparent variance" of them. For an interval of length T, the apparent mean of the phase process is

$$\eta_T = \frac{1}{T} \int_{-T/2}^{T/2} (\psi_i^0 + c_i t) \, dt = \psi_i^0 \tag{7.37a}$$

and the apparent variance is

$$\sigma_T^2 = \frac{1}{T} \int_{-T/2}^{T/2} (c_i t)^2 dt = \frac{c_i^2 T^2}{12}. \tag{7.37b}$$

Equation (7.37b) confirms that which is intuitively obvious: either or both c_i or T must be large for the uniformly distributed-phase approximation to be valid. If the standard deviation of ψ_i is required to be greater than $2n\pi$ for the approximation to hold, then over a time interval T_0 we require that

$$\frac{c_i^2 T_0^2}{12} \geqslant (2n\pi)^2 \tag{7.38a}$$

or

$$c_i \geqslant \frac{\sqrt{48}\,\pi}{T_0}\, n. \tag{7.38b}$$

Since $c_i = 4\pi V_i/\lambda$,

$$V_i \geqslant \frac{\sqrt{3}\,\lambda}{T_0}\, n \tag{7.39a}$$

and

$$n \leqslant \frac{T_0 V_i}{\sqrt{3}\,\lambda}. \tag{7.39b}$$

To illustrate the limitations of the uniformly distributed-phase model, consider a radar tracking the stern of our example ship at a low-grazing angle. To estimate the value of V_i we use

$$V_i \approx \frac{E\{\Delta T^2\}^{1/2}}{\tau} \tag{7.40}$$

where τ is the radar's PRI. In this scenario, pitching motion has the dominant effect on the variations in the scatterer ranges: from Appendix B,

$$E\{\Delta R^2\} \approx z_{max}^2 E\{\Delta \theta^2\}$$
$$= 2z_{max}^2 \sigma_\theta^2 [1 - e^{-\alpha_\theta |\tau|} \cos \omega_{0_\theta} \tau]. \tag{7.41}$$

For $\tau = 0.002$ s, $\omega_{0_\theta} - 0.409$ rad/s and $\sigma_\theta = 0.0089$ rad (Appendix A), and $z_{max} = 5$ m (Appendix B), $E\{\Delta R^2\}^{1/2} = 0.00127$ m and $V_i = 0.64$ m/s. If the pitch process, θ, is approximately Gaussian, then n must be no less than about 10. For a 3 cm radar, Eq. (7.39a) says that for the random-phase model to apply, V_i must be greater than 0.51 m for $T = 1$ s. We see that in our example this is only marginally true and that for lower frequency radars, it will not be true.

8. GLINT

The second (next to RCS) most common projection of the scattered field is glint (angle noise, angle scintillation). This parameter represents the apparent angular location of the target as seen by the radar. It is correlated with the target's RCS and is a function of the radar's frequency, polarization, and antenna pattern and of the target's shape, size, and composition. We make the same assumptions for glint that we made for RCS: the radar is horizontally polarized with fixed frequency and the target is a perfect conductor whose polarization effects are accounted for in the unit-scatterer amplitudes.

As described in Section 1, two concepts have been used to understand and analyze the phenomenon of glint: phase-front distortion and Poynting-vector direction. In the development of glint models based on these concepts, it was assumed that the target was composed of a finite number of point-source or dipole scatterers. Therefore, these models are directly applicable in our modeling approach. In this chapter we use both concepts to develop glint equations for a target described in terms of unit-scatterers.

Various authors have applied the glint concepts to specific problems, but to our knowledge no deterministic analytic-formulation of two-dimensional glint has been made for the N-source target in the presence of multipath. We develop this formulation for both concepts. The resulting equations will be analytically complex but ideal for digital simulation.

8.1 Definitions

Most existing models of glint represent the target and its motion in only one plane: the target is represented as a line in the azimuth plane of the radar. (This approximation is made because the longest dimension of most targets is in that plane.) Therefore, these glint models are one dimensional. We refer to such glint as azimuth glint. The less-often-used but more general glint models are two-dimensional. Because of our three-dimensional representation of the ship and of multipath effects, we will develop a two-dimensional glint model. The second glint dimension is elevation.

8.1.1 Phase-Front Gradient

The phase-front definition was introduced by Howard [12]. He showed that azimuth glint was equal to the azimuth slope of the phase front of the scattered field. Figure 8.1 illustrates this concept. For the one-dimensional problem, the phase front is a curve that passes through the location point of the radar. This curve is defined by mapping the locations of points where the phase of the scattered electric field is equal to the value of phase at the radar point. The analytical expression for azimuth glint is derived by expressing the phase of the scattered electric field, Φ, as a function of the angle about the sight-line from the radar to a fixed point on the target, ψ (see Fig. 8.1). Each scatterer is assumed to yield identically polarized plane waves at the radar. The azimuth glint then becomes, in linear units,

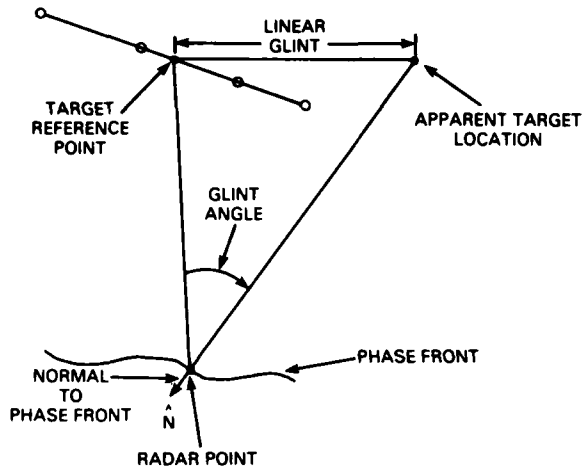$$G_a(\psi) = \frac{1}{k} \frac{d\Phi}{d\psi} \qquad (8.1)$$

Fig. 8.1 — Azimuth glint visualized in terms of phase front slope

where k is the wave number, $2\pi/\lambda$. It was shown by Howard [12] that for a target composed of N point scatterers on a line (Fig. 8.2), azimuth glint, in linear units, is

$$G_a(\psi) = -\sin\psi \cdot \frac{\sum_{i=1}^{N}\sum_{j=1}^{N} a_i a_j L_i \cos[2k(L_i - L_j)\cos\psi]}{\sum_{i=1}^{N}\sum_{j=1}^{N} a_i a_j \cos[2k(L_i - L_j)\cos\psi]} \qquad (8.2)$$

where L_i and ψ are defined in Fig. 8.2 and a_i is the amplitude of the ith scatterer. The minus sign arises because we define ψ in the opposite sense than that of Ref. 12.
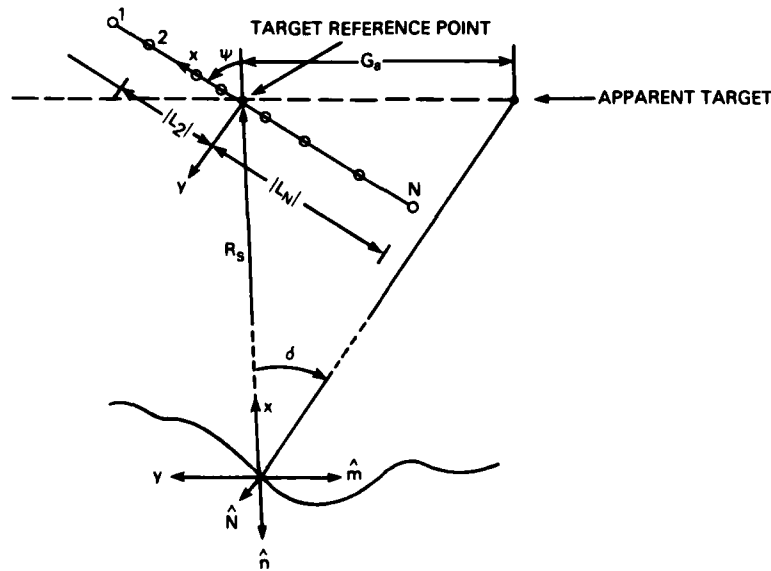

Fig. 8.2 — Parameters of the classical glint problem

The obvious extension of the phase-front-slope concept (Eq. (8.1)) is the phase-front gradient

$$\nabla \Phi = \left[\hat{n} \, \frac{\partial}{\partial r} + \frac{\hat{l}}{r} \, \frac{\partial}{\partial \theta} + \frac{\hat{m}}{r \sin \theta} \, \frac{\partial}{\partial \psi} \right] \Phi. \qquad (8.3)$$

From Eq. (8.3) and Fig. 8.2, we see that in linear units azimuth glint is

$$G_a = |\vec{R}_s| \, \frac{\nabla \Phi \cdot \hat{m}}{\nabla \Phi \cdot \hat{n}} = \frac{\partial \Phi / \partial \psi}{\sin \theta \, \partial \Phi / \partial r}. \qquad (8.4a)$$

Similarly, the elevation glint is, in linear units,

$$G_e = |\vec{R}_s| \, \frac{\nabla \Phi \cdot (-\hat{l})}{\nabla \Phi \cdot \hat{n}} = \frac{-\partial \Phi / \partial \theta}{\sin \theta \, \partial \Phi / \partial r}. \qquad (8.4b)$$

For $\theta = \pi/2$, these equations reduce to the one-dimensional problem.

8.1.2 Poynting-Vector Direction

The phase-front model indicated that the flow of energy was not necessarily radial at the radar. This led Dunn and Howard [43] to show that the Poynting vector from an N-source target was normal to the phase front. Therefore the Poynting vector concept was shown to be equivalent to the phase-front-slope concept in predicting glint. Assuming that the Poynting vector of the scattered field at the radar is

$$\vec{P} = \vec{P}_r + \vec{P}_\psi + \vec{P}_\theta = P_r \hat{n} + P_\psi \hat{m} + P_\theta \hat{l} \qquad (8.5)$$

where P_r, P_ψ, and P_θ are the radial, azimuth-tangential, and elevation-tangential components, we see from Fig. 8.3 that the azimuth glint, in linear units, is

$$G_a = |\vec{R}_s| \cdot \frac{P_\psi}{P_r}. \qquad (8.6a)$$

Similarly, elevation glint, in linear units, is

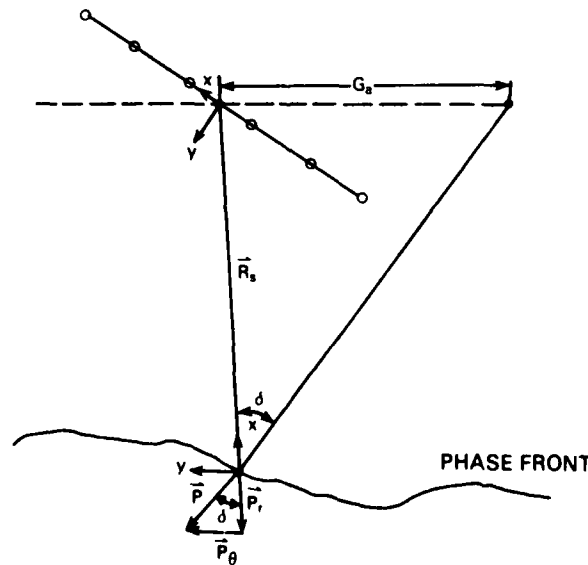$$G_e = |\vec{R}_s| \cdot \frac{P_\theta}{P_r}. \qquad (8.6b)$$

Fig. 8.3 — Azimuth glint visualized in terms of the Poynting vector

8.1.3 Axis Systems

To obtain equations that are useful for simulating the glint from an N-source target, we use $N +$ 2 axis-systems: an Earth-axis system, a target-cg-axis system, and N, US-location-axis systems. All of the axis systems are right-handed with the z-axis positive upward relative to Earth's surface:

> The origin of the Earth-axis system is at the radar point. This system is fixed relative to Earth with the $x - y$ plane defined as being parallel to Earth's surface. Subscripting a vector with the letter e implies that the vector is expressed in Earth coordinates. The unit vectors $\hat{i}$, $\hat{j}$, and $\hat{k}$ are the unit vectors of this system.

> The origin of the target-cg-axis system is fixed at the radar point. The x-axis is colinear with and directed along the sight line from the radar point to the target's cg. Subscripting a vector with the letter s implies that the vector is expressed in target-cg coordinates.

> The origins of the N US-location-axis systems are fixed at the radar point. The x-axes are co-linear with and directed along the sight lines from the radar point to the US locations. Subscripting a vector with an index implies that the vector is expressed in coordinates of the associated US-axis system.

Coordinates and vectors that locate points on the target relative to the radar point are indicated by subscripting with the letter R: location vectors are subscripted with a target-point indicator, location-vector coordinates are first subscripted with a coordinate indicator (x, y, or z) and then with a location-point indicator (index or s). Whenever the letter R is used as a vector coordinate, it is an Earth-system, rectangular coordinate.

For both the gradient and Poynting-vector approaches, the most natural formulation is in spherical coordinates. Figure 8.4 illustrates the spherical-system unit vectors that we use. We define the ith Poynting-vector plane (ith plane) as the plane passing through the radar point that is normal to the ith Poynting vector. The spherical unit vectors are defined relative to this plane:

$\hat{n}$ is perpendicular to the ith plane and positive away from the target,

$\hat{m}$ is the intersection of the ith plane and the $x - y$ plane of the Earth-axis system, and

$\hat{l}$ is in the ith plane such that $\hat{l} = \hat{m} \times \hat{n}$ and is positive downward.

From these definitions we see that $\hat{m}$ indicates the azimuth direction and $\hat{l}$ indicates the (negative) elevation direction. We note that $\hat{n}$ is also aligned with the target's Poynting vector and, equivalently, with the phase-front gradient.

8.2 Polarization Effects

The electric field polarization is an important parameter in determining glint but it has not been explicitly addressed in previous work. The one-dimensional glint problem has always been analyzed with the implicit assumption that the target elements radiate with the same polarization as the radar. This is a reasonable assumption in many practical problems. However, if this assumption is not valid, then current glint models can yield erroneous results. For example, consider the classic problem of a target composed of two scatterers (Fig. 8.2 with $N = 2$). If one of the scatterers' reradiation polarization is horizontal and the other's is vertical, then an ideal horizontally or vertically polarized radar will not sense one of the scatterers and there will be no nontrivial glint. The physical components of a US will often exhibit multiple scattering and such scattering causes cross polarization [53].
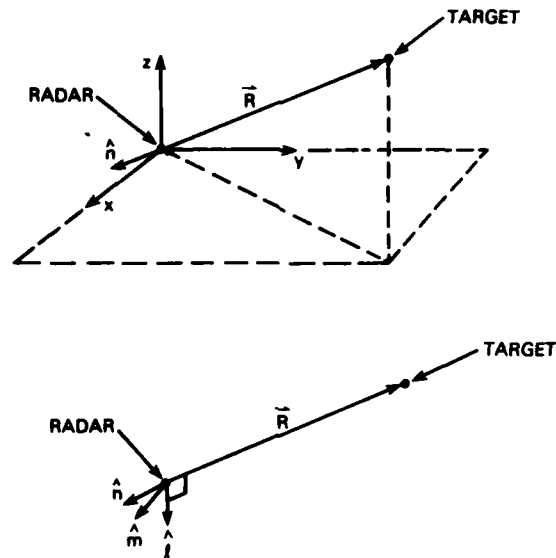
Fig. 8.4 — Spherical-coordinate unit vectors

Implicit in the glint concepts are different assumptions regarding the received-field polarizations. The gradient concept requires knowledge of the phase of the received field. This phase can be obtained accurately by assuming that the received fields from the USs are plane waves which are identically polarized. The Poynting-vector concept requires knowledge of the Poynting-vector direction and therefore only assumes that the received fields are planar; the received-field polarizations and directions of propagation must be accounted for in this method because they contain the directional information. For long ranges, the two methods produce results that are equivalent for practical purposes. However, we prefer the Poynting-vector method because it accounts for polarization effects, it is more closely related to physical concepts (power flow), and it does not require knowledge of rate-of-change properties of the US or multipath functions (Sec. 8.3).

8.3 Phase-Front Gradient

From Eq. (4.5), the magnitude of the received field has the form

$$E = g(\vec{R})\Gamma(\hat{p}_T, \hat{p}_R) = g(\vec{R})\hat{p}_T^T \left[\sum_{i=1}^{N} X_i\right]\hat{p}_R. \tag{8.7}$$

Equation (8.7) represents only that portion of the received field that is sensed by the radar. Assuming plane wave propagation, the vector representations of the fields sensed by the radar are simply

$$\vec{E} = E\hat{p}_R \tag{8.8a}$$

and

$$\vec{H} = -\frac{E}{\eta} \hat{p}_R^\perp \tag{8.8b}$$

where η ($= 377 \ \Omega$) is the characteristic impedance of free space and $\hat{p}_R^\perp$ is orthogonal to $\hat{p}_R$ such that when the received polarization is horizontal, in the target-cg axis-system $\hat{p} = \hat{m}$ and $\hat{p} = \hat{l}$. Given the large-range assumption, this formulation yields accurate estimates of the magnitude and phase of the received field.

59

We begin with the received-field representation of Eq. (8.7), where we assume, for simplicity, that $\hat{p}_T = \hat{p}_R = (1, 0)^T$. Expanding the field into real and imaginary parts, the phase is

$$\Phi = \tan^{-1} \left\{ \frac{\sum\limits_{i=1}^{N} A_i \sin \phi_i}{\sum\limits_{i=1}^{N} A_i \cos \phi_i} \right\} \tag{8.9}$$

where we have implicitly included multipath effects (in A_i and ϕ_i) for later use. Glint is referenced to the target-cg axis system. Therefore all derivatives must be calculated in that system. First,

$$\frac{\partial \Phi}{\partial \psi} = \frac{\left(\sum\limits_{i=1}^{N} A_i \cos \phi_i \right)^2}{\left(\sum\limits_{i=1}^{N} A_i \cos \phi_i \right)^2 + \left(\sum\limits_{i=1}^{N} A_i \sin \phi_i \right)^2} \frac{\partial}{\partial \psi} \left(\frac{\sum\limits_{i=1}^{N} A_i \sin \phi_i}{\sum\limits_{i=1}^{N} A_i \cos \phi_i} \right) \tag{8.10}$$

and

$$\frac{\partial}{\partial \psi} \left(\frac{\sum\limits_{i=1}^{N} A_i \sin \phi_i}{\sum\limits_{i=1}^{N} A_i \cos \phi_i} \right) = \frac{\left(\sum\limits_{i=1}^{N} A_i \cos \phi_i \right) \sum\limits_{i=1}^{N} \left(A_i \frac{\partial \phi_i}{\partial \psi} \cos \phi_i + \frac{\partial A_i}{\partial \psi} \sin \phi_i \right)}{\left(\sum\limits_{i=1}^{N} A_i \cos \phi_i \right)^2}$$

$$- \frac{\left(\sum\limits_{i=1}^{N} A_i \sin \phi_i \right) \sum\limits_{i=1}^{N} \left(-A_i \frac{\partial \phi_i}{\partial \psi} \sin \phi_i + \frac{\partial A_i}{\partial \psi} \cos \phi_i \right)}{\left(\sum\limits_{i=1}^{N} A_i \cos \phi_i \right)^2}$$

$$= \frac{\sum\limits_{i=1}^{N} \sum\limits_{j=1}^{N} A_i A_j \frac{\partial \phi_j}{\partial \psi} \cos (\phi_i - \phi_j) - \sum\limits_{i=1}^{N} \sum\limits_{j=1}^{N} A_i \frac{\partial A_i}{\partial \psi} \sin (\phi_i - \phi_j)}{\left(\sum\limits_{i=1}^{N} A_i \cos \phi_i \right)^2}. \tag{8.11}$$

Hence,

$$\frac{\partial \Phi}{\partial \psi} = \frac{\sum\limits_{i=1}^{N} \sum\limits_{j=1}^{N} \left[A_i A_j \frac{\partial \phi_i}{\partial \psi} \cos (\phi_i - \phi_j) - A_i \frac{\partial A_i}{\partial \psi} \sin (\phi_i - \phi_j) \right]}{\sum\limits_{i=1}^{N} \sum\limits_{j=1}^{N} A_i A_j \cos (\phi_i - \phi_j)}. \tag{8.12}$$

Similarly,

$$\frac{\partial \Phi}{\partial \theta} = \frac{\sum\limits_{i=1}^{N} \sum\limits_{j=1}^{N} \left[A_i A_j \frac{\partial \phi_j}{\partial \theta} \cos (\phi_i - \phi_j) - A_i \frac{\partial A_j}{\partial \theta} \sin (\phi_i - \phi_j) \right]}{\sum\limits_{i=1}^{N} \sum\limits_{j=1}^{N} A_i A_j \cos (\phi_i - \phi_j)} \tag{8.13}$$

and

$$\frac{\partial \Phi}{\partial r} = \frac{\sum_{i=1}^{N} \sum_{j=1}^{N} \left[A_i A_j \frac{\partial \phi_j}{\partial r} \cos\,(\phi_i - \phi_j) - A_i \frac{\partial A_j}{\partial r} \sin\,(\phi_i - \phi_j) \right]}{\sum_{i=1}^{N} \sum_{j=1}^{N} A_i A_j \cos\,(\phi_i - \phi_j)}. \tag{8.14}$$

The a_i functions $(A_i = |F_i^2|\, a_i)$ depend on US orientation, not on range. Therefore $\partial a_i/\partial r = 0$ for all i and

$$\frac{\partial \Phi}{\partial r} = \frac{\sum_{i=1}^{N} \sum_{j=1}^{N} A_i A_j \frac{\partial \phi_j}{\partial r} \cos\,(\phi_i - \phi_j) - \sum_{i=1}^{N} \sum_{j=1}^{N} 2a_j A_i \frac{\partial |F_i|}{\partial r} \sin\,(\phi_i - \phi_j)}{\sum_{i=1}^{N} \sum_{j=1}^{N} A_i A_j \cos\,(\phi_i - \phi_j)}. \tag{8.15}$$

The resulting glint equations are

$$G_a = \frac{\sum_{i=1}^{N} \sum_{j=1}^{N} \left[A_i A_j \frac{\partial \phi_j}{\partial \psi} \cos\,(\phi_i - \phi_j) - A_i \frac{\partial A_j}{\partial \psi} \sin\,(\phi_i - \phi_j) \right]}{\sum_{i=1}^{N} \sum_{j=1}^{N} \left[A_i A_j \frac{\partial \phi_j}{\partial r} \cos\,(\phi_i - \phi_j) - a_j A_i \frac{\partial |F_j^2|}{\partial r} \sin\,(\phi_i - \phi_j) \right]} \tag{8.16a}$$

and

$$G_e = \frac{\sum_{i=1}^{N} \sum_{j=1}^{N} \left[A_i A_j \frac{\partial \phi_j}{\partial \theta} \cos\,(\phi_i - \phi_j) - A_i \frac{\partial A_j}{\partial \theta} \sin\,(\phi_i - \phi_j) \right]}{\sum_{i=1}^{N} \sum_{j=1}^{N} \left[A_i A_j \frac{\partial \phi_j}{\partial r} \cos\,(\phi_i - \phi_j) - a_j A_i \frac{\partial |F_j^2|}{\partial r} \sin\,(\phi_i - \phi_j) \right]}. \tag{8.16b}$$

We recall that

$$\phi_i(\vec{R}_i, \vec{\theta}_i) = 2k|\vec{R}_i| + \gamma(\vec{R}_i, \vec{\theta}_i) + \beta_i(\vec{\theta}_i) \tag{8.17}$$

where $\gamma(\vec{R}_i, \vec{\theta}_i)$ is the phase due to multipath and $\beta_i(\theta_i)$ is the phase due to US orientation. Clearly, specific knowledge of the US functions is required to use the glint equations in the form of Eqs. (8.16). In particular, the derivatives of the US and multipath coefficient amplitudes and phases (with respect to azimuth and elevation) are required.

For the classic problem of N sources on a rigid rod (Fig. 8.2), various assumptions are made: ranges are large, the scatterer amplitudes and phases are constant with respect to rotations, and there is no multipath. These assumptions yield

$$\frac{\partial \phi_i}{\partial \psi} = 2k\,\frac{\partial |\vec{R}_i|}{\partial \psi}, \tag{8.18a}$$

$$\frac{\partial \phi_i}{\partial \theta} = 2k\,\frac{\partial |\vec{R}_i|}{\partial \theta}, \tag{8.18b}$$

$$\frac{\partial \phi_i}{\partial r} \approx 2k, \tag{8.18c}$$

$$|F_i| = 1, \tag{8.18d}$$

and

$$\frac{\partial A_j}{\partial \psi} = \frac{\partial A_j}{\partial \theta} = \frac{\partial |F_j|}{\partial r} = 0. \tag{8.18e}$$

61

D.Y. NORTHAM

So that

$$G_a \approx \frac{\sum_{i=1}^{N} \sum_{j=1}^{N} a_i a_j \frac{\partial |\vec{R}_i|}{\partial \psi} \cos (\phi_i - \phi_j)}{\sum_{i=1}^{N} \sum_{j=1}^{N} a_i a_j \cos (\phi_i - \phi_j)}. \tag{8.19}$$

We see from Fig. 8.2 that the large-range assumption implies that

$$\phi_i - \phi_j \approx 2k(L_i - L_j) \cos \psi \tag{8.20a}$$

and

$$|\vec{R}_j| \approx R_s + L_j \cos \psi \tag{8.20b}$$

so that

$$\frac{\partial |\vec{R}_j|}{\partial \psi} \approx -L_j \sin \psi \tag{8.21}$$

where the L_j are the signed distances of the scatterers from the target reference point. (We note that Howard [12] incorrectly uses the unsigned distances in his Eq. (5).) Using Eqs. (8.20a), (8.20b), and (8.21) in Eq. (8.16a) we obtain the well-known Eq. (8.2).

8.4 Poynting-Vector Direction

Dunn and Howard [43] showed that glint was equivalent to the direction of the time-average Poynting vector. The time averaging is performed over the period T, where $\omega = 2\pi/T$ is the radar's frequency. The averaging is valid because the phase terms of the received field (Eq. (8.7)) are approximately constant over the period T. The time-average Poynting vector is defined by

$$\vec{P} = \frac{1}{2} \vec{E} \times \vec{H}^*. \tag{8.22}$$

For an N-source target and no multipath,

$$\vec{E} = \left[g(\vec{R}) \hat{p}_T^T \left(\sum_{i=1}^{N} X(\vec{R}_i, \vec{\theta}_i) \right) \hat{p}_R \right] \hat{p}_R. \tag{8.23}$$

Given that the polarization of both the transmitter and the receiver are horizontal, in the target-cg axis-system the electric field and the Poynting vector can be represented in the forms

$$\vec{E} = g(\vec{R}) \left(\sum_{i=1}^{N} a_i e^{j\phi_i} \right) \hat{m}_s \tag{8.24a}$$

and

$$\vec{P} = \frac{g^2(\vec{R})}{2\eta} \left[\sum_{i=1}^{N} \sum_{k=1}^{N} a_i a_k \cos (\phi_i - \phi_k) \right] \hat{n}_s \tag{8.24b}$$

where the a_i and ϕ_i terms are obtained by taking into account the associated US-radar geometries. (Note that the $\hat{p}_T$ and $\hat{p}_R$ vectors must be expressed in each of the individual US axis-systems.) Equation (8.24b) is not in a useful form because $\hat{n}_s$ is not known directly. Therefore, we next derive an equation for $\vec{P}$ in terms of the N, known Poynting vectors.

Equations for the locations of the USs were derived in Sections 5 and 6; given the radar point and the US locations, the Poynting vector for each US can be determined. The total fields due to the USs are

$$\vec{E} = g(\vec{R}) \sum_{i=1}^{N} a_i e^{j\phi_i} \hat{m}_i \tag{8.25a}$$

62

and

$$\vec{H} = -\frac{g(\vec{R})}{\eta} \sum_{i=1}^{N} a_i e^{j\phi_i} \hat{l}_i, \tag{8.25b}$$

and the associated Poynting vector is

$$\vec{P} = -\frac{g^2(\vec{R})}{2\eta} \sum_{i=1}^{N} \sum_{k=1}^{N} a_i a_k \cos(\phi_i - \phi_k) \hat{m}_i \times \hat{l}_k. \tag{8.26}$$

We define the position of the ith scatterer relative to the radar (in Earth coordinates) as

$$\vec{R}_i = R_{x_i}\hat{i} + R_{y_i}\hat{j} + R_{z_i}\hat{k} \tag{8.27}$$

where for clarity, the $\vec{R}_i$ time-dependence is suppressed. In the ith US-system

$$\hat{n}_i = -\frac{1}{|\vec{R}_i|}(R_{x_i}\hat{i} + R_{y_i}\hat{j} + R_{z_i}\hat{k}). \tag{8.28a}$$

Because $\hat{m}_i$ is in the x-y plane of the Earth-axis system and is perpendicular to $\vec{R}_i$,

$$\hat{m}_i = \sin\psi_i\hat{i} - \cos\psi_i\hat{j} \tag{8.28b}$$

where $\psi_i = \tan^{-1}(R_{y_i}/R_{x_i})$ and $\vec{R}_{x_{y_i}} = R_{x_i}\hat{i} + R_{y_i}\hat{j}$ (Fig. 8.5). Finally,

$$\hat{l}_i = \hat{m}_i \times \hat{n}_i = \frac{R_{z_i}}{|\vec{R}_i|}\cos\psi_i\hat{i} + \frac{R_{z_i}}{|\vec{R}_i|}\sin\psi_i\hat{j} - \left[\frac{R_{y_i}\sin\psi_i}{|\vec{R}_i|} + \frac{R_{x_i}\cos\psi_i}{|\vec{R}_i|}\right]\hat{k}. \tag{8.28c}$$
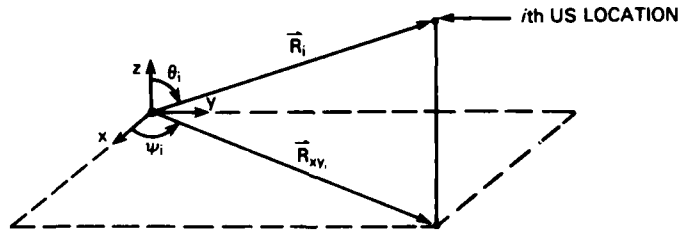

Fig. 8.5 — The ith azimuth and elevation angles
in the Earth-axis system

By using Eqs. (8.28), the cross product term of Eq. (8.26) is

$$\hat{m}_i \times \hat{l}_k = \hat{m}_i \times (\hat{m}_k \times \hat{n}_k). \tag{8.29a}$$

Expanding Eq. (8.29a) in terms of known quantities,

$$\hat{m}_i \times \hat{l}_k = \frac{R_{y_k}\sin\psi_k + R_{x_k}\cos\psi_k}{|\vec{R}_k|}\cos\psi_i\hat{i}$$

$$+ \frac{R_{y_k}\sin\psi_k + R_{x_k}\cos\psi_k}{|\vec{R}_k|}\sin\psi_i\hat{j} + \frac{R_{z_k}}{|\vec{R}_k|}\cos(\psi_k - \psi_i)\hat{k}. \tag{8.29b}$$

Equations (8.28) express the ith-system unit vectors in (rectangular) Earth coordinates. Referring to Fig. 8.5 we see that the transformation from Earth coordinates to target-cg coordinates, T_{ET}, is

$$T_{ET} = \frac{1}{|\vec{R}_s|^2}\begin{bmatrix} R_{z_s}\cos\psi_s & R_{z_s}\sin\psi_s & -R_{y_s}\sin\psi_s - R_{x_s}\cos\psi_s \\ \sin\psi_s & -\cos\psi_s & 0 \\ R_{x_s} & R_{y_s} & R_{z_s} \end{bmatrix} \tag{8.30}$$

63

where the subscript s indicates the target's cg location and $\psi_s = \tan^{-1}(R_{y_s}/R_{x_s})$. The Poynting vector is now

$$\vec{P} = -\frac{g^2(\vec{R})}{2\eta}\left[\sum_{i=1}^{N}\sum_{k=1}^{N} a_i a_k \cos(\phi_i - \phi_k) T_{ET}(\hat{m}_i \times \hat{l}_k)_e\right] \qquad (8.31a)$$

$$= -\frac{g^2(\vec{R})}{2\eta} T_{ET}\left[\sum_{i=1}^{N}\sum_{k=1}^{N} a_i a_k \cos(\phi_i - \phi_k)(\hat{m}_i \times \hat{l}_k)_e\right] \qquad (8.31b)$$

where the $(\hat{m}_i \times \hat{l}_k)$ vector is expressed in Earth coordinates. The azimuth and elevation glint can now be expressed as

$$G_a = |\vec{R}_s| \frac{\left[\sum_{i=1}^{N}\sum_{k=1}^{N} a_i a_k \cos(\phi_i - \phi_k) T_{ET}(\hat{m}_i \times \hat{l}_k)_e\right] \cdot \hat{m}_s}{\left[\sum_{i=1}^{N}\sum_{k=1}^{N} a_i a_k \cos(\phi_i - \phi_k) T_{ET}(\hat{m}_i \times \hat{l}_k)_e\right] \cdot \hat{n}_s} \qquad (8.32a)$$

$$G_e = |\vec{R}_s| \frac{\left[\sum_{i=1}^{N}\sum_{k=1}^{N} a_i a_k \cos(\phi_i - \phi_k) T_{ET}(\hat{m}_i \times \hat{l}_k)_e\right] \cdot [-\hat{l}_s]}{\left[\sum_{i=1}^{N}\sum_{k=1}^{N} a_i a_k \cos(\phi_i - \phi_k) T_{ET}(\hat{m}_i \times \hat{l}_k)_e\right] \cdot \hat{n}_s}. \qquad (8.32b)$$

We note that for small US-separations and long ranges, $\hat{m}_i \times \hat{l}_k \approx \hat{n}_s$, so that the denominator of Eqs. (8.32) is approximately the target's RCS (Eq. (7.7a)).

8.5 Multipath Effects

For low-grazing-angle illumination of ships, over-water multipath affects the received signal. In Section 4, we described a multipath model appropriate for point-source scatterers. In this section, we discuss the modeling of the effects of multipath on glint.

A different method of multipath modeling is required for each glint concept because they are developed under different assumptions. The phase-front gradient method requires explicit knowledge of only the received amplitudes and phases whereas the Poynting-vector method also requires explicit direction-of-propagation information.

8.5.1 Phase-Front Gradient

For the phase-front gradient model, we view multipath as an alteration of the received amplitude and phase from the US. Referring to Eq. (4.17), we rewrite Eq. (8.9) to explicitly show the multipath effects:

$$\Phi = \tan^{-1}\left[\frac{\sum_{i=1}^{N} |F_i^2| a_i \sin\phi_i}{\sum_{i=1}^{N} |F_i^2| a_i \cos\phi_i}\right] \qquad (8.33)$$

where ϕ_i is defined by Eq. (8.17). From Eqs. (8.16) we see that the terms of interest are the partial derivatives of $|F_i^2|a_i$ and ϕ_i with respect to r, ψ, and θ (in the target-cg axis system). Because there are in general no physical interpretations for these rate-of-change processes, they would, at best, be difficult to estimate. They are also analytically complex so we will develop the general multipath formulation only for the Poynting-vector method, which yields physically-meaningful results. However, we will analyze the special case of very calm (smooth) seas.

From Eqs. (4.16) we see that the ith multipath factor is

$$F_i = (1 + \rho_{s_i} \cos \alpha_i + \rho_{p_i}) + j(\rho_{s_i} \sin \alpha_i + \rho_{Q_i}). \tag{8.34}$$

For smooth seas, $\rho_{p_i} = 0$ and $\rho_{Q_i} = 0$ (their variances become zero) and we have

$$F_i = (1 + \cos \alpha_i) + j \sin \alpha_i \tag{8.35}$$

where

$$|F_i| = [(1 + \cos \alpha_i)^2 + \sin^2 \alpha_i]^{1/2}$$
$$= (2 + 2 \cos \alpha_i)^{1/2} \tag{8.36}$$

and

$$\gamma_i = \tan^{-1} \left[\frac{\sin \alpha_i}{1 + \cos \alpha_i} \right]. \tag{8.37}$$

The partial derivatives with respect to a parameter p are

$$\frac{\partial |F_i^2|}{\partial p} = -2 \cos \alpha_i \frac{\partial \alpha_i}{\partial p} \tag{8.38a}$$

and

$$\frac{\partial \gamma_i}{\partial p} = \frac{(1 + \cos \alpha_i)}{(1 + \cos \alpha_i)^2 + \sin^2 \alpha_i} \cdot \frac{\partial}{\partial p} \left[\frac{\sin \alpha_i}{1 + \cos \alpha_i} \right]$$

$$= \frac{\partial \alpha_i}{\partial p} \left[\frac{(1 + \cos \alpha_i) \cos \alpha_i + \sin^2 \alpha_i}{(1 + \cos \alpha_i)^2 + \sin^2 \alpha_i} \right]$$

$$= \frac{1}{2} \frac{\partial \alpha_i}{\partial p}. \tag{8.38b}$$

Clearly, $\partial \alpha_i / \partial p$ is the significant parameter. We use the well-known approximation for path-length difference

$$\Delta R_i \approx \frac{2 h_R h_i}{|\vec{R}_{xy_i}|} \tag{8.39}$$

for the difference between the direct and reflected path lengths so that

$$\alpha_i = \frac{2 k h_R h_i}{|\vec{R}_{xy_i}|}. \tag{8.40}$$

Because ψ is the azimuth angle,

$$\frac{\partial \alpha_i}{\partial \psi} = 0. \tag{8.41}$$

The coordinate r is the radial distance so that

$$\frac{\partial \alpha_i}{\partial r} \approx -\frac{2 k h_R h_i}{|\vec{R}_{xy_i}|^2}. \tag{8.42}$$

Finally, θ_i is an elevation angle and (see Fig. 8.6)

$$\cos \theta_i = \frac{R_{z_i}}{|\vec{R}_i|} \approx \frac{R_{z_i}}{|\vec{R}_{xy_i}|} \tag{8.43}$$

65

where, from Fig. 8.6, $R_{z_i} = h_i - h_R$. Now

$$\alpha_i \approx 2kh_R \left[\frac{R_{z_i} + h_R}{|\vec{R}_i|} \right]$$

$$\approx 2kh_R \left[\frac{h_R}{|\vec{R}_i|} + \cos \theta_i \right] \tag{8.44}$$

so that

$$\frac{\partial \alpha_i}{\partial \theta} \approx 2kh_R \left[-\frac{h_R}{|\vec{R}_i|^2} \frac{\partial |\vec{R}_i|}{\partial \theta} - \sin \theta_i \frac{\partial \theta_i}{\partial \theta} \right]. \tag{8.45}$$

Because $\sin \theta_i \approx 1$, $\partial \theta_i / \partial \theta \approx 1$, $h_R / |\vec{R}_i| \ll 1$, and $\partial |\vec{R}_i| / \partial \theta \ll |\vec{R}_i|$, we have that for a smooth sea-surface,

$$\frac{\partial \alpha_i}{\partial \theta} \approx -2kh_R. \tag{8.46}$$

Hence, the multipath components of the phase-front-gradient formulation are

$$\frac{\partial |F_i^2|}{\partial \psi} = 0, \tag{8.47a}$$

$$\frac{\partial \gamma_i}{\partial \psi} = 0, \tag{8.47b}$$

$$\frac{\partial |F_i^2|}{\partial r} \approx \frac{4kh_R h_i}{|\vec{R}_{xy_i}|^2} \cos \left[\frac{2kh_R h_i}{|\vec{R}_{xy_i}|} \right], \tag{8.47c}$$

$$\frac{\partial \gamma_i}{\partial r} \approx -\frac{kh_R h_i}{|\vec{R}_{xy_i}|^2}, \tag{8.47d}$$

$$\frac{\partial |F_i^2|}{\partial \theta} \approx 4kh_R \cos \left[\frac{2kh_R h_i}{|\vec{R}_{xy_i}|} \right], \tag{8.47e}$$

and

$$\frac{\partial \gamma_i}{\partial \theta} \approx -kh_R. \tag{8.47f}$$

8.5.2 Poynting-Vector Direction

To introduce multipath into the Poynting-vector formulation, we modify the received fields by the multipath factor, F_i^2, described in Sec. 4.4 (Eqs. (4.18)). This factor modifies the direct-return scattered fields and induces N apparent (image) scatterers. This model allows the obvious extension of Eq. (8.31b) to

$$\vec{P} = -\frac{g^2(\vec{R})}{2\eta} T_{ET} \left[\sum_{i=1}^{2N} \sum_{k=1}^{2N} M_i M_k a_i a_k \cos (\phi_i - \phi_k)(\hat{m}_i \times \hat{l}_k)_e \right] \tag{8.48}$$

where

$$M_i = \begin{cases} F_i & , \quad 1 \leqslant i \leqslant N \\ F_{i-N}(F_{i-N} - 1) & , \quad N + 1 \leqslant i \leqslant 2N, \end{cases} \qquad (8.49a)$$

$$\left.\begin{aligned} a_l &= a_m \\ \phi_l &= \phi_m \\ \hat{m}_l &= \hat{m}_m \end{aligned}\right\} \quad l \leqslant N, \quad m = l + N, \qquad (8.49b)$$

and, from Fig. 8.6,

$$\vec{R}_i = \vec{R}_i' = R_{x_i}\hat{i} + R_{y_i}\hat{j} - (h_R + h_i)\hat{k}, \quad N + 1 \leqslant i \leqslant 2N. \qquad (8.49c)$$
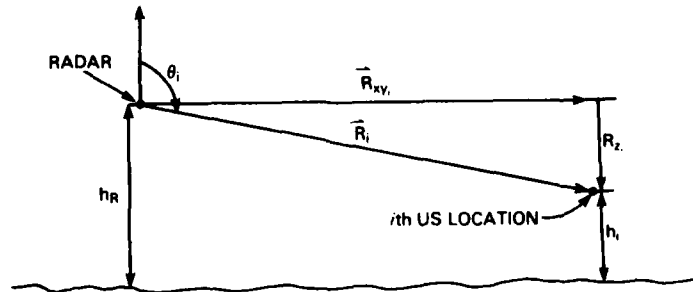

Fig. 8.6 — Multipath geometry

Equation (8.49c) implies that Eq. (8.28c) becomes

$$\hat{l}_i = \frac{R_{z_i}'}{|\vec{R}_i'|} \cos \psi_i \hat{i} + \frac{R_{z_i}'}{|\vec{R}_{z_i}|} \sin \psi_i \hat{j} - \left[\frac{R_{y_i} \sin \psi_i + R_{x_i} \cos \psi_i}{|\vec{R}_i'|} \right] \hat{k} \qquad (8.49d)$$

for $N + 1 \leqslant i \leqslant 2N$. Therefore when accounting for multipath, the glint equations become

$$G_a = |\vec{R}_s| \frac{\left[\sum_{i=1}^{2N} \sum_{k=1}^{2N} M_i M_k a_i a_k \cos (\phi_i - \phi_k) T_{ET} (\hat{m}_i \times \hat{l}_k)_e \right] \cdot \hat{m}_s}{\left[\sum_{i=1}^{2N} \sum_{k=1}^{2N} M_i M_k a_i a_k \cos (\phi_i - \phi_k) T_{ET} (\hat{m}_i \times \hat{l}_k)_e \right] \cdot \hat{n}_s} \qquad (8.50a)$$

and

$$G_e = |\vec{R}_s| \frac{\left[\sum_{i=1}^{2N} \sum_{k=1}^{2N} M_i M_k a_i a_k \cos (\phi_i - \phi_k) T_{ET} (\hat{m}_i \times \hat{l}_k)_e \right] \cdot [-\hat{l}_s]}{\left[\sum_{i=1}^{2N} \sum_{k=1}^{2N} M_i M_k a_i a_k \cos (\phi_i - \phi_k) T_{ET} (\hat{m}_i \times \hat{l}_k)_e \right] \cdot \hat{n}_s}. \qquad (8.50b)$$

As in Eqs. (8.32), for small US-separations and long ranges the denominator of Eqs. (8.50) approximates the target's RCS.

It is clear that Eqs. (8.50) are more natural and accurate for use in modeling the glint of N-source targets than are Eqs. (8.16). Equations (8.50) are used in the simulations (Appendix C).

9. SIMULATION RESULTS

In this section we briefly summarize the results of simulations that were performed by using the method of Section 6 to simulate US motion and the equations of Sections 7 and 8 (as modified, for efficiency, in Appendix C) to simulate RCS and glint. The source code that was used is presented in Appendix D. Because of the number of parameters affecting the scattering process, a parametric study of the model was beyond the scope of this report. Among those parameters are:

> ship structure
> ship maneuvering
> ship speed
> ship response to the sea (RAOs)
> sea state
> sea structure (sea, swell, etc.)
> ship heading relative to the dominant wave direction
> radar-to-ship aspect angle
> radar-to-ship elevation angle
> radar frequency
> radar pulsewidth
> relative motion between the radar and the ship
> US amplitudes
> US phases
> US locations.

We note that when measurements of ship scattering (e.g., RCS or glint) are made, measurements of the first twelve parameters listed should also be made.

In the simulation studies, we have investigated the qualitative effects of variations in ship maneuvering, radar-to-ship aspect angle, and multipath (which is primarily a function of radar-to-ship elevation angle, radar frequency, and sea state).

9.1 Simulation Parameters

In the simulations, the radar's wavelength was 3 cm and the radar was located at a fixed point that was 40 m above the sea surface. The ship's position was initialized at 10 km from the radar. This yields grazing angles on the order of 0.25°.

Two maneuvers were considered for the ship: straight-line motion and turning. For the straight-line motion the ship's speed was 10 kn, and for the turning motion the turn rate was 0.4°/s and the ship's speed was 6 kn. The maneuvers were simulated with and without multipath effects. For the straight-line motion an rms wave height of 0.762 m was used because this corresponds to the sea state associated with the ship-motion spectra that were used (Appendix A). For the turning maneuver an rms wave height of 0.135 m was used and the ship-motion spectra were changed from the spectra of Appendix A by reducing the rms values by a factor of 10 for each of the six motion processes; this was done to approximate the ship's motion in slight to moderate seas. For the geometry of the simulations the sea-roughness factor (a fundamental parameter characterizing multipath, defined by $h\sin\psi/\lambda$ where h is the rms wave height, ψ is the grazing angle, and λ is the radar's wavelength; see Ref. 49) is on the order of 0.025 for the turning motion and 0.133 for the straight-line motion. The simulation time-increment was 0.002 s, and the simulated time was 2.1 s.

The USs used in the simulation were chosen based on visual identification of scatterer type and approximate projected area. For $\lambda = 0.03$ m the sphere-like (constant RCS) scatterers have amplitudes that are small relative to the flat-plate and corner-reflector types, assuming comparable projected areas.

Therefore only flat-plate and corner-reflector types were used in the simulations because such scatterers dominated the ship's structure. A ship was chosen for which photographs were available and the USs were chosen for three aspect angles: broadside, aft-quarter, and stern. Table 9.1 lists the location, magnitude, and type (flat-plate is type 2 and corner-reflector is type 3) for the USs that were used. Figure 9.1 is intended as an aid in visualizing the ship representation: it contains two-dimensional plots of the US locations relative to the ship's cg using the location data from Table 9.1.

9.2 Discussion

The output of each simulation run is presented as a figure composed of four plots: RCS, azimuth glint, and elevation glint as functions of time, and azimuth glint vs elevation glint for each time instant (connecting the points from instant to instant). RCS is plotted in dB above one square meter (dBsm), and all RCS plots use the same scale. The scales for the glint plots vary (due to the nature of glint). These plots are Figs. 9.2 to 9.15.

Figures 9.4 through 9.15 display the output of twelve simulations. The parameters varied in these simulations were maneuvering (straight-line, turn); aspect (broadside, aft-quarter, stern); and multipath (yes, no). Although the parameter variations are limited, the outputs indicate the qualitative effects of the parameters on RCS and glint. In the remainder of this section we discuss some of the most salient features of the output data.

9.3 Multipath Effects

Figures 9.2 and 9.3 illustrate the effects of (point-source) multipath for the two multipath conditions chosen. In each case the only motion is that of the sea surface; the ship scatterers do not move. We note the following implications of the sea-roughness factor: the rms waveheight of 0.762 m implies that diffuse-component multipath effects (random) dominate those due to the specular component and the rms waveheight of 0.135 m implies that the specular effects (deterministic) dominate. We also note that the diffuse multipath effects are essentially independent (except through variations in the value of the roughness factor) of ship motion for our scenarios, but the specular multipath effects, which are deterministic, are of course correlated with that motion. Clearly, both specular and diffuse multipath modulate the scattered fields further complicating the problem of US identification in the presence of multipath.

9.4 RCS

It is clear that the correlation properties of the RCS are strongly dependent on aspect angle. We see this in Figs. 9.4(a) through 9.15(a) and it is quantified by the normalized spectra shown in Figs. 9.16 through 9.18. (These spectra were calculated using the TSAP program, which is described in Ref. 96. A time series of 1024 points, 2.048 s, was used. First the autocovariance function was calculated using a 12.5% lag. This result was windowed and then an FFT was used to obtain the spectral estimates.)

Examining the quartering-aspect RCS in Fig. 9.5(b) we see that as shown in Chapter 7, even assuming constant amplitude functions (Table 9.1(b)) the slow, oscillatory motions of the ship can yield RCS realizations that appear nonstationary over short time-intervals. (Note that there is an apparent decreasing trend in the variance of that data.)

9.5 Glint

From the data we see that glint is a process with a wider bandwidth than the RCS process. Figure 9.19 contains examples of glint spectra (calculated by using the procedure described in Sec. 9.3) for data (from Figs. 9.5 and 9.8) that exhibit no obvious nonstationary characteristics in the mean or variance.

Table 9.1 — Scatterers That Were Used to
Model the Three Aspects

(a) Broadside

Location (WRT CG)			RCS am.	Scatt. Type	Plate Diam.
X	Y	Z			
−50.0	−4.0	2.0	4.0	3	
−5.0	−4.0	7.0		2	5.0
3.0	0.0	20.0	3.0	3	
10.0	−4.0	7.0		2	5.0
20.0	−4.0	7.0		2	3.0
30.0	−3.0	15.0	5.0	3	

(b) Aft-Quarter

Location (WRT CG)			RCS amp.	Scatt. Type	Plate Diam.
X	Y	Z			
−50.0	−2.0	3.0	3.0	3	
0.0	−2.0	7.0	6.0	3	
3.0	0.0	20.0	3.0	3	
14.0	−3.0	7.0	5.0	3	
17.0	0.0	20.0	4.0	3	
30.0	0.0	7.0	3.0	3	

(c) Stern

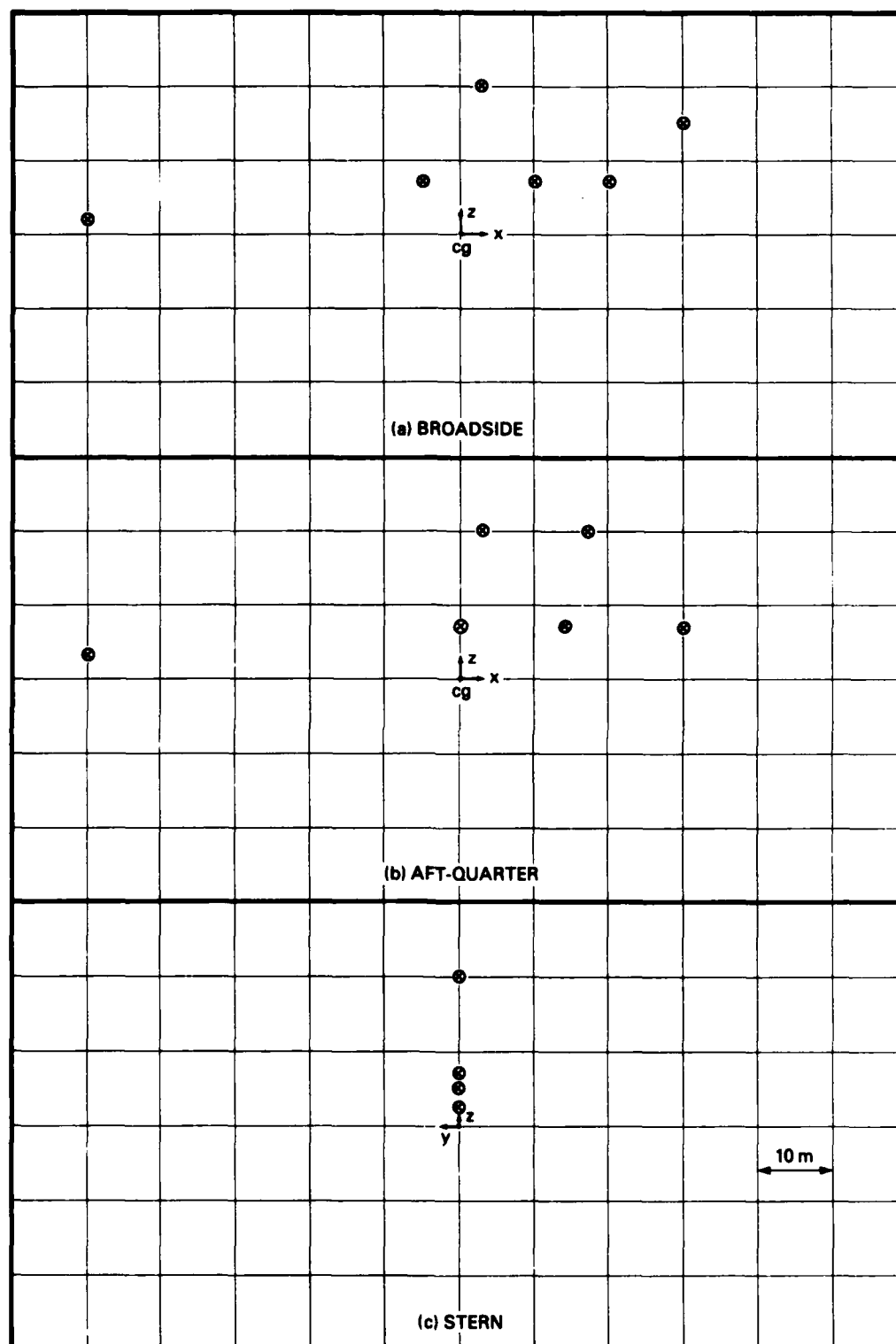| Location (WRT CG)			RCS amp.	Scatt. Type	Plate Diam.
X	Y	Z			
−60.0	0.0	0.0		2	6.0
−50.0	0.0	2.0	4.0	3	
−40.0	0.0	5.0	4.0	3	
−25.0	0.0	7.0		2	10.0
3.0	0.0	20.0	3.0	3	

Fig. 9.1 — Two-dimensional schematics of the *US* locations for each aspect
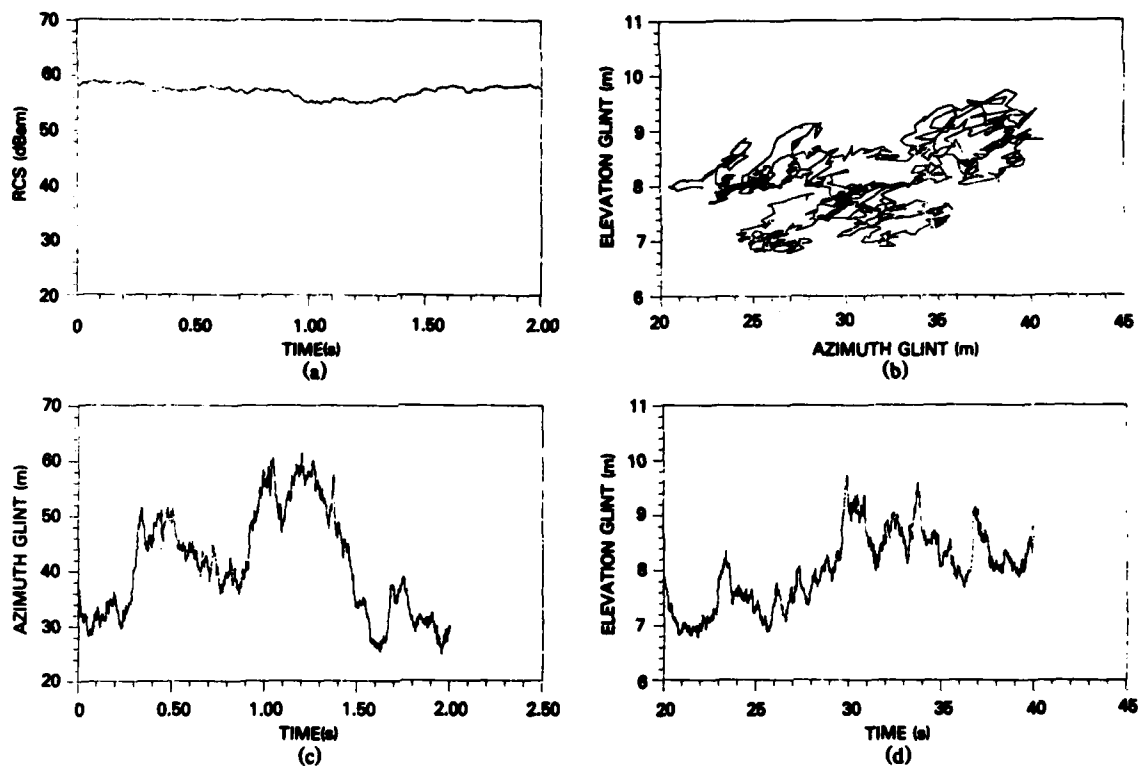(drawn to relative scale)

Fig. 9.2 — No ship motion, broadside aspect, rms wave height = 0.135 m
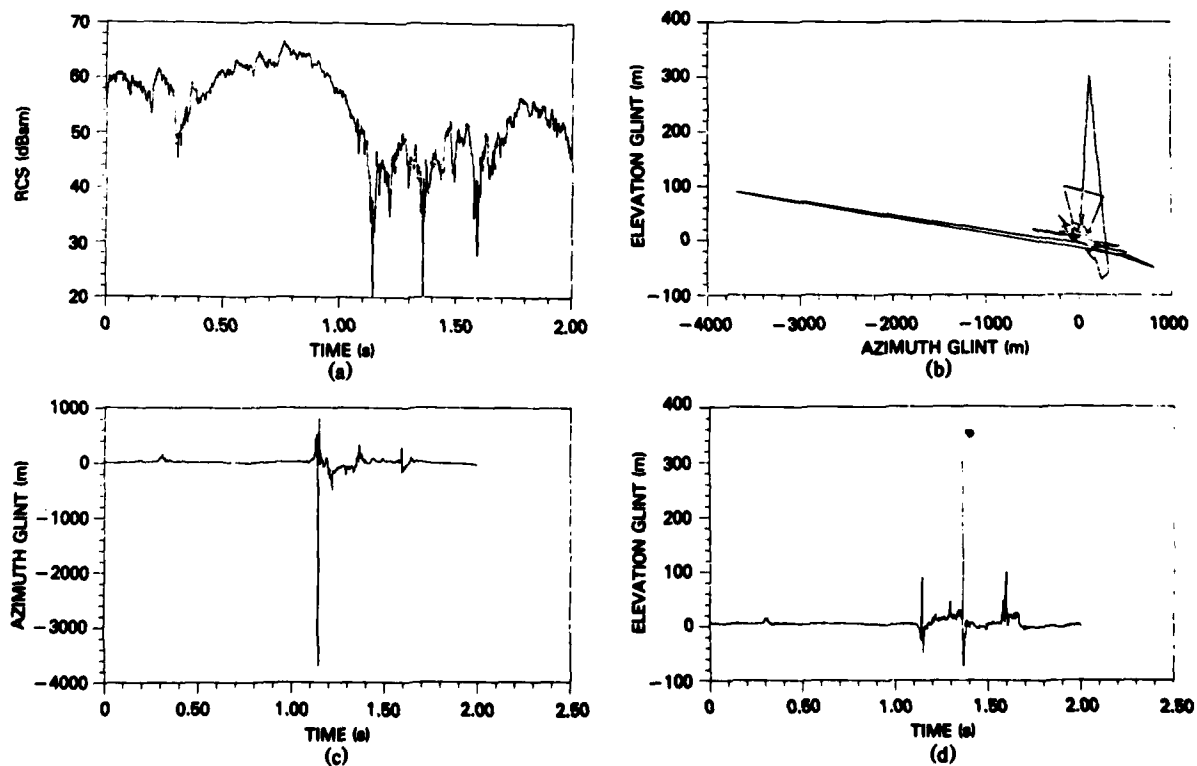

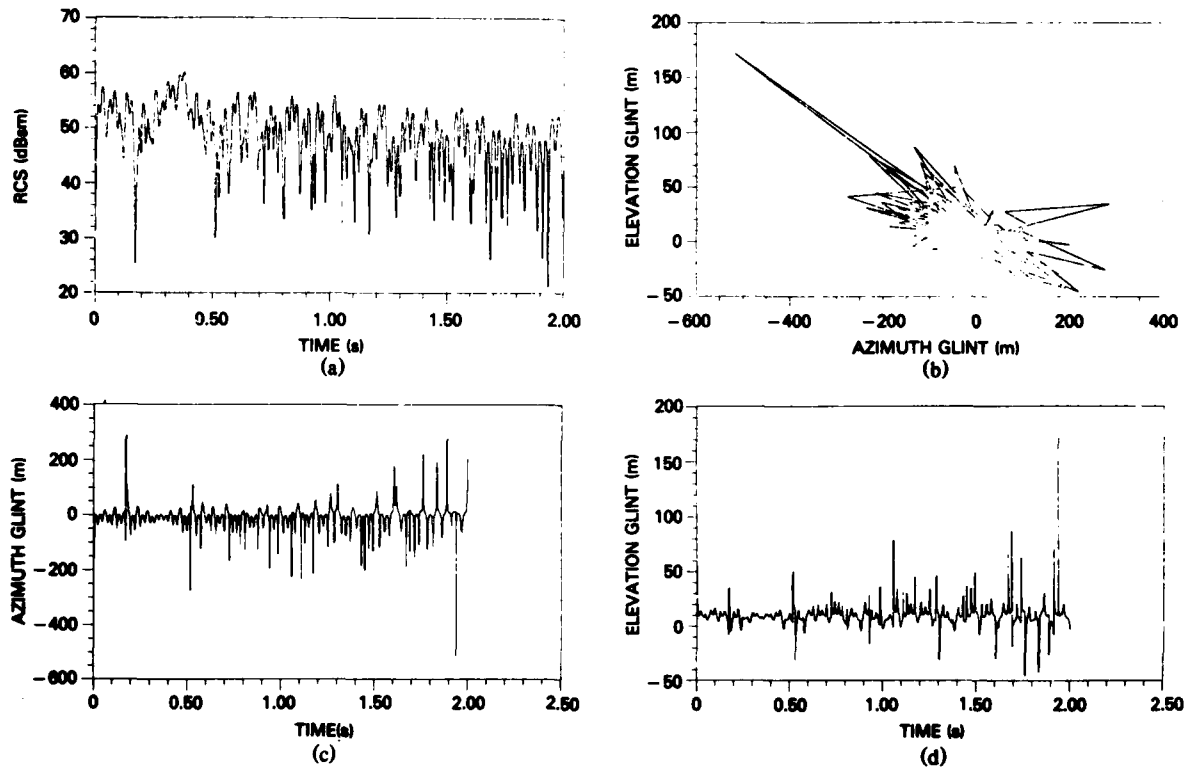Fig. 9.3 — No ship motion, broadside aspect, rms wave height = 0.762 m

Fig. 9.4 — Straight-line motion, ship speed = 10 kn, broadside aspect, no multipath
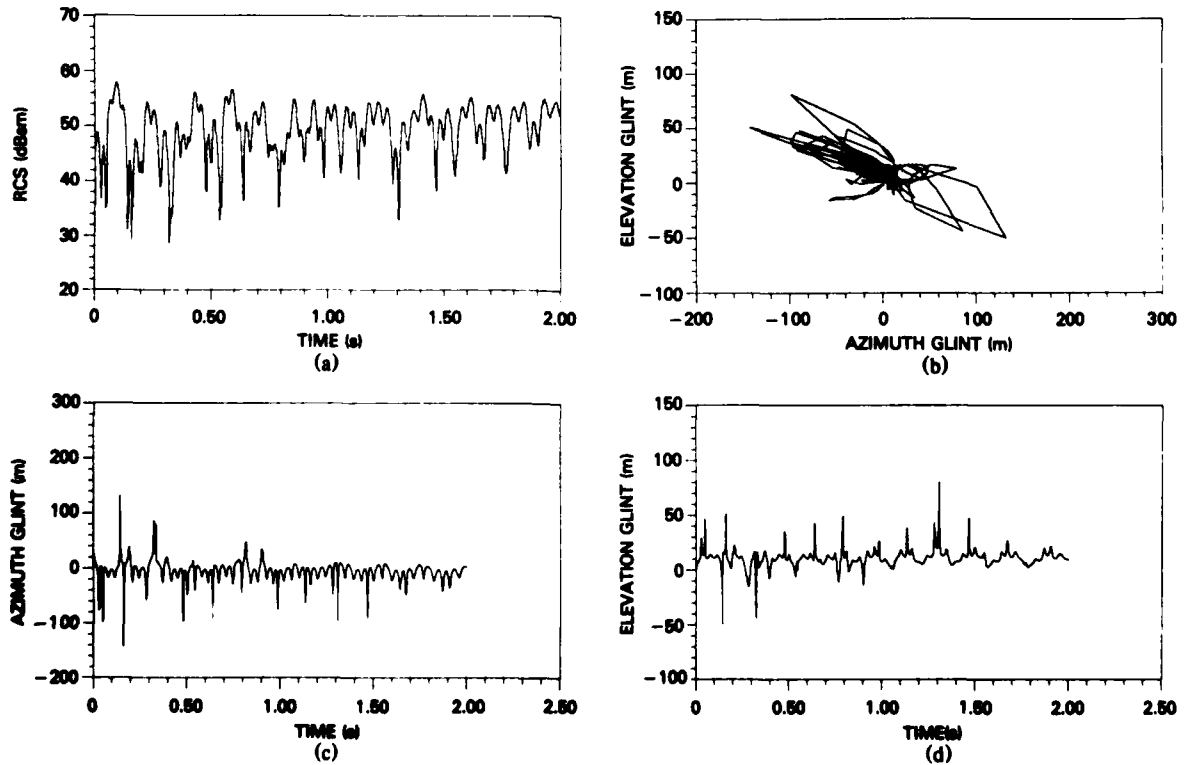

Fig. 9.5 — Straight-line motion, ship speed = 10 kn, aft-quarter aspect, no multipath
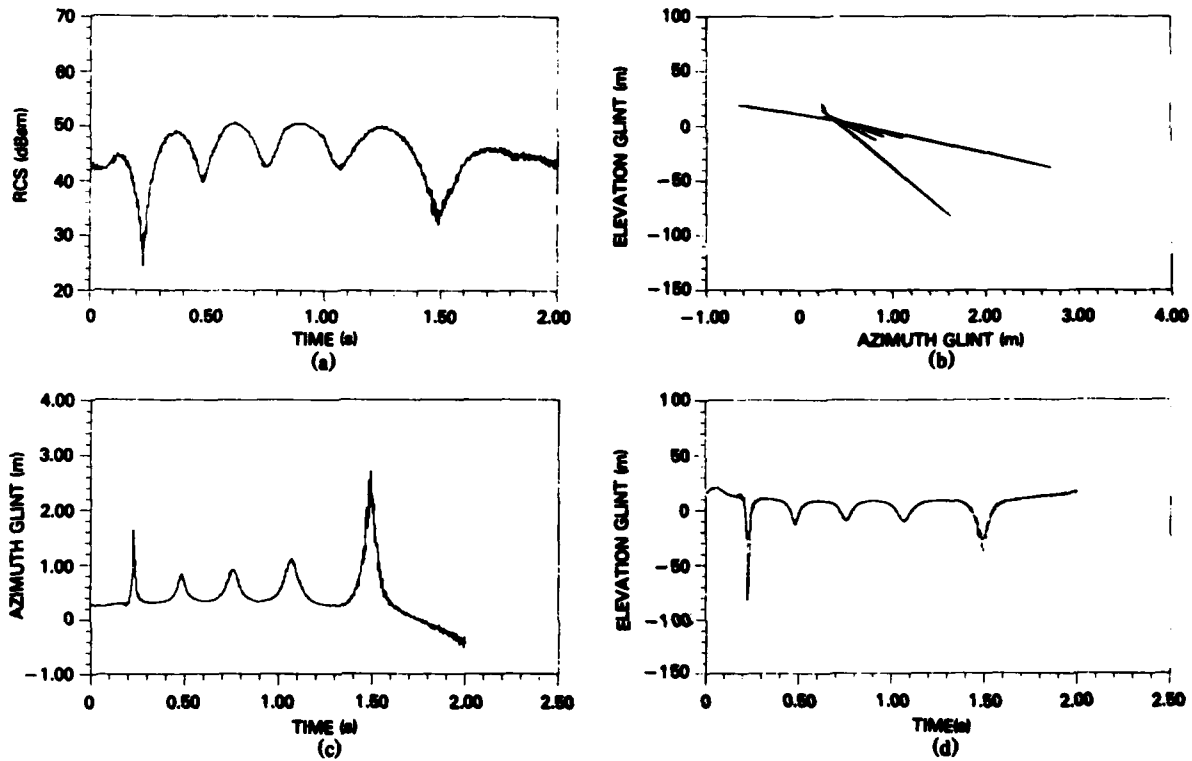
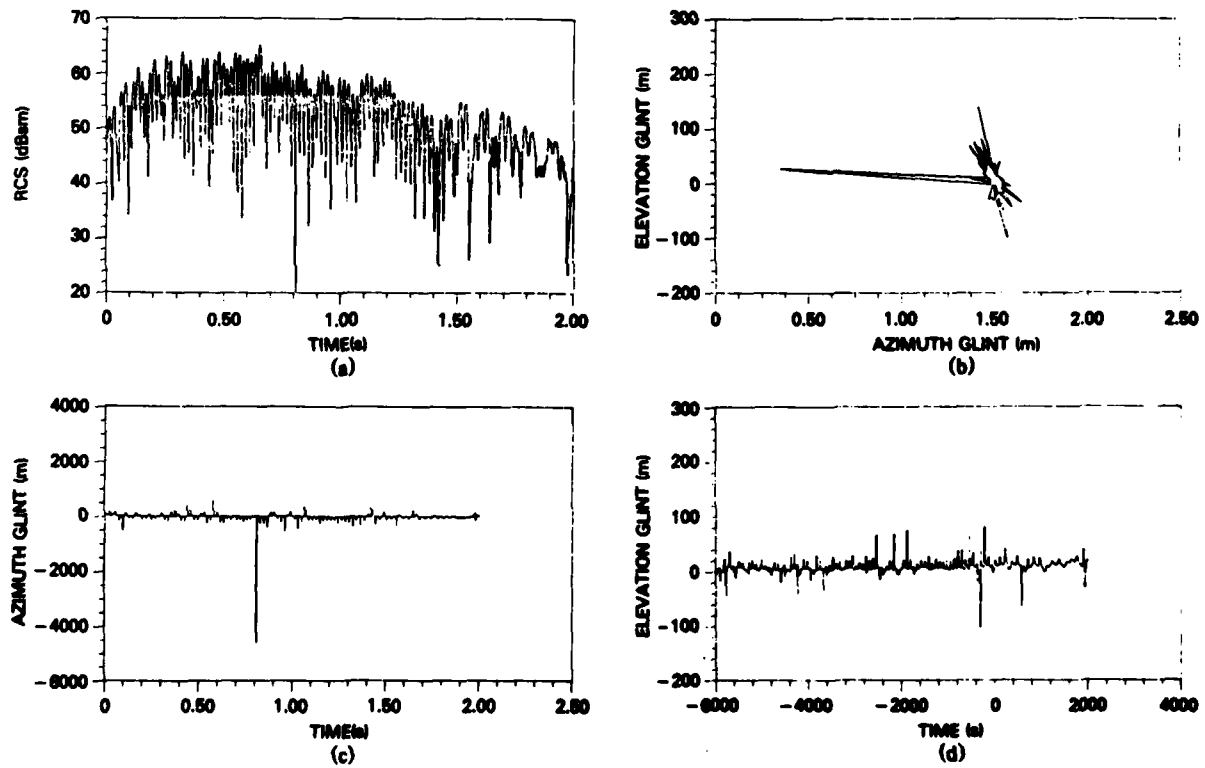Fig. 9.6 — Straight-line motion, ship speed = 10 kn, stern aspect, no multipath

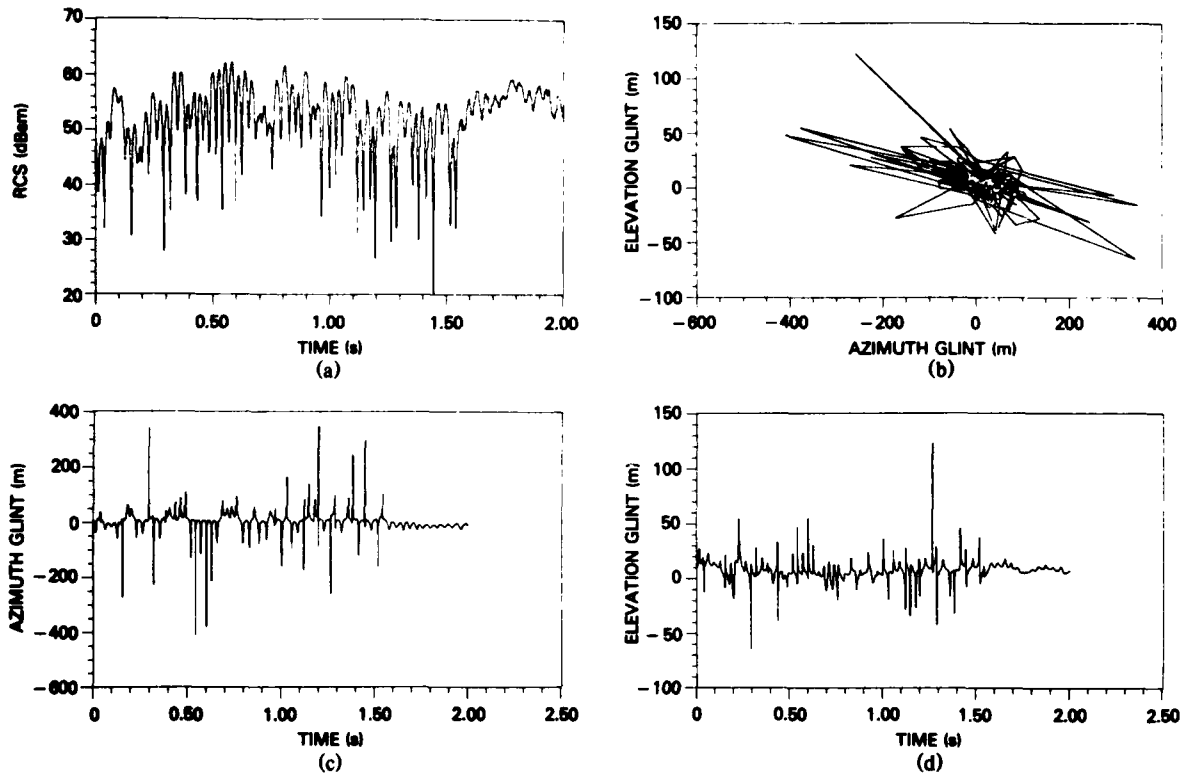Fig. 9.7 — Straight-line motion, ship speed = 10 kn, broadside aspect, rms wave height = 0.762 m

Fig. 9.8 — Straight-line motion, ship speed = 10 kn, aft-quarter aspect, rms wave height = 0.762 m
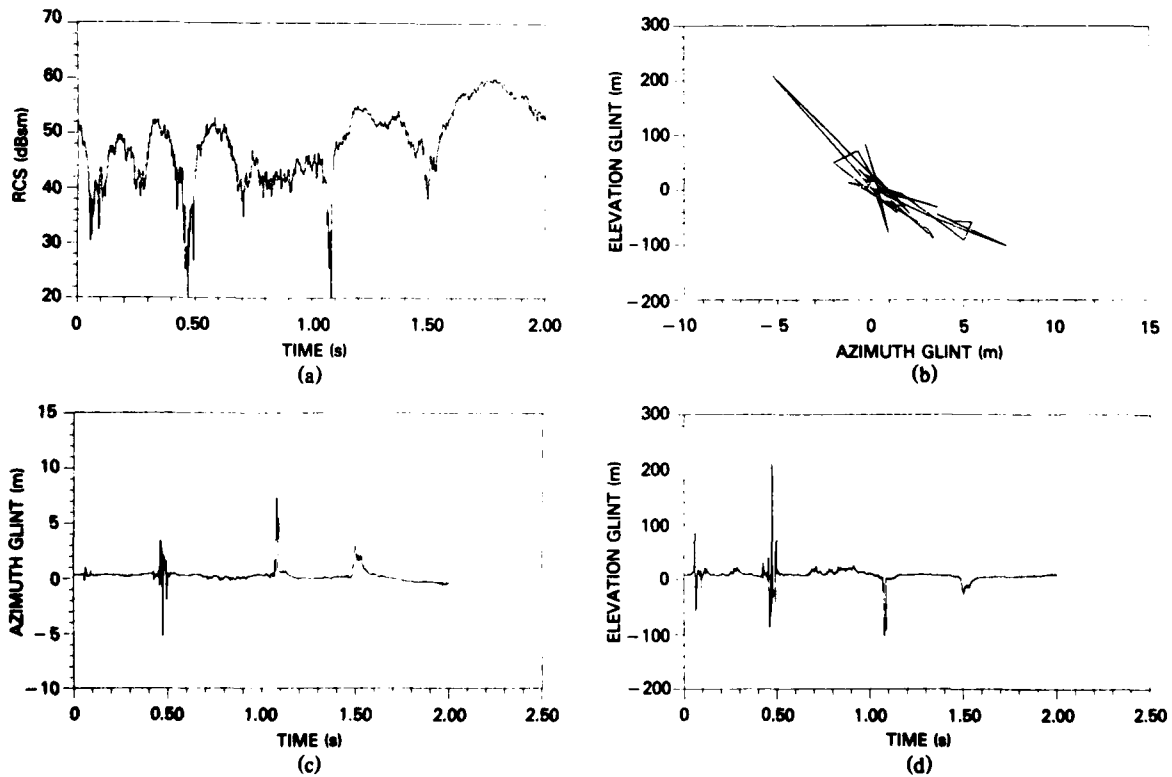
Fig. 9.9 — Straight-line motion, ship speed = 10 kn, stern aspect, rms wave height = 0.762 m
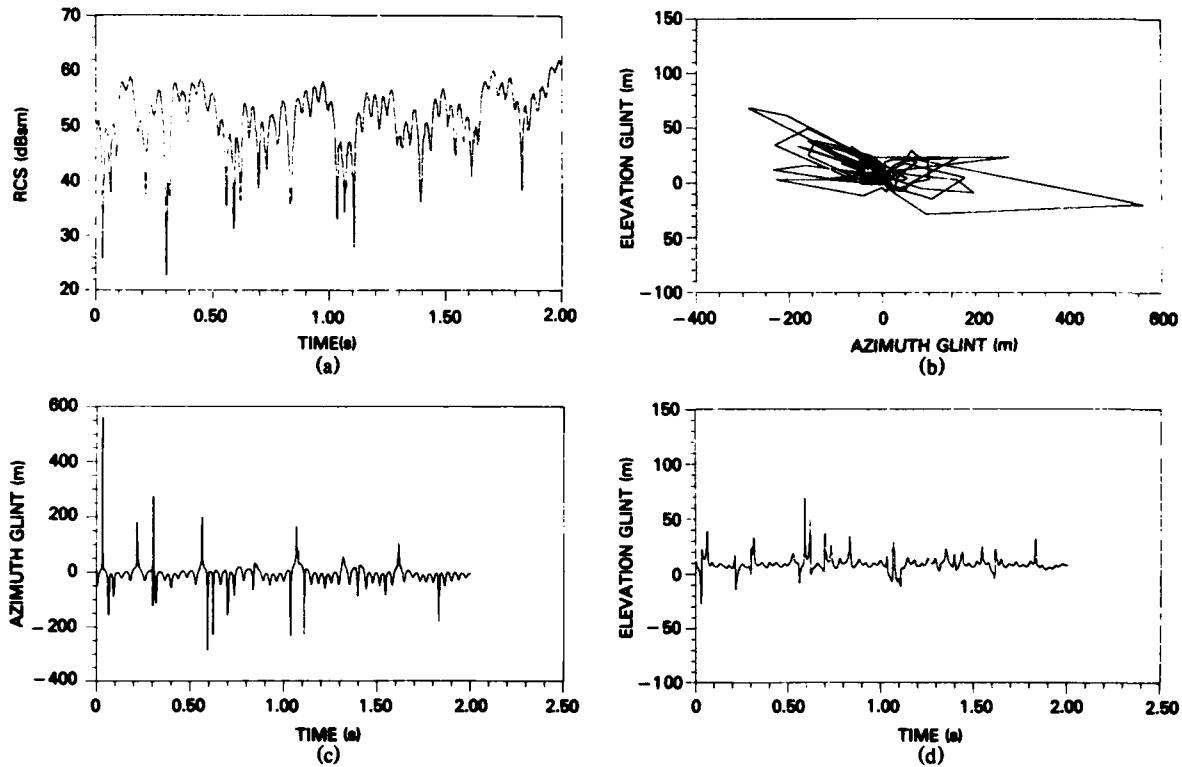
Fig. 9.10 — Ship turn rate = 0.4°/s, broadside aspect, no multipath
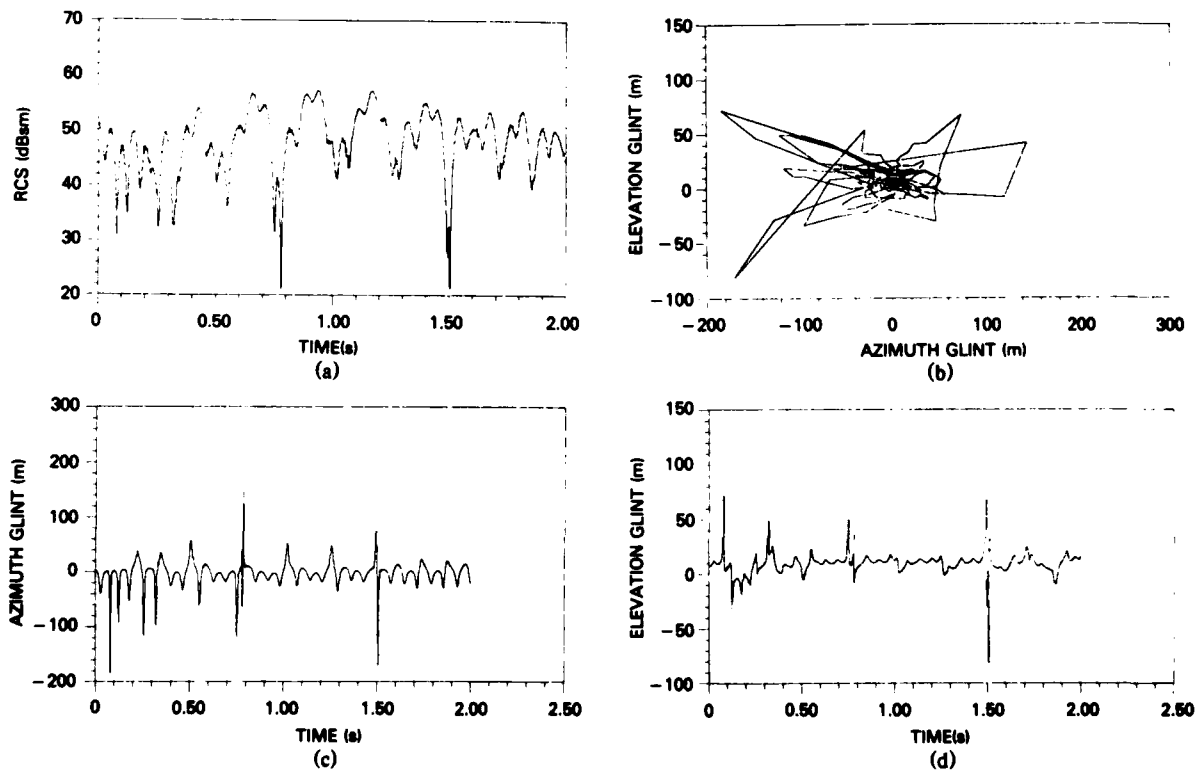
Fig. 9.11 — Ship turn rate = 0.4°/s, aft-quarter aspect, no multipath

76
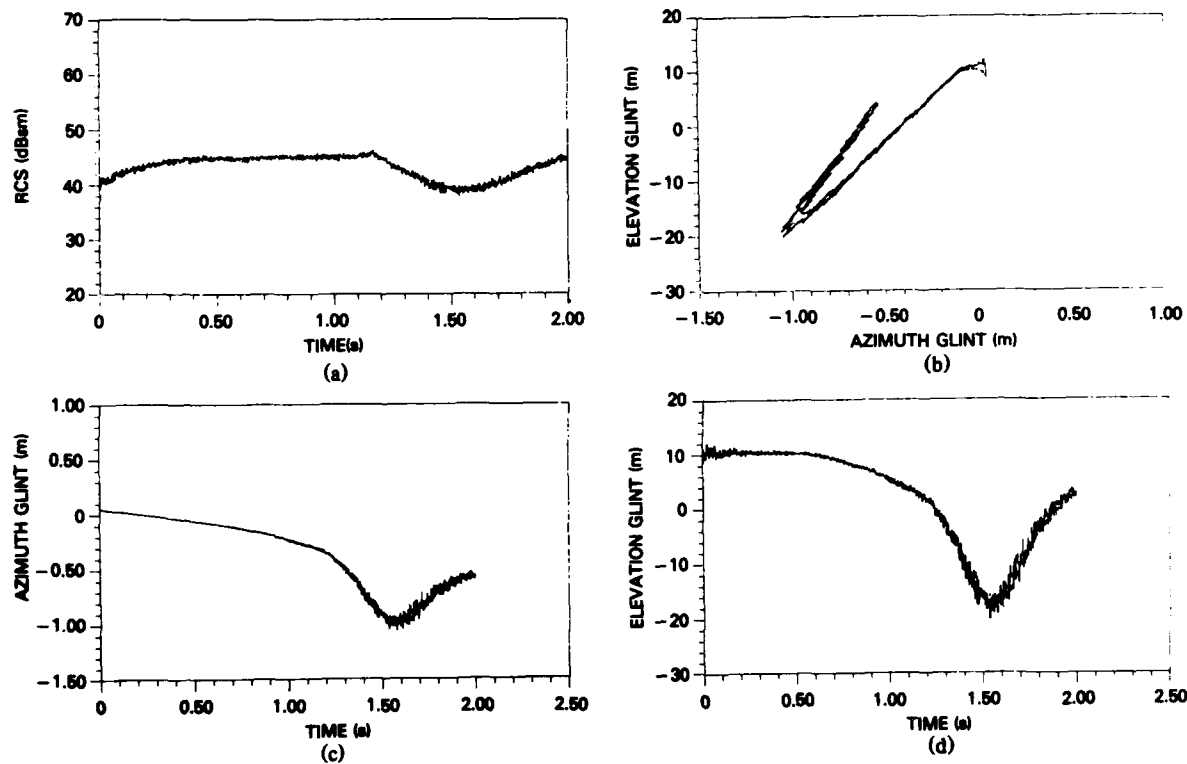
Fig. 9.12 — Ship turn rate = 0.4°/s, stern aspect, no multipath
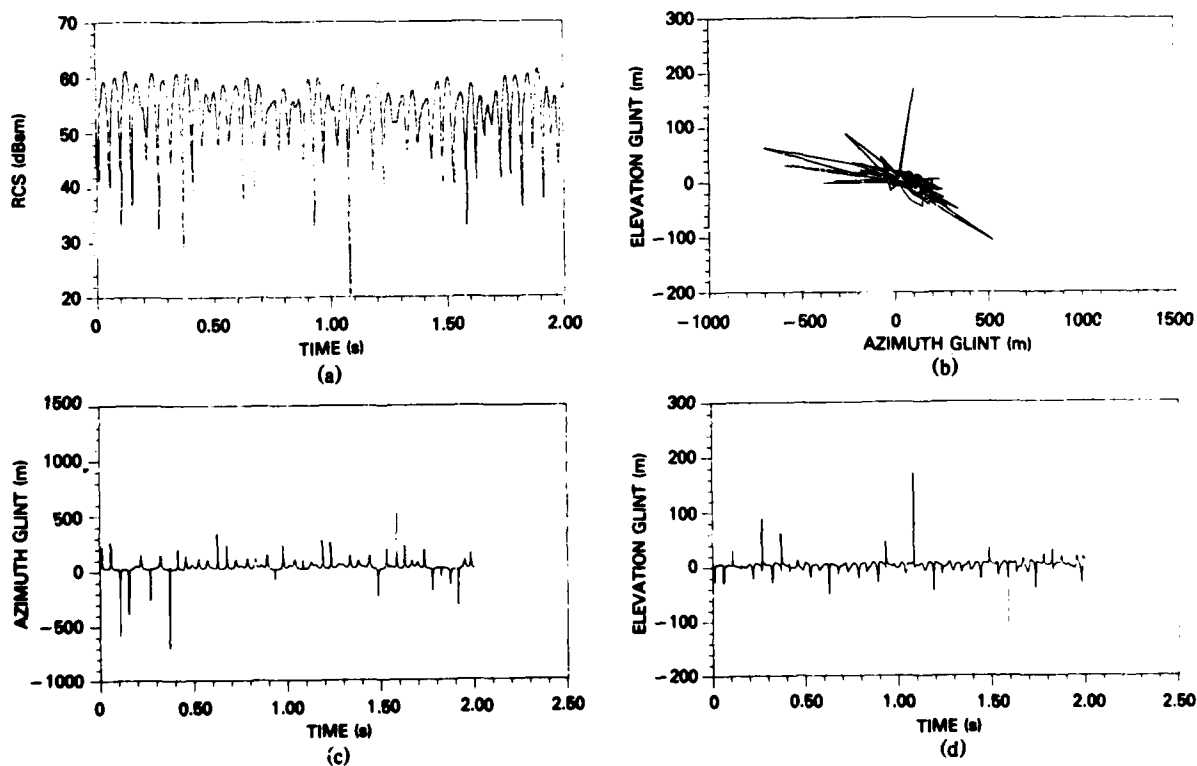
Fig. 9.13 — Ship turn rate = 0.4°/s, broadside aspect, rms wave height = 0.135 m
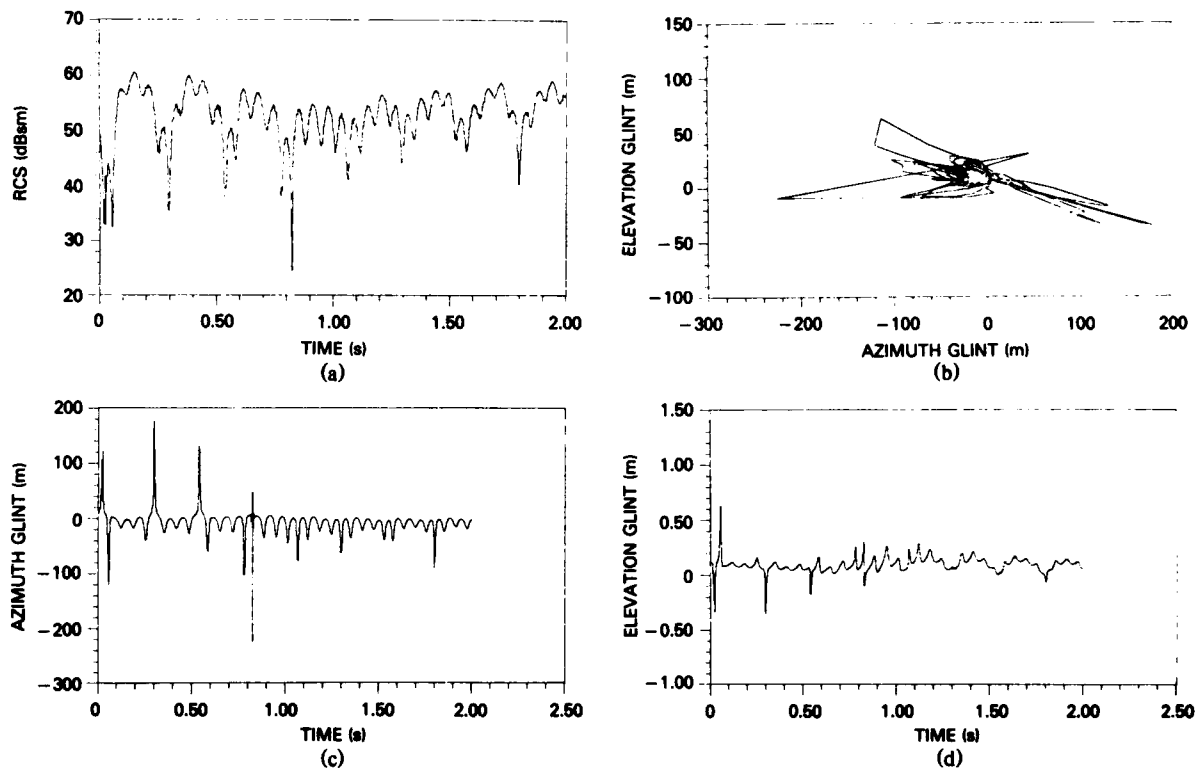
Fig. 9.14 — Ship turn rate = 0.4°/s, aft-quarter aspect, rms wave height = 0.135 m
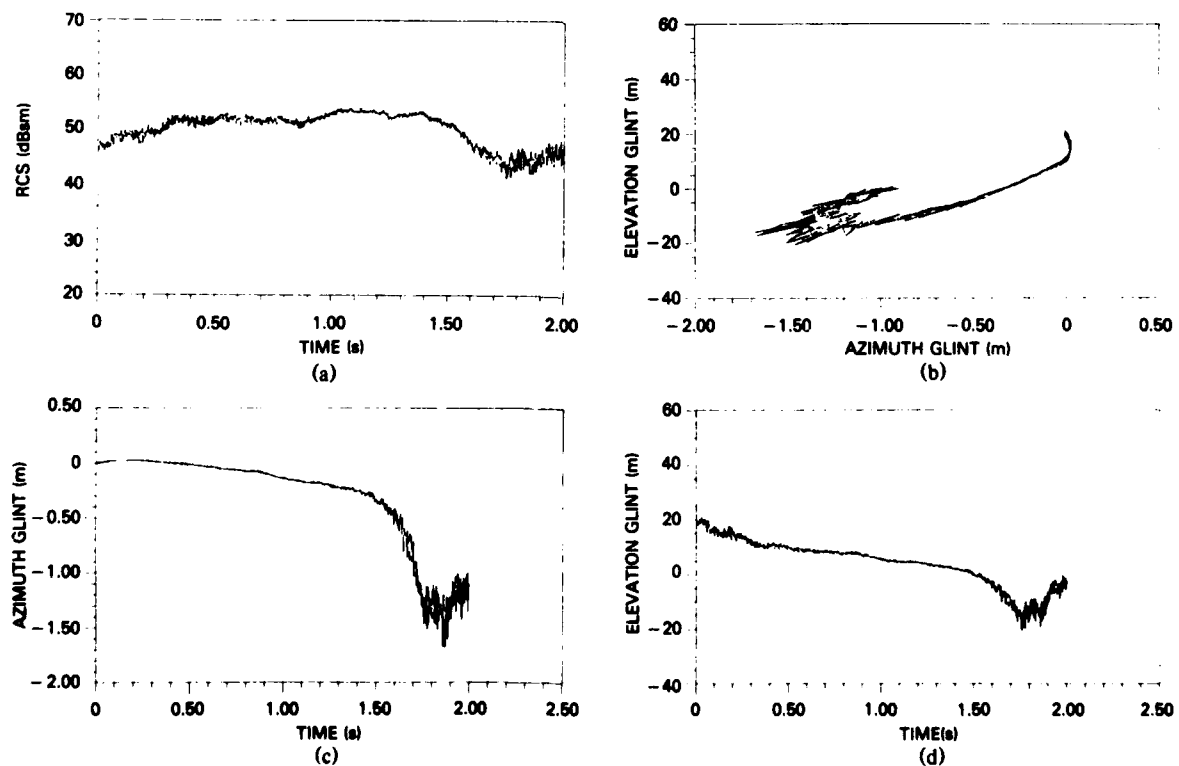
Fig. 9.15 — Ship turn rate = 0.4°/s, stern aspect, rms wave height = 0.135 m
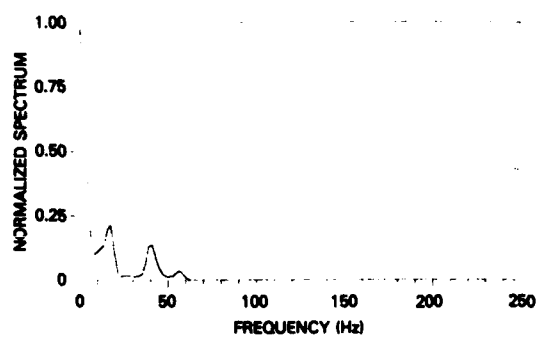
(a) Broadside aspect
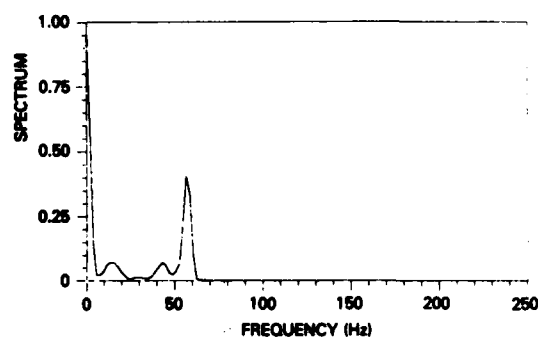
(a) Broadside aspect
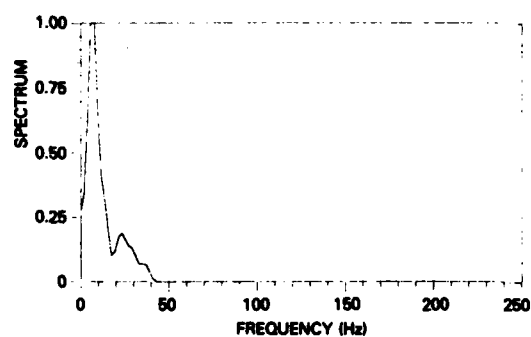
(b) Aft-quarter aspect
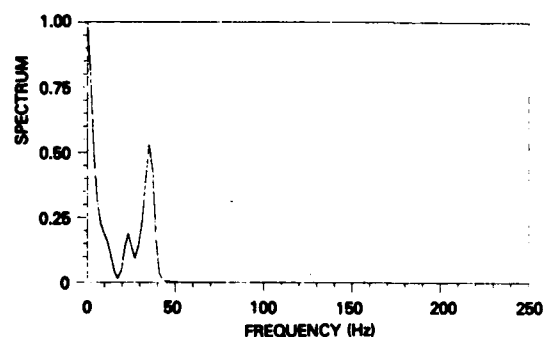
(b) Aft-quarter aspect
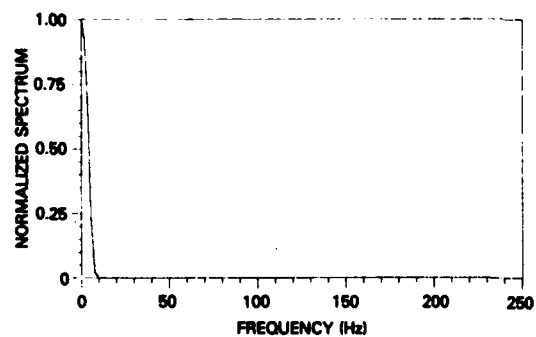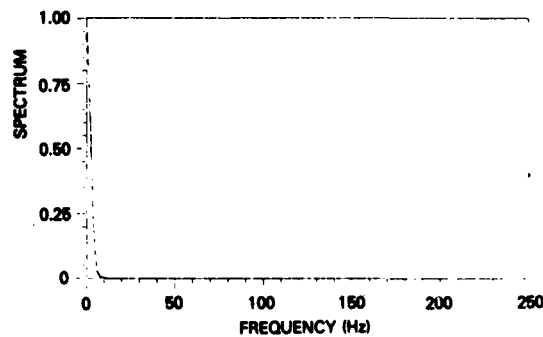
(c) Stern aspect

(c) Stern aspect

Fig. 9.16 — RCS spectra for straight-line motion, ship speed = 10 kn, no multipath

Fig. 9.17 — RCS spectra for straight-line motion, ship speed = 10 kn, rms wave height = 0.762 m

79
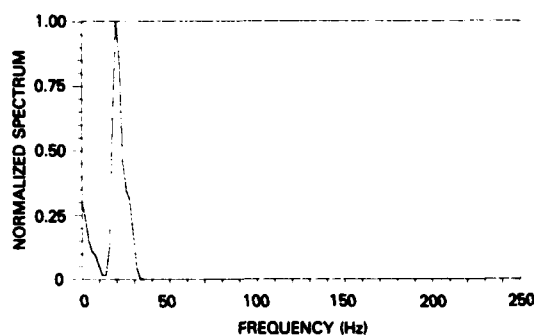
(a) Broadside aspect
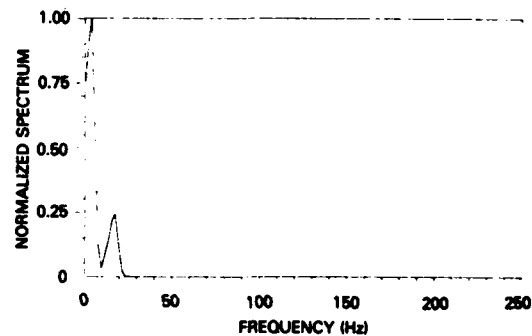
(b) Aft-quarter aspect
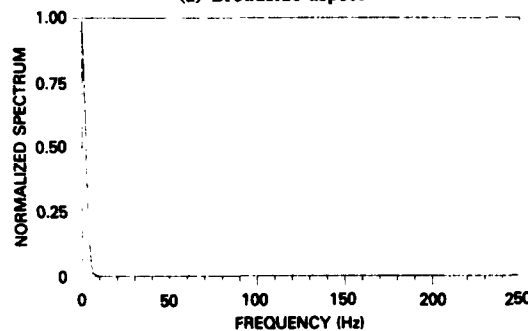
(c) Stern aspect

Fig. 9.18 — RCS spectra for turning motion, ship
speed = 6 kn, rms wave height = 0.135 m
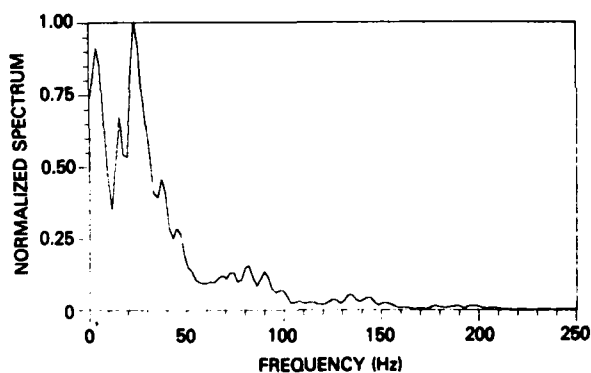
(a) Azimuth glint, no multipath
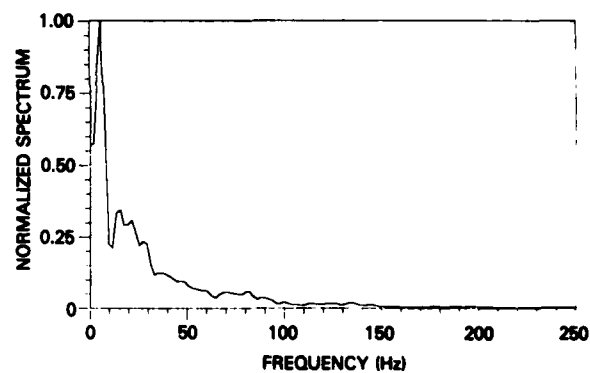
(b) Elevation glint; no multipath
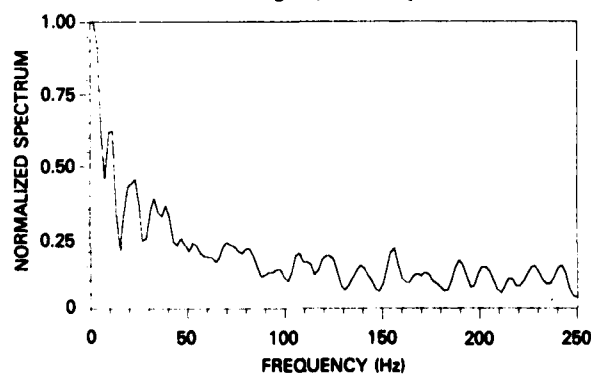
(c) Azimuth glint, rms wave height = 0.762 m
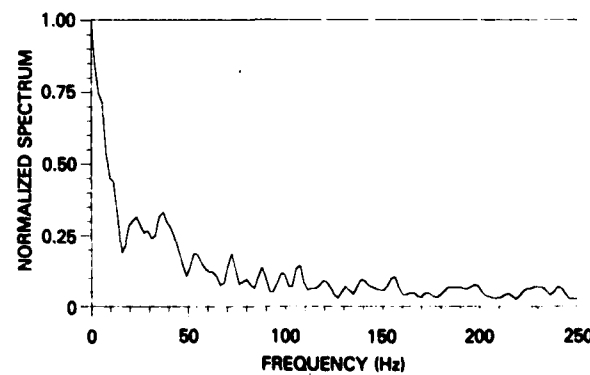
(d) Elevation glint, rms wave height = 0.762 m

Fig. 9.19 — Glint spectra (straight-line motion, ship speed = 10 kn, aft-quarter aspect)

80

A well-known property of glint is also illustrated in the data: sharp decreases in the magnitude of RCS ("fades") produce sharp increases ("spikes") in the magnitude of glint. Recalling from Section 8 that glint is the ratio of two functions where the denominator approximates RCS, we see that this fade-spike correlation is to be expected.

If Figs. 9.4(b) through 9.15(b) are interpreted as scatter diagrams, then we see that azimuth and elevation glint are in general not strongly correlated. Only the stern aspects show strong correlation (due to the associated scenario producing very little signal fluctuation). To further confirm this observation, cross-covariance functions for the glint data of Figs. 9.4, 9.5, 9.7, and 9.8 were calculated (using TSAP) and are plotted as Fig. 9.20. We suspect that the relatively strong but brief correlation that does occur (at zero lag) is due to the simultaneous occurrence of spikes. We also note that multipath appears to contribute to decorrelation between azimuth and elevation glint.

(a) Broadside aspect, no multipath

(b) Aft-quarter aspect, no multipath

(c) Broadside aspect, rms wave height = 0.762 m

(d) Aft-quarter aspect, rms wave height = 0.762 m
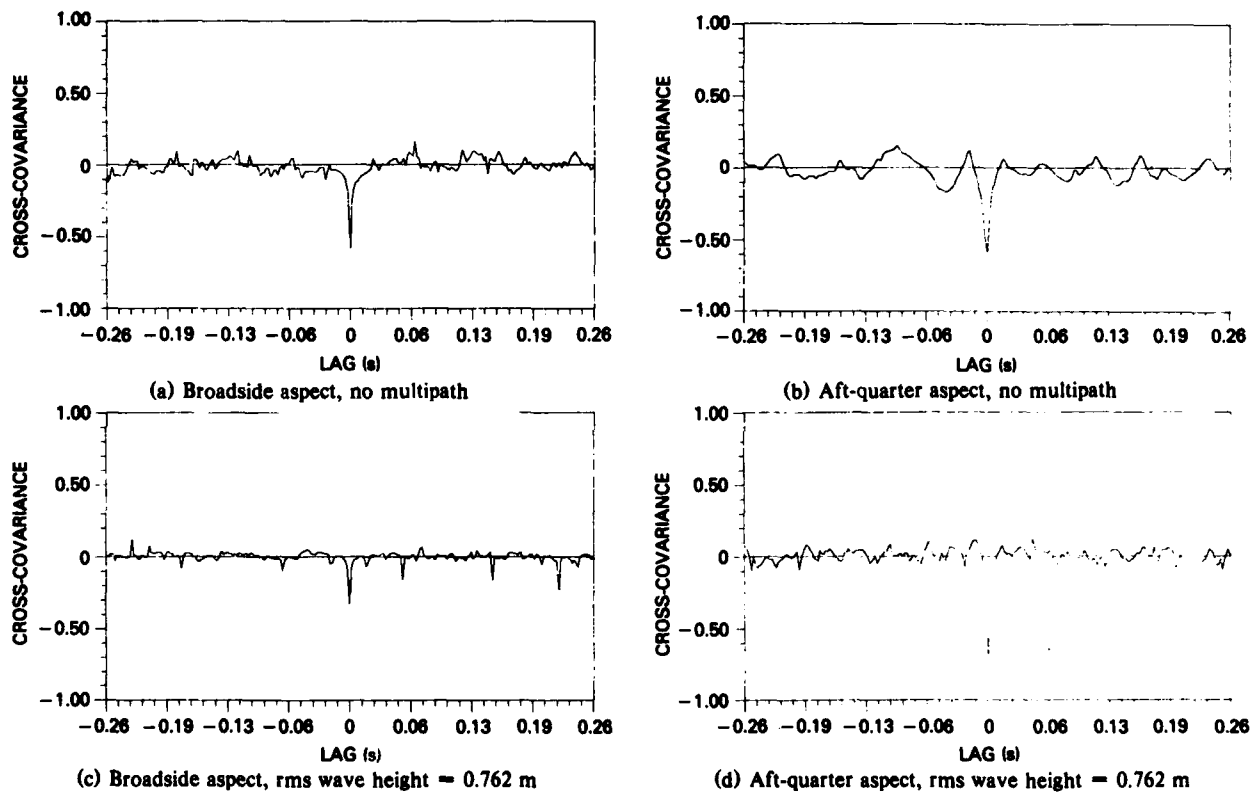
Fig. 9.20 — Cross-covariance functions for the glint data of four simulations
(straight-line motion, ship speed = 10 kn)

An examination of the azimuth-glint plots shows that the data are often asymmetrical about a mean near zero (e.g., in Fig. 9.4(c) the positive values are more correlated (smooth) than the negative values). This suggests that such data may not be Gaussian distributed. (It is known that some radar targets display glint statistics that are approximately Gaussian [97].) This observation was confirmed by using a Kolmorgorov-Smirov test of fit (from TSAP) to test the hypothesis that the azimuth-glint data is Gaussian distributed: for each time series the result was rejection of the hypothesis at an α-level less than 0.01. This result also holds for the elevation-glint data except for one time series: that in Fig. 9.10(d). We comment here that what we simulated was "ideal" glint in the sense that it cannot be exactly measured by radars. Constraints on radar system performance (antenna pattern effects, finite bandwidths, system noise, etc.) may result in error signals that are more symmetrical (due to smoothing of sharp variations) and hence more likely to appear Gaussian.

81

Figure 9.21 illustrates the correlation between RCS and azimuth glint for four of the simulations. We note that a weak but definite correlation exists between these two processes.

(a) Broadside aspect, straight-line motion, ship speed = 10 kn   (b) Broadside aspect, turning rate = 0.4°/s, ship speed = 6 kn

(c) Aft-quarter aspect, straight-line motion, ship speed = 10 kn   (d) Aft-quarter aspect, turning rate = 0.4°/s, ship speed = 6 kn
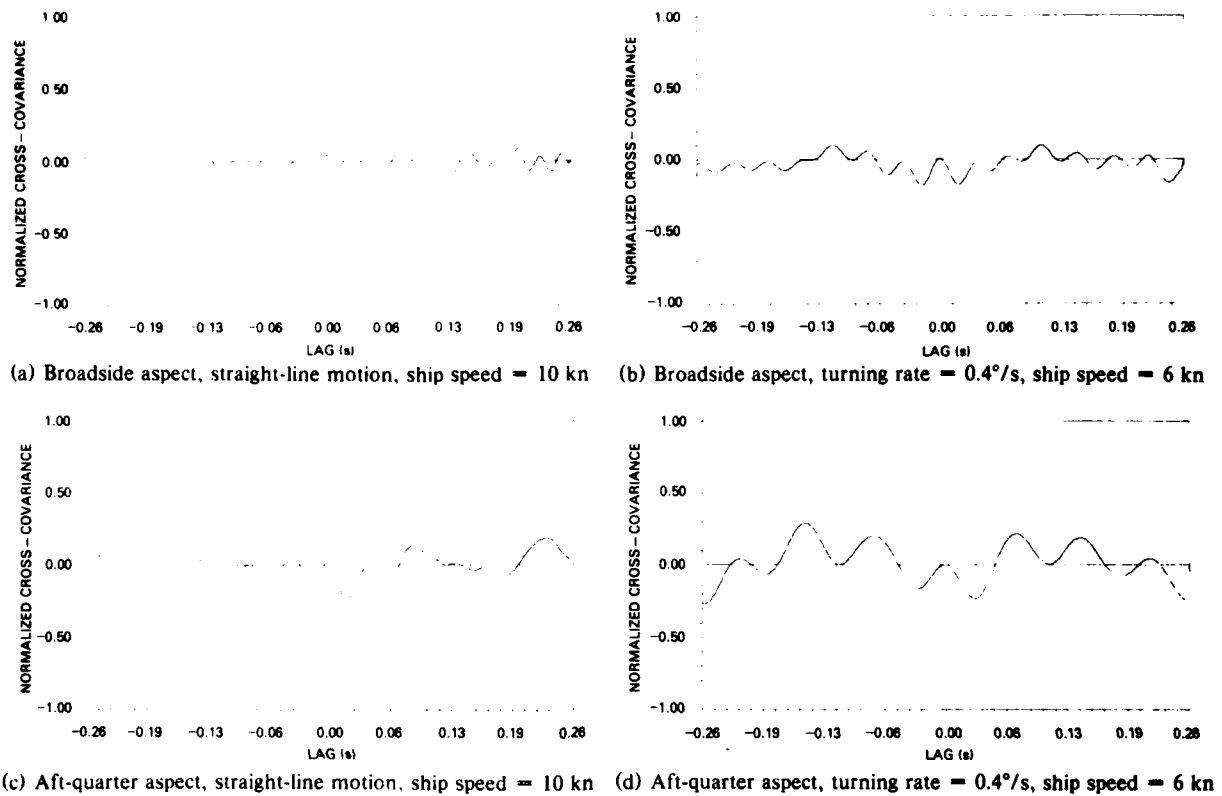
Fig. 9.21 — Normalized cross-covariances between RCS and azimuth glint in the absence of multipath

10. CONCLUSIONS AND FURTHER RESEARCH

The major result of this research is the development of a unified stochastic model and associated simulation for the EM scattering from complex objects in the presence of overwater multipath. By modeling each component of this very complex problem using an N-source formulation, we have obtained a unified RCS-glint model that is useful in applications. We have introduced the concept of unit-scatterer and shown that it is a generic element for use in modeling scattering effects. Though by defining the unit-scatterer as our generic scattering element we have, in a sense, only shifted the scattering problem from the entire object to sub-parts of the object, we suggest that the unit-scatterer concept is fundamental to the practical, pulse-by-pulse modeling and simulation of scattering from complex objects. We believe that it may not be necessary to precisely characterize unit-scatterers to obtain good approximations to the total scattering. If this is the case, then having determined classes of US types one could quickly build models and efficient simulations for the scattering from complex objects by using elements from these classes as building blocks.

We suggest four major areas of research for extension of this work:

(1)   The primary area concerns the identification and characterization of unit-scatterers. Particularly useful (and cost effective) would be simulation studies using the geometric simulations such as those at the NRL and the Georgia Institute of Technology. It would be important to

(a) identify US types,

(b) characterize US amplitude functions, and

(c) characterize US phase functions with emphasis on determining the rate-of-change of phase with US rotation.

(2) Analysis of existing ISAR data for identifying and characterizing unit-scatterers as suggested in the first area.

(3) Second-order-statistical comparisons of simulation data with measured data where the simulation data is generated using the parameters associated with the measured data.

(4) A study of the effects of multipath on objects that are distributed to determine a better model for the multipath effects on unit-scatterers than the existing point-source models.

Appendix A

AN EXAMPLE SIMULATION OF SHIP MOTION

A simulation of the 6 dof motion for a ship's cg is described in Section 6. This appendix presents the output of a simulation that was implemented according to that description. The ship chosen for simulation is the DD963 because that is the ship used as the example in Ref. 78. A ship speed of 10 knots and a relative ship-to-dominant-wave heading of 30° were chosen for the simulation. Figure A1 illustrates the spectra calculated by DTNSRDC for the DD963 at 10 knots. The center frequency, bandwidth, and rms values used in the simulation were estimated from this figure and are listed in Table A1. The frequency increment, $\Delta\omega$, was chosen to be constant and equal to BW/10 for each component process. The simulation runs used a time-step size of 1.0 s in generating six, 2048-point samples. The first 300 points of each of these samples are plotted as Fig. A2. The samples were analyzed using the time series analysis package described in Ref. 79 to estimate the associated spectra and rms values. The resulting rms values are tabulated in Table A2 and normalized spectral estimates are plotted in Fig. A3. Figure A4 illustrates 2-s samples of the motion processes generated by using a time-step size of 0.002 s.

(a) Angular-position spectra (deg)

(b) Linear-position spectra (ft)
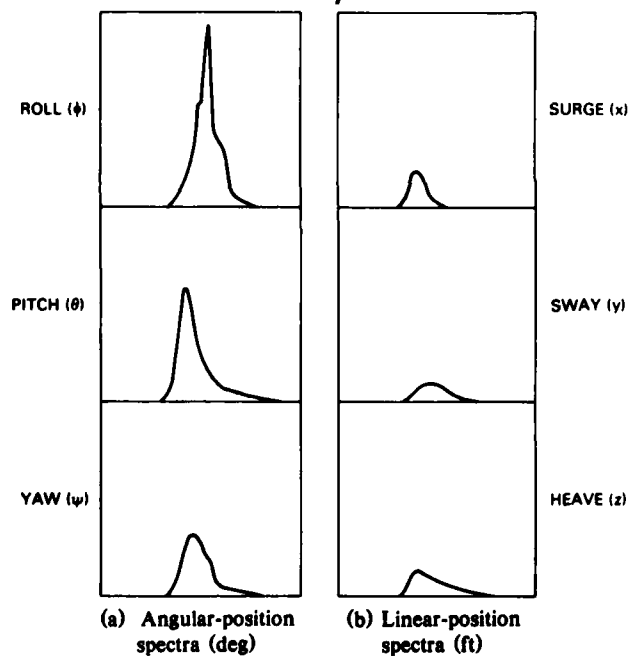
Fig. A1 — DTNSRDC motion spectra for the example simulation

Table A1 — Spectrum Parameters That Were Input to the Example Simulation

Process	ω_0 (Hz)	BW (Hz)	RMS Value
X	0.061	0.018	0.344
Y	0.076	0.029	0.357
Z	0.069	0.025	0.411
PHI	0.083	0.022	0.0539
THETA	0.065	0.018	0.0089
PSI	0.072	0.025	0.0066

(a) Linear positions (m)

(b) Angular positions (rad)
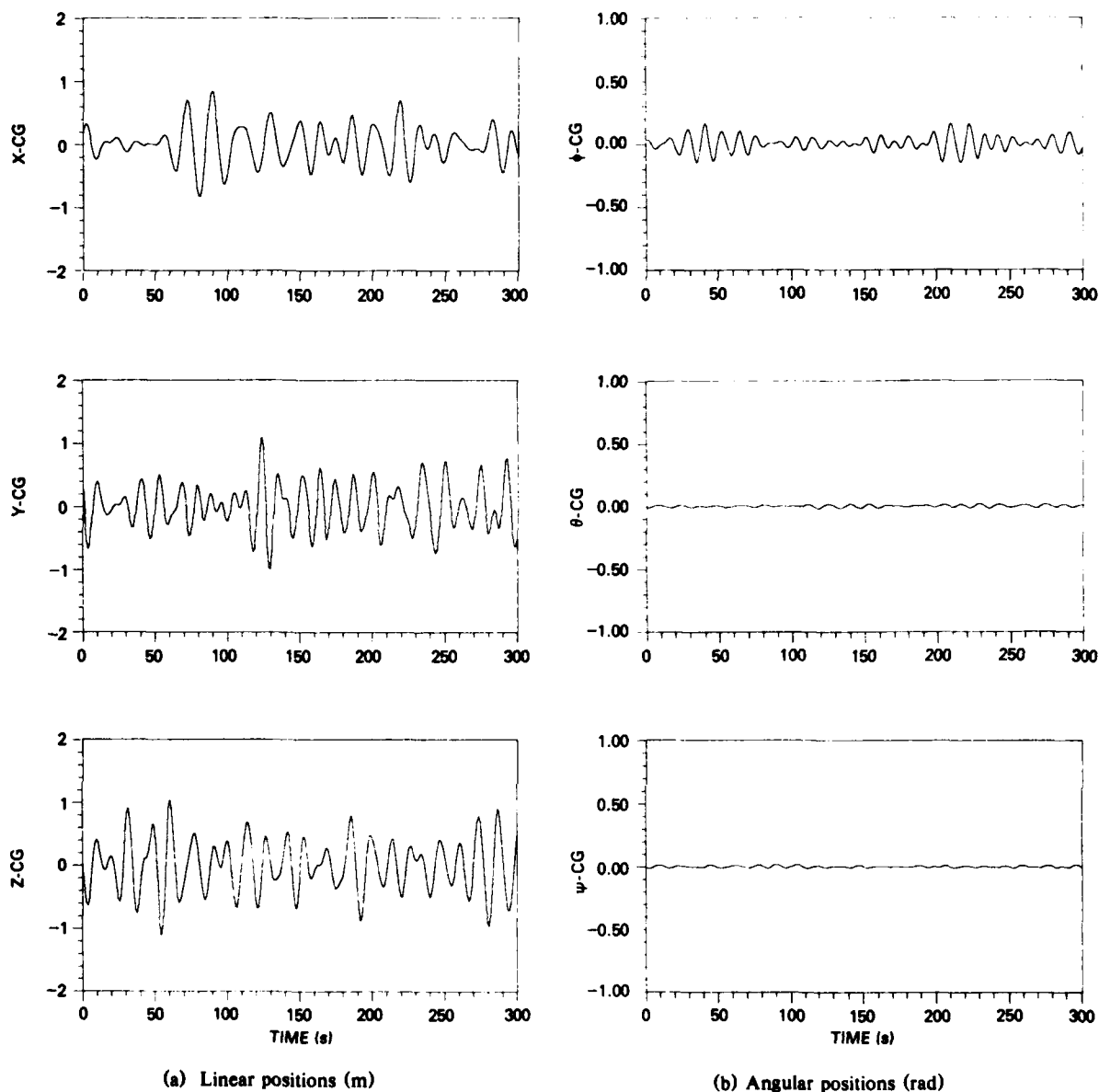
Fig. A2 — The first 300 s of the simulated cg-motion processes

Table A2 — RMS Values of the
Simulated CG-Motion Processes

Process	rms value
X	0.334
Y	0.360
Z	0.417
PHI	0.0538
THETA	0.0088
PSI	0.0067

85
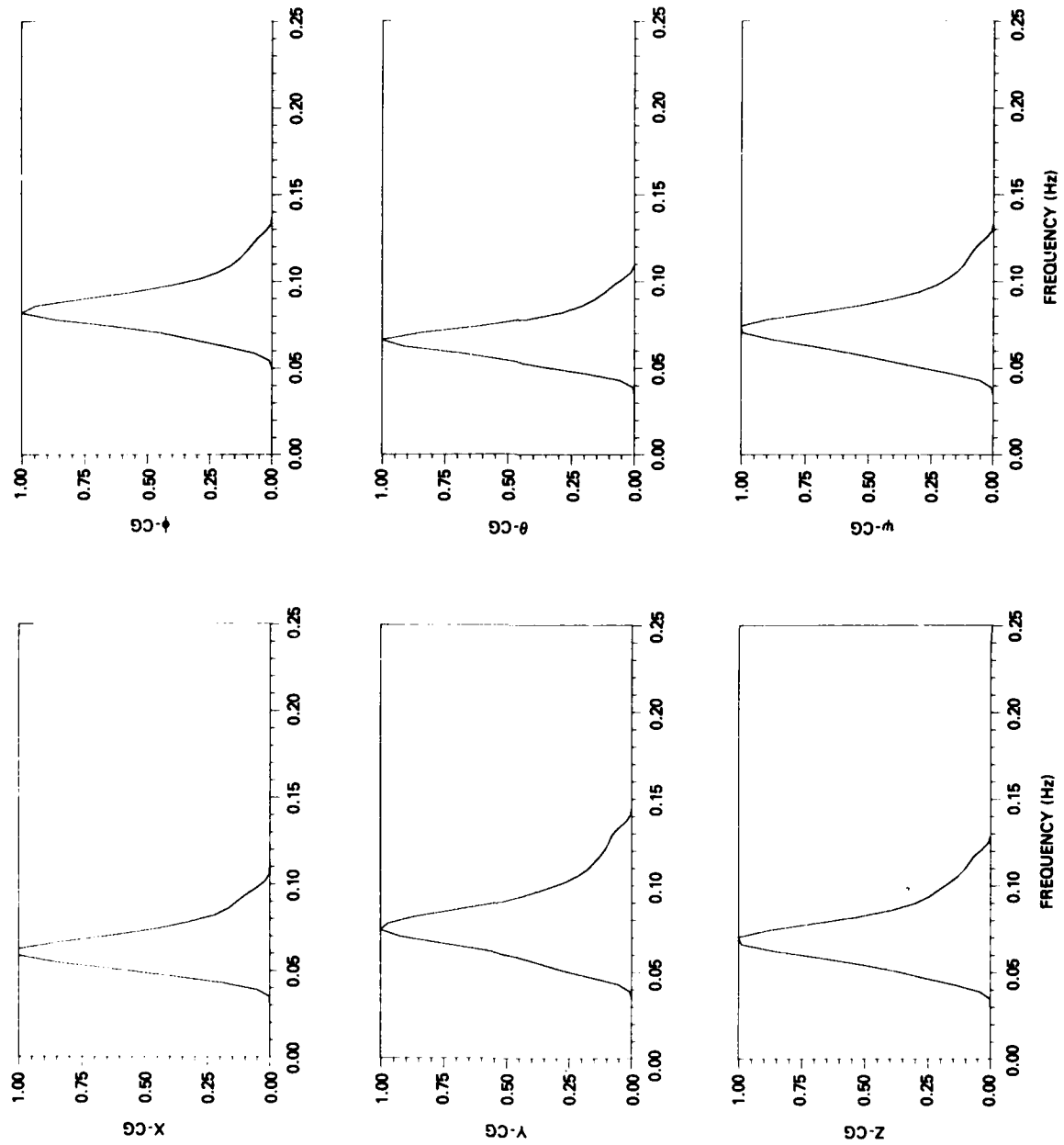
Fig. A3 — Spectra (normalized) of the simulated cg-motion processes
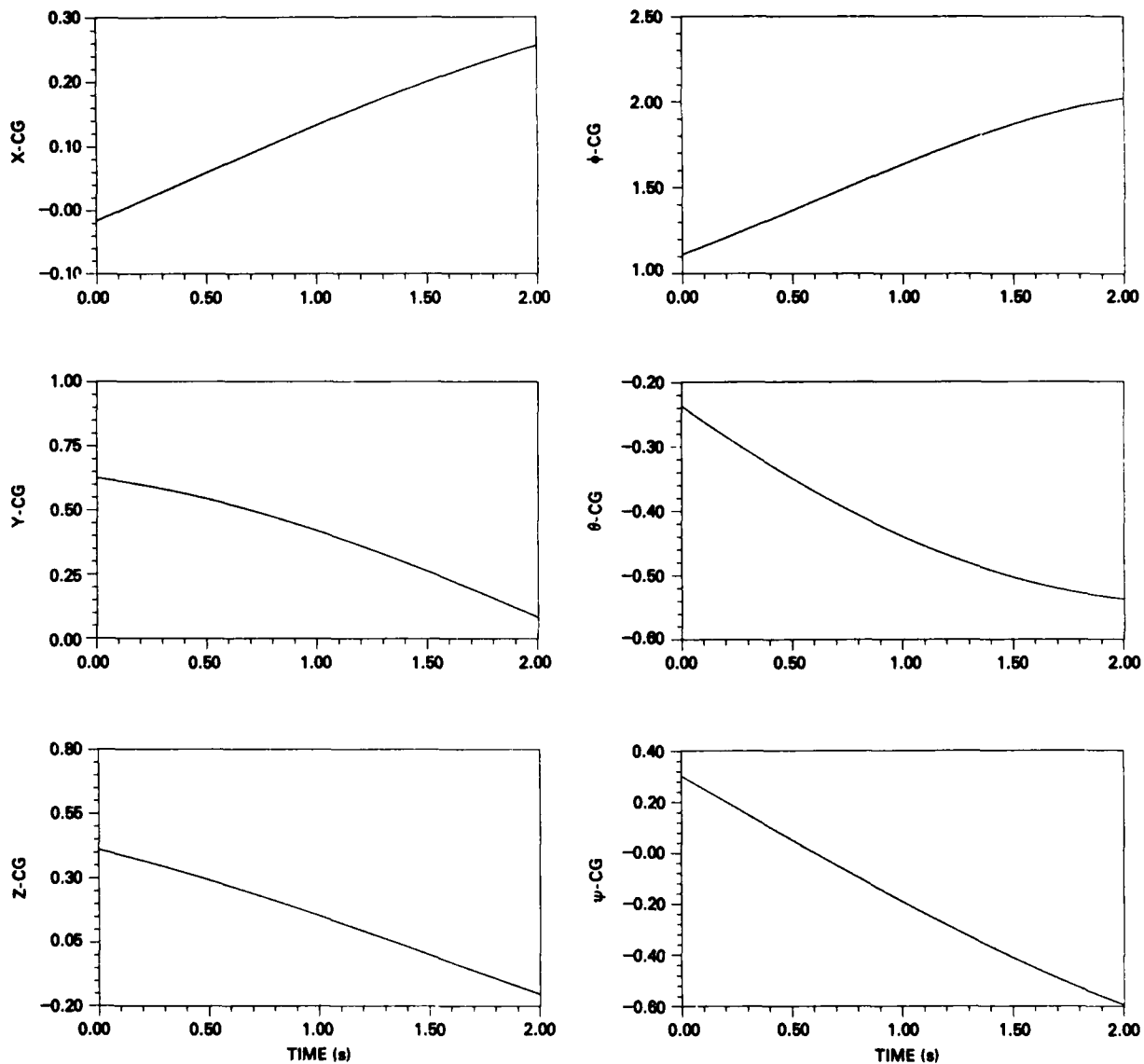
(a) Units of meters

(b) Units of degrees

Fig. A4 — Simulated cg-motion processes for a short time interval

Appendix B
AN ESTIMATE OF RANGE VARIATION DURING
A SHORT TIME PERIOD

Let $\vec{R}_i(t)$ be the range from the radar to a scatterer on the ship. The phase of the received field due to range is

$$\psi_i(t) = \frac{4\pi}{\lambda} |\vec{R}_i(t)|. \tag{B1}$$

To estimate the variation in $|\vec{R}_i(t)|$ over short periods of time, we use the measure

$$E\{\Delta R_i^2\}^{1/2} = E\{(|\vec{R}_i(t+\tau) - \vec{R}_i(t)|)^2\}^{1/2}. \tag{B2}$$

From Eq. (6.5b),

$$\Delta R_i = |T_s(t+\tau)\vec{R}_i^L(t+\tau) + \vec{R}_s^E(t+\tau)| - |T_s(t)\vec{R}_i(t) + \vec{R}_s^E(t)|. \tag{B3}$$

For simplicity we assume that there is no maneuvering, hence $T_s(t) = I$ and $\vec{R}_s^E(t) = \vec{R}_s^E(0)$. Therefore

$$\Delta R_i = |\vec{R}_i^L(t+\tau) + \vec{R}_s^E(0)| - |\vec{R}_i^L(t) + \vec{R}_s^E(0)|. \tag{B4}$$

From Eq. (6.5),

$$\Delta R_i = |\vec{R}_i(0) + T_i[\vec{x}_{cg}(t+\tau) - \vec{x}_{cg}(0)] + \vec{R}_s^E(0)|$$

$$- |\vec{R}_i(0) + T_i[\vec{x}_{cg}(t) - \vec{x}_{cg}(0)] + \vec{R}_s^E(0)|. \tag{B5}$$

Collecting the initial terms,

$$\Delta R_i = |\vec{R}_i^0 + T_i\vec{x}_{cg}(t+\tau)| - |\vec{R}_i^0 + T_i\vec{x}_{cg}(t)|$$

$$\leqslant |T_i[\vec{x}_{cg}(t+\tau) - \vec{x}_{cg}(t)]|. \tag{B6}$$

Expressing the difference in Eq. (B6) in terms of components,

$$\Delta R_i \leqslant |T_i[\Delta x, \Delta y, \Delta z, \Delta\phi, \Delta\theta, \theta\psi]^T| \tag{B7a}$$

and

$$\Delta R_i \leqslant [(\Delta x + z_i\Delta\theta - y_i\Delta\psi)^2 + (\Delta y - z_i\Delta\phi + x_i\Delta\psi)^2 + (\Delta z + y_i\Delta\phi - x_i\Delta\theta)^2]^{1/2} \tag{B7b}$$

so that

$$\Delta R_i^2 \leqslant \Delta x^2 + (z_i \Delta \theta)^2 + (y_i \Delta \psi)^2 + \Delta y^2 + (z_i \Delta \phi)^2 + (x_i \Delta \psi)^2$$
$$+ \Delta z^2 + (y_i \Delta \phi)^2 + (x_i \Delta \theta)^2 + \text{cross-product terms.} \qquad \text{(B8)}$$

Because the component processes were assumed to be independent, we have

$$E\{\Delta R_i^2\} = E\{\Delta x^2\} + E\{\Delta y^2\} + E\{\Delta z\}^2 + (y_i^2 + z_i^2) E\{\Delta \phi^2\}$$

$$+ (x_i^2 + z_i^2) E\{\Delta \theta^2\} + (x_i^2 + y_i^2) E\{\Delta \psi^2\} \qquad \text{(B9a)}$$

where each expectation has the form

$$E\{\Delta x^2\} = E\{[x(t+\tau) - x(t)]^2\} = 2R_x(0) - 2R_x(\tau). \qquad \text{(B9b)}$$

As described in Section 6, a useful approximation to the covariance function for each process has the

form

$$R_i(\tau) = \sigma_i^2 e^{-\alpha_i |\tau|} \cos \omega_{0_i} \tau \qquad \text{(B10)}$$

where α is 1/2 the bandwidth and ω_{0_i} is the center frequency of the ith process. Using these approxi-

mations we have, for example,

$$E\{\Delta x^2\} = E\{(x(t) - x(t+\tau)]^2\} = 2\sigma_x^2[1 - e^{-\alpha_x |\tau|} \cos \omega_{0_x} \tau]. \qquad \text{(B11)}$$

For a ship, three scatterer locations yield the largest values for the position coordinates: the location highest above the ship's cg and the locations at the bow and stern. For the example ship, the DD963, $x_{max} \approx 50$ m, $y_{max} \approx 5$ m, and $z_{max} \approx 15$ m. Because of ship structure, each maximum does not occur at the same location. The broadside aspect presents the largest range variations because the largest angular rate, roll, has the maximum effect on the z-axis components and the largest scatterer-distance from the cg, along the x-axis, also yields its maximum range effect. Even if the scatterer was located such that the location maxima occurred, we find that using the position values above, the process values from Table A1, and a typical PRI of $\tau = 0.002$ s, $E\{\Delta R^2\}^{1/2} \approx 2.1$ cm, and for $\tau = 1.0$ s, $E\{\Delta R^2\}^{1/2} \approx 0.42$ m.

Appendix C

SIMULATION EQUATIONS FOR RCS AND GLINT

We use Eqs. (7.7a) and (7.9) to simulate RCS where, in anticipation of the glint simulation, we modify them to be in the form

$$\sigma = \sum_{i=1}^{2N} \sum_{j=1}^{2N} M_i a_i M_j a_j \cos\left(\Psi_i - \Psi_j\right) \tag{C1a}$$

and

$$\Psi_i - \Psi_j = \frac{4\pi}{\lambda} \left(|\vec{R}_i| - |\vec{R}_j|\right) + \beta_i(\vec{\theta}_i) - \beta_j(\vec{\theta}_j) + \gamma_i(\vec{R}_i, \vec{\theta}_i) - \gamma_j(\vec{R}_j - \vec{\theta}_j) \tag{C1b}$$

where

$$M_k = \begin{cases} |F_k| & , & 1 \leqslant k \leqslant N \\ |F_k(F_k - 1)| & , & N+1 \leqslant k \leqslant 2N \end{cases} \tag{C2a}$$

and

$$\gamma_k = \begin{cases} < F_k & , & 1 \leqslant k \leqslant N \\ < F_k(F_k - 1) & , & N+1 \leqslant k \leqslant 2N. \end{cases} \tag{C2b}$$

We describe in detail the simulation of the multipath coefficients, F_k, in Refs. 49 and 98.

The glint equations used for simulation are Eqs. (8.50). Next, we make an assumption that simplifies those equations for use in the simulation.

Because we have limited our studies to small-grazing-angle illumination of the ship and because the ship's cg is near Earth's surface,

$$R_{z_i}^2 \ll R_{x_i}^2 + R_{y_i}^2 \tag{C3}$$

which implies that (see Fig. 8.5)

$$|\vec{R}_{xy_s}| \approx |\vec{R}_s| \tag{C4a}$$

and

$$|\vec{R}_{xy_i}| \approx |\vec{R}_i|. \tag{C4b}$$

Equations (C4) imply that

$$\sin\psi_s \approx \frac{R_{ys}}{|\vec{R}_s|}, \tag{C5a}$$

$$\cos\psi_s \approx \frac{R_{xs}}{|\vec{R}_s|}, \tag{C5b}$$

$$\sin\psi_i \approx \frac{R_{x_i}}{|\vec{R}_i|}, \tag{C5c}$$

and

$$\cos \psi_i \approx \frac{R_{y_i}}{|\vec{R}_i|}. \tag{C5d}$$

By use of Eqs. (C5), the transformation matrix in Eqs. (8.50) becomes

$$T_{ET} \approx \begin{bmatrix} \cos \theta_s \cos \psi_s & \cos \theta_s \sin \psi_s & -1 \\ \sin \psi_s & -\cos \psi_s & 0 \\ \cos \psi_s & \sin \psi_s & \cos \theta_s \end{bmatrix} \tag{C6}$$

and the cross product term becomes, from Eq. (8.29b),

$$(\hat{m}_i \times \hat{l}_k)e = \cos \psi_i \hat{i} + \sin \psi_i \hat{j} + \cos \theta_k \cos (\psi_k - \psi_i) \hat{k}. \tag{C7}$$

Therefore,

$$(\hat{m}_i \times \hat{l}_k)_s = T_{ET}(\hat{m}_i \times \hat{l}_k)_e$$

$$= [\cos \theta_s \cos \psi_s \cos \psi_i + \cos \theta_s \sin \psi_s \sin \psi_i - \cos \theta_k \cos (\psi_k - \psi_i)]\hat{l}_s$$

$$+ [\sin \psi_s \cos \psi_i - \cos \psi_s \sin \psi_i]\hat{m}_s$$

$$+ [\cos \psi_s \cos \psi_i + \sin \psi_s \sin \psi_i + \cos \theta_s \cos \theta_k \cos (\psi_k - \psi_i)]\hat{n}_s \tag{C8a}$$

$$= [\cos \theta_s \cos (\psi_s - \psi_i) - \cos \theta_k \cos (\psi_k - \psi_i)]\hat{l}_s$$

$$+ \sin (\psi_s - \psi_i)\hat{m}_s + [\cos (\psi_s - \psi_i) + \cos \theta_s \cos \theta_k \cos (\psi_k - \psi_i)\hat{n}_s. \tag{C8b}$$

By use of Eq. (C8b) in Eqs. (8.50), we have

$$G_a \approx |\vec{R}_s| \frac{\displaystyle\sum_{i=1}^{2N} \sum_{j=1}^{2N} M_i a_i M_j a_j \cos (\phi_i - \phi_j) \sin (\psi_s - \psi_i)}{\displaystyle\sum_{i=1}^{2N} \sum_{j=1}^{2N} M_i a_i M_j a_j \cos (\phi_i - \phi_j) \cos (\psi_s - \psi_i)} \tag{C9a}$$

and

$$G_e \approx |\vec{R}_s| \frac{\displaystyle\sum_{i=1}^{2N} \sum_{j=1}^{2N} M_i a_i M_j a_j \cos (\phi_i - \phi_j)[\cos \theta_j \cos (\psi_j - \psi_i) - \cos \theta_s \cos (\psi_s - \psi_i)]}{\displaystyle\sum_{i=1}^{2N} \sum_{j=1}^{2N} M_i a_i M_j a_j \cos (\phi_i - \phi_j) \cos (\psi_s - \psi_i)}$$

$$= |\vec{R}_s| \left\{ \frac{\displaystyle\sum_{i=1}^{2N} \sum_{j=1}^{2N} M_i a_i M_j a_j \cos (\phi_i - \phi_j) \cos \theta_j \cos (\psi_j - \psi_i)}{\displaystyle\sum_{i=1}^{2N} \sum_{j=1}^{2N} M_i a_i M_j a_j \cos (\phi_i - \phi_j) \cos (\psi_s - \psi_i)} - \cos \theta_s \right\}. \tag{C9b}$$

Because sine, cosine, and arctangent functions are time-expensive on digital computers, we use Eqs. (C5) in Eqs. (C9) to obtain

$$(\hat{m}_i \times \hat{l}_k)_s \approx \left\{ \frac{R_{z_s}}{|\vec{R}_s|} \left[\frac{R_{x_s}R_{x_i} - R_{y_s}R_{y_i}}{|\vec{R}_s| \cdot |\vec{R}_i|} \right] - \frac{R'_{z_k}}{|\vec{R}_k|} \left[\frac{R_{x_k}R_{x_i} - R_{y_k}R_{y_i}}{|\vec{R}_i| \cdot |\vec{R}_k|} \right] \right\} \hat{l}_s$$

$$+ \frac{R_{y_s}R_{x_i} - R_{x_s}R_{y_i}}{|\vec{R}_s| \cdot |\vec{R}_i|} \hat{m}_s + \frac{R_{x_s}R_{x_i} + R_{y_s}R_{y_i}}{|\vec{R}_s| \cdot |\vec{R}_i|} \hat{n}_s, \tag{C10}$$

where we recall from Section 8 that

$$\vec{R}_i = \begin{cases} R_{x_i}\hat{i} + R_{y_i}\hat{j} + R_{z_i}\hat{k} & , \quad i \leq i \leq N \\ R_{x_i}\hat{i} + R_{y_i}\hat{j} - (h_R + h_i)\hat{k} & , \quad N+1 \leq i \leq 2N \end{cases} \tag{C11a}$$

$$= R_{x_i}\hat{i} + R_{y_i}\hat{j} + R'_{z_i}\hat{k}. \tag{C11b}$$

Therefore the simulation equations for glint become

$$G_a \approx |\vec{R}_s|$$

$$\frac{\sum_{i=1}^{2N}\sum_{j=1}^{2N} M_i a_i M_j a_j \cos(\phi_i - \phi_j)\left|\dfrac{R_{y_s}R_{x_i} - R_{x_s}R_{y_i}}{|\vec{R}_i|}\right|}{\sum_{i=1}^{2N}\sum_{j=1}^{2N} M_i a_i M_j a_j \cos(\phi_i - \phi_j)\left|\dfrac{R_{x_s}R_{x_i} - R_{y_s}R_{y_i}}{|\vec{R}_i|}\right|} \tag{C12a}$$

and

$$G_e \approx |\vec{R}_s|$$

$$\frac{\sum_{i=1}^{2N}\sum_{j=1}^{2N} M_i a_i M_j a_j \cos(\phi_i - \phi_j)\dfrac{R'_{z_j}}{|\vec{R}_j|}\left|\dfrac{R_{x_j}R_{x_i} + R_{y_j}R_{y_i}}{|\vec{R}_j| \cdot |\vec{R}_i|}\right|}{\sum_{i=1}^{2N}\sum_{j=1}^{2N} M_i a_i M_j a_j \cos(\phi_i - \phi_j)\left|\dfrac{R_{x_s}R_{x_i} - R_{y_s}R_{y_i}}{|\vec{R}_s| \cdot |\vec{R}_i|}\right|}$$

$$- \frac{R_{z_s}}{|\vec{R}_s|}\Bigg| \tag{C12b}$$

$$= |\vec{R}_s|$$

$$\frac{\sum_{i=1}^{2N}\sum_{j=1}^{2N} M_i a_i M_j a_j \cos(\phi_i - \phi_j)R'_{z_j}\left|\dfrac{R_{x_j}R_{x_i} + R_{y_j}R_{y_i}}{|\vec{R}_i| \cdot |\vec{R}_s|}\right|}{\sum_{i=1}^{2N}\sum_{j=1}^{2N} M_i a_i M_j a_j \cos(\phi_i - \phi_j)\left|\dfrac{R_{x_s}R_{x_i} - R_{y_s}R_{y_i}}{|\vec{R}_i| \cdot |\vec{R}_s|}\right|} \tag{C12c}$$

$$- R_{z_s}.$$

Finally we note that because of the long-range assumption, $(\psi_s - \psi_i)$ and $(\psi_i - \psi_j)$ are small angles so that

$$\cos(\psi_s - \psi_i) \approx 1 \tag{C13a}$$

and

$$\cos(\psi_i - \psi_j) \approx 1. \tag{C13b}$$

By use of Eqs. (C13) in Eq. (C12a) and Eq. (C12b), we have

$$G_a \approx |\vec{R}_s| \frac{\displaystyle\sum_{i=1}^{2N} \sum_{j=1}^{2N} M_i a_i M_j a_j \cos(\phi_i - \phi_j) \left[\frac{R_{y_s} R_{x_i} - R_{x_s} R_{y_i}}{|\vec{R}_i|}\right]}{\displaystyle\sum_{i=1}^{2N} \sum_{j=1}^{2N} M_i a_i M_j a_j \cos(\phi_i - \phi_j)} \qquad \text{(C14a)}$$

and

$$G_e \approx |\vec{R}_s| \left[\frac{\displaystyle\sum_{i=1}^{2N} \sum_{j=1}^{2N} M_i a_i M_j a_j \cos(\phi_i - \phi_j) R_{z_j}' \left[\frac{R_{x_j} R_{x_i} + R_{y_j} R_{y_i}}{|\vec{R}_i| \cdot |\vec{R}_j|^2}\right]}{\displaystyle\sum_{i=1}^{2N} \sum_{j=1}^{2N} M_i a_i M_j a_j \cos(\phi_i - \phi_j)}\right] - R_{z_s}. \qquad \text{(C14b)}$$

93

Appendix D

SIMULATION DESCRIPTION AND SOURCE-CODE LISTINGS

The simulation was written in FORTRAN and run on a PRIME computer system. A flow chart is presented in Fig. D1. Parameters are input (1) directly by the user and (2) via data files. An example of user-interactive data is shown, in the proper sequence, in Table D1. The first input data-file defines the ship-motion spectra and the second defines the US parameters; example files appear in Figs. D2 and D3. The ship-motion input-file is called SHIP-PARMS and the US-parameters input-file is called SCATT-PARMS. Data are output in binary format, one record per time increment. The output file-names are defined in a DATA statement in subroutine INIT. We note that the compiler replaces the PRIME statement

$INSERT filename

with the contents of the file that is named 'filename'.
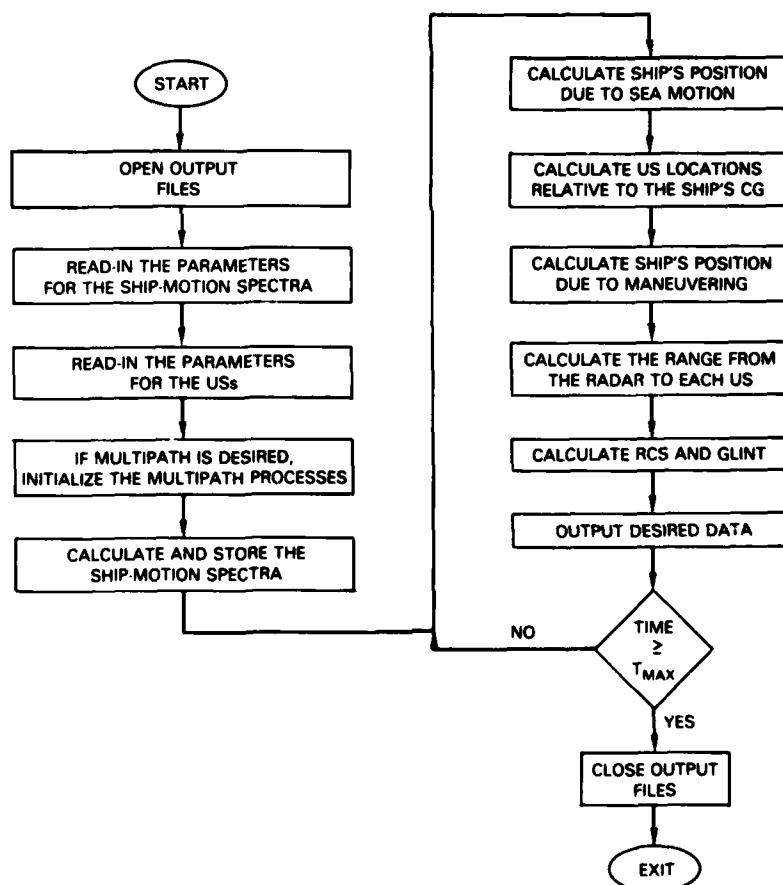
Fig. D1 — Simulation flow chart

Table D1 — The User
Input-Sequence

0.0300	Radar Wave Length
0.0	Pct. Range Error
0.002	Step Size
0.135	Wave RMS
Yes	Multipath Indicator
10.00	Run Time
10000,7,0	Initial Ship Position
0.0,3.19,0	Initial Ship Speeds
88.0	Initial Ship Orientation
0.0070	Ship Turn Rate

SCATTERER DEFINITIONS

LOCATION		(WRT CG)	RCS	SCATT.	PLATE
X	Y	Z	AMP	TYPE	DIAM
-----	-----	-----	-----	-----	-----
-50.	-4.	2.	4.	3	0.
-5.	-4.	7.	0.	2	5.
3.	0.	20.	3.	3	0.
10.	-4.	7.	0.	2	5.
20.	-4.	7.	0.	2	3.
30.	-3.	15.	5.	3	0.

Fig. D2 — A *US*-parameter input-file

CG-PROCESSES SPECTRUM-DEFINITION

CENT FREQ (RAD/S)	BW (RAD/S)	RMS VALUE	PROCESS
-----	-----	-----	-----
0.386	0.114	0.344	X
0.477	0.182	0.357	Y
0.432	0.159	0.411	Z
0.523	0.136	0.0539	PHI
0.409	0.114	0.0089	THETA
0.455	0.159	0.0066	PSI

Fig. D3 — A ship-motion input-file

The remainder of this appendix lists the insert files followed by the source-code except for that used to simulate multipath. The multipath source code is presented in Ref. 98.

95

```
C   $INSFRT FILES (PRIMF FORTRAN)
C----------------------------------------------------------------
C   $INSERT SIZE
        INTEGFR DIMEN,DIMEN2
        PARAMETER (DIMFN=25)
        PARAMETER (DIMFN2=DIMEN*2)

C   $INSERT BLOCK1
        INTFGER*4 ISEED
        COMMON/BLOCK1/ISFED,DT,TIME

C   $INSERT BLOCK2
        COMMON/BLOCK2/XYZ(3,DIMFN),AMP(DIMEN),T(3,6,DIMEN),
       *               CNTFRC(6),BNDWTH(6),RMS(6),RNGERR,WAVRMS,RADHGT


C   FILE: MAIN
C--------------------------------------------------------------------
        CALL DRIVFR
        CALL EXIT
        FND


C   FILF: DRIVER
C--------------------------------------------------------------------
C   PURPOSE:
C     TO GENERATE A TIME SERIES OF RADAR SIGNALS RESULTING FROM
C     ILLUMINATION OF A SHIP AT LONG RANGF. THIS ROUTINE IS THE
C     DRIVER FCR THF PACKAGE.
C
C   INPUT:
C     ARGUMENTS:
C       NONF.
C
C   OUTPUT:
C     ARGUMENTS:
C       NONF.
C
C   AUTHOR: D.Y.NCRTHAM.
C   DEVELOPED: 4/82.
C   MODIFIED: 1982, 1983.
C--------------------------------------------------------------------
        SUBROUTINF DRIVER
$INSFRT SYSCOM>ASKEYS
$INSFRT RCS>ROUTINFS>SIZF
$INSFRT RCS>ROUTINFS>BLOCK1
$INSFRT RCS>ROUTINFS>BLOCK2
        DOUBLE PRFCISION TMP,DELRI(3,DIMEN)
        DOUBLF PRFCISION DX,DY,DZ,DR
        LOGICAL UPDATE(DIMEN),FIRST(DIMEN),MFFLAG
        INTEGFR SCTTYP(DIMFN)
        PARAMETER (PION2=1.571,TWOPI=6.2832)
        DIMENSION LUNITS(9),XSWIF(6),XCG(6),RI(3,DIMEN),FSI(DIMEN),
       *           DIAM(DIMEN)
C
C   INITIALIZE SIMULATION
```

96

```
      CALL INIT(LUNITS,NSCATT,SCTTYP,DIAM,WAVLEN,MPFLAG)
      LUN1=LUNITS(1)
      LUN2=LUNITS(2)
      LUN3=LUNITS(3)
      LUN4=LUNITS(4)
      LUN5=LUNITS(5)
      LUN6=LUNITS(6)
      LUN7=LUNITS(7)
      LUN8=LUNITS(8)
      LUN9=LUNITS(9)
   10 CALL TNOUA('ENTER MAX TIME: ',16)
      READ(1,*,ERR=10) TMAX
      MAX=TMAX/DT+1
      DO 15 I=1,DIMEN
        FIRST(I)=.TRUE.
        UPDATE(I)=.TRUE.
   15 CONTINUE
C
C  BEGIN SIMULATION LOOP
      DO 90 I=1,MAX
        TIME=DT*I
C
C  UPDATE 6 DOF POSITION VALUES FOR SHIP'S CG
      DO 20 J=1,6
        CALL PROCES(J,CNTFPQ(J),BNDWTH(J),0,.FALSE.,XCG(J),TIME)
        XCG(J)=RMS(J)*XCG(J)
   20   CONTINUE
C
C  UPDATE SCATTERER POSITIONS
      DO 35 K=1,NSCATT
        CALL LINMAP(T(1,1,K),3,6,XCG,RI(1,K))
        DO 30 J=1,3
          RI(J,K)=RI(J,K)+XYZ(J,K)
   30     CONTINUE
   35   CONTINUE
C
C  UPDATE SHIP MANEUVERING POSITION
      CALL SHIP(TIME,XSHIP)
C
C  UPDATE RADAR-TO-SCATTERER RANGE
      DO 40 K=1,NSCATT
        CALL TRNSFR(RI(1,K),XSHIP,RADHGT,DBLRI(1,K))
        PSI(K)=ASPECT(XSHIP(1),XSHIP(2),XSHIP(6),K,FIRST(K))+XCG(6)
   40 CONTINUE
C
C  UPDATE RCS AND GLINT PROCESSES
      PHI=XCG(4)
      CALL SIGNIS(PSI,NSCATT,SCTTYP,DIAM,PHI,WAVLEN,DBLRI,XSHIP,
     *            RCS,AZGLNT,ELGLNT,MPFLAG)
C
C  OUTPUT DESIRED DATA
      WRITE(LUN7) RCS
      WRITE(LUN8) AZGLNT
      WRITE(LUN9) ELGLNT
C
C  TURN OFF INITIALIZATION FLAGS
      DO 80 K=1,NSCATT
```

```
             IF(.NOT.FIRST(K)) GO TO 80
                FIRST(K)=.FALSE.
                UPDATE(K)=.FALSE.
    80    CONTINUE
    90 CONTINUE
C
C  CICSE OUTPUT FILES
         DO 100 I=1,9
            CALL CLOSSA(LUNITS(I)-4)
   100 CONTINUE
C
C  END OF SIMULATION
         RETURN
         END


C  FILE: INIT
C------------------------------------------------------------------
C  PURPOSE:
C     TO INITIALIZE THE SIMULATION PARAMETERS.
C
C  INPUT:
C     ARGUMENTS:
C        NONE.
C
C  OUTPUT:
C     ARGUMENTS:
C        LUNITS     =LOGICAL UNIT NUMBERS FOR THE OUTPUT FILES.
C        NSCATT     =NUMBER OF SCATTERERS.
C        SCTTYP     =INDEX INDICATING TYPE OF SCATTERER.
C                   =1 FOR CONSTANT TYPE.
C                   =2 FOR FLAT-PLATE TYPE.
C                   =3 FOR CORNER TYPE.
C        DIAM       =DIAMETERS OF THE FLAT PLATE SCATTERERS.
C        WAVLEN     =RADAR WAVE LENGTH.
C        MPFLAG     =MULTIAPTH FLAG.
C                   =.TRUE. IF MULTIPATH EFFECTS ARE TO BE ACCOUNTED FOR.
C                   =.FALSE. OTHERWISE.
C        /BLOCK1/:
C        DT         =SIMULATION STEP SIZE.
C        ISEED      =RANDOM NUMBER GENERATOR SEEDS (I*4).
C        /BLOCK2/:
C        RADHGT     =HEIGHT OF THE RADAR ABOVE THE SEA.
C        CNTERQ     =CENTER FREQUENCIES OF THE SHIP-MOTION SPECTRA.
C        BNDWTH     =BANDWIDTH OF THE SHIP-MOTION SPECTRA.
C        RMS        =RMS VALUES OF THE SHIP MOTION PROCESSES.
C        RNGERP     =RANGE ERROR IN THE PHASE CENTER LOCATION.
C        XYZ        =CARTESIAN COORDINATES OF THE SCATTERING CENTERS
C                    IN THE SHIP-CG AXIS SYSTEM.
C        AMP        =AMPLITUDES OF THE SCATTERERS.
C        T          =TRANSFORMATION FROM SHIP-CG 6-DOF POSITION TO
C                    SCATTERER 6-DOF POSITION.
C
C  AUTHOR: D.Y.NORTHAM.
C  DEVELOPED: 4/82.
C  MODIFIED: 1982.
C------------------------------------------------------------------
```

```
      SUBROUTINE INIT(LUNITS,NSCATT,SCTTYP,DIAM,WAVLEN,MPFLAG)
$INSERT SYSCOM>ASKEYS
$INSERT RCS>ROUTINES>SIZE
$INSERT RCS>ROUTINES>BLOCK1
$INSERT RCS>ROUTINES>BLOCK2
      INTEGER LUNITS(1),FNAM(8,9)
      INTEGER SCTTYP(NSCATT)
      LOGICAL FUNIT,YESNO,MPFLAG
      INTEGER*4 I1,I2
      PARAMETER (TWOPI=6.2832)
      DATA FNAM/'X-CG',6*'   ',
     *          'Y-CG',6*'   ',
     *          'Z-CG',6*'   ',
     *          'PHI-CG',5*'   ',
     *          'THETA-CG',4*'   ',
     *          'PSI-CG',5*'   ',
     *          'RCSMAG',5*'   ',
     *          'AZ-GLINT',4*'   ',
     *          'EL-GLINT',4*'   '/
C
      ISEED=1
      RADHGT=40.0
    3 CALL TNOUA('ENTER RADAR WAVLENGTH: ',23)
      READ(1,*,ERR=3) WAVLEN
      CALL GETSCT(XYZ,NSCATT,AMP,SCTTYP,DIAM)
      DO 5 I=1,NSCATT
        IF(SCTTYP(I).EQ.3) AMP(I)=AMP(I)/WAVLEN
    5 CONTINUE
      CALL GETPRM(CNTFRQ,BNDWTH,RMS)
      CALL GETMAP(XYZ,NSCATT,T)
    7 CALL TNOUA('ENTER PERCENT RANGE ERROR: ',27)
      READ(1,*,ERR=7) PCT
      RNGERR=WAVLEN*(PCT/100.)
   10 CALL TNOUA('ENTER STEP SIZE: ',17)
      READ(1,*,ERR=10) DT
C
C   OPEN OUTPUT FILES
      DO 45 I=1,9
        IF(FUNIT(NFU)) GO TO 40
          STOP
   40   CALL OPENSA(ASWRIT+ASSAMF,FNAM(1,I),16,NFU)
        LUNITS(I)=NFU+4
   45 CONTINUE
C
C   SET UP FOR MULTIPATH
   46 CALL TNOUA('ENTER WAVE RMS: ',16)
      READ(1,*,ERR=46) WAVRMS
      IF(.NOT.YESNO('USE MULTIPATH? ')) GO TO 55
        MPFLAG=.TRUE.
        I1=101
        I2=1001
        DO 50 I=1,NSCATT
          CALL MPINIT(I,0.0,WAVRMS,WAVLEN,0,I1,I2,DT)
          I1=I1+5
          I2=I2+6
   50   CONTINUE
        GO TO 60
```

```
   55   MPFLAG=.FALSE.
   60 CONTINUE
C
C  CALCULATE AND STORE SPECTRA
      DO 70 I=1,6
         CALL PROCES(I,CNTFRQ(I),BNDWTH(I),INTL(I),.TRUE.,RMDVAR,0.0)
   70 CONTINUE
      RETURN
      END


C  FILE: GETSCT
C---------------------------------------------------------------------
C  PURPOSE:
C    TO READ IN THE SCATTERING PARAMETERS FOR THE INDIVIDUAL
C    UNIT-SCATTERERS.
C
C  INPUT:
C    ARGUMENTS:
C      NONE.
C
C  OUTPUT:
C    ARGUMENTS:
C      XYZ(3,I)     =CARTESIAN COORDS. OF SCATTERER LOCATIONS
C                     IN THE SHIP-CG AXIS SYSTEM.
C      NSCATT       =NUMBER OF SCATTERERS.
C      AMP          =AMPLITUDE OF THE SCATTERERS.
C      SCTTYP       =INDICATES TYPE OF SCATTERER.
C      DIAM         =FLAT PLATE DIAMETER, IF APPROPRIATE.
C
C  AUTHOR: D.Y.NORTHAM.
C  DEVELOPED: 4/82.
C  MODIFIED: 1982.
C---------------------------------------------------------------------
      SUBROUTINE GETSCT(XYZ,NSCATT,AMP,SCTTYP,DIAM)
SINSERT SYSCOM>ASKEYS
      INTEGER FNAME(16)
      LOGICAL FUNIT
      INTEGER SCTTYP(NSCATT)
      DIMENSION XYZ(3,NSCATT),AMP(NSCATT),DIAM(NSCATT)
      DATA FNAME/'SCATT-PARMS ',10*'  '/
C
C  OPEN INPUT FILES AND READ IN SCATTERING PARAMETERS
      IF(FUNIT(NFU)) GO TO 10
        STOP
   10 CALL OPENSA(ASPRAD+ASSAMF,FNAME,32,NFU)
      LUN=NFU+4
      READ(LUN,11) DUM1,DUM2,DUM3,DUM4
   11 FORMAT(A4/A4/A4/A4)
      NSCATT=0
      DO 15 I=1,100
         READ(LUN,*,END=20,ERR=20) XYZ(1,I),XYZ(2,I),XYZ(3,I),AMP(I),
     *                             SCTTYP(I),DIAM(I)
         NSCATT=NSCATT+1
   15 CONTINUE
   20 CONTINUE
C
```

```
C  WRITE MESSAGE AND CLOSE INPUT FILE
      WRITE(1,25) NSCATT
   25 FORMAT(' THERE ARE',I3,' SCATTERERS.')
      CALL CLOSSA(NFU)
      RETURN
      END


C  FILE: GETPRM
C--------------------------------------------------------------------
C  PURPOSE:
C    TO READ IN THE SHIP-MOTION-PROCESS PARAMETERS.
C
C  INPUT:
C    ARGUMENTS:
C      NONE.
C
C  OUTPUT:
C    ARGUMENTS:
C      CNTFRQ    =CENTER FREQUENCIES OF THE SHIP-MOTION SPECTRA.
C      BNDWTH    =BANDWIDTH OF THE SHIP-MOTION SPECTRA.
C      RMS       =RMS VALUES OF THE SHIP MOTION PROCESSES.
C
C  AUTHOR: D.Y.NORTHAM.
C  DEVELOPED: 4/82.
C  MODIFIED: 1982.
C--------------------------------------------------------------------
      SUBROUTINE GETPRM(CNTFRQ,BNDWTH,RMS)
$INSERT SYSCOM>ASKEYS
      INTEGER FNAME(16)
      LOGICAL FUNIT
      DIMENSION CNTFRQ(6),BNDWTH(6),RMS(6)
      DATA FNAME/'SHIP-PARMS',11*'  '/
C
C  OPEN INPUT FILE AND READ IN MOTION PARAMETERS
      IF(FUNIT(NFU)) GO TO 10
        STOP
   10 CALL OPENSA(ASREAD+ASSAMF,FNAME,32,NFU)
      IUN=NFU+4
      READ(LUN,13) DUM1,DUM2,DUM3
   13 FORMAT(A4/A4/A4)
      NPARMS=0
      DO 15 I=1,6
        NPARMS=NPARMS+1
        READ(LUN,*) CNTFRQ(I),BNDWTH(I),RMS(I)
   15 CONTINUE
C
C  CLOSE INPUT FILE
   20 CALL CLOSSA(NFU)
      RETURN
      END


C  FILE: GETMAP
C--------------------------------------------------------------------
C  PURPOSE:
C    TO DEFINE THE LINEAR MOTION-MAPS FOR THE INDIVIDUAL
```

```
C     UNIT-SCATTERER LOCATIONS.
C
C   INPUT:
C     ARGUMENTS:
C        XYZ(3,I)      =CARTESIAN COORDS. OF SCATTERER LOCATIONS
C                       IN THE SHIP-CG AXIS SYSTEM.
C        NSCATT        =NUMBER OF SCATTERERS.
C
C   OUTPUT:
C     ARGUMENTS:
C        T             =TRANSFORMATION FROM SHIP-CG 6-DOF POSITION TO
C                       SCATTERER 6-DOF POSITION.
C
C   AUTHOR: D.Y.NORTHAM.
C   DEVELOPED: 4/82.
C   MODIFIED: 1982.
C-------------------------------------------------------------------
      SUBROUTINE GETXAR(XYZ,NSCATT,T)
      DIMENSION XYZ(3,NSCATT),T(3,6,NSCATT)
C
      DO 20 K=1,NSCATT
        DO 10 I=1,3
        DO 10 J=1,3
          T(I,J,K)=0.0
          IF(I.EQ.J) T(I,J,K)=1.0
   10   CONTINUE
        T(1,4,K)=0.0
        T(2,4,K)=-XYZ(3,K)
        T(3,4,K)=XYZ(2,K)
        T(1,5,K)=XYZ(3,K)
        T(2,5,K)=0.0
        T(3,5,K)=-XYZ(1,K)
        T(1,6,K)=-XYZ(2,K)
        T(2,6,K)=XYZ(1,K)
        T(3,6,K)=0.0
   20 CONTINUE
      RETURN
      END


C  FILE: TRNSFR
C-------------------------------------------------------------------
C  PURPOSE:
C    TO OBTAIN THE COORDINATES OF THE ITH SCATTERER IN
C    THE RADAR AXIS-SYSTEM.
C
C  INPUT:
C    ARGUMENTS:
C      RI       =SCATTERER COORDINATES IN THE SHIP-CG AXIS SYSTEM.
C      XSHIP    =SHIP-CG, 6-DOF POSITION DUE TO MANEUVERING.
C      RADHGT   =HEIGHT OF THE RADAR ABOVE THE SEA.
C
C  OUTPUT:
C    ARGUMENTS:
C      DELRI    =RADAR AXIS-SYSTEM COORDS. OF THE ITH SCATTERER (I*4).
C
C  AUTHOR: D.Y.NORTHAM.
```

```
C   DEVELOPED: 1982.
C   MODIFIED: 1982.
C---------------------------------------------------------------
      SUBROUTINE TRNSFR(RI,XSHIP,RADHGT,DBLRI)
      DOUBLE PRECISION DBLRI
      DIMENSION RI(3),XSHIP(6),A(3,3),DBLRI(3),Y(3)
C
      SPHI=SIN(XSHIP(4))
      CPHI=COS(XSHIP(4))
      STHE=SIN(XSHIP(5))
      CTHE=COS(XSHIP(5))
      SPSI=SIN(XSHIP(6))
      CPSI=COS(XSHIP(6))
C
      A(1,1)=CPSI*CTHE
      A(1,2)=CPSI*STHE*SPHI-SPSI*CPHI
      A(1,3)=CPSI*STHE*CPHI+SPSI*SPHI
      A(2,1)=SPSI*CTHE
      A(2,2)=SPSI*STHE*SPHI+CPSI*CPHI
      A(2,3)=SPSI*STHE*CPHI-CPSI*SPHI
      A(3,1)=-STHE
      A(3,2)=CTHE*SPHI
      A(3,3)=CTHE*CPHI
C
C   POSITION DUE TO SEA MOTION
      DO 20 I=1,3
        Y(I)=0.0
        DO 10 J=1,3
          Y(I)=Y(I)+A(I,J)*RI(J)
   10   CONTINUE
   20 CONTINUE
C
C   POSITION DUE TO MANEUVERING
      DO 30 I=1,3
        DBLRI(I)=Y(I)+XSHIP(I)
   30 CONTINUE
C
C   CORRECT FOR RADAR BEING ABOVE THE EARTH
      DBLRI(3)=DBLRI(3)-RADHGT
C
      RETURN
      END


C   FILE: LINMAP
C---------------------------------------------------------------
C   PURPOSE:
C     TO LINEARLY TRANSFORM AN INPUT VECTOR INTO AN OUTPUT VECTOR.
C
C   INPUT:
C     ARGUMENTS:
C       A             =TRANSFORMATION MATRIX.
C       NROWA         =NUMBER OF ROWS IN 'A'.
C       NCOLA         =NUMBER OF COLUMNS IN 'A'.
C       X             =VECTOR TO BE TRANSFORMED.
C
C   OUTPUT:
```

103

```
C     ARGUMENTS:
C         Y              =RESULTANT VECTOR.
C
C  AUTHOR: D.Y.NORTHAM.
C  DEVELOPED: 4/82.
C  MODIFIED: 1982.
C----------------------------------------------------------------
      SUBROUTINE LINMAP(A,NROWA,NCOLA,X,Y)
C     DIMENSION A(NROWA,NCOLA),X(NCOLA),Y(NROWA)
      DIMENSION A(3,6),X(6),Y(3)
C
      DO 20 I=1,NROWA
        Y(I)=0.0
        DO 10 J=1,NCOLA
          Y(I)=Y(I)+A(I,J)*X(J)
   10   CONTINUE
   20 CONTINUE
      RETURN
      END


C  FILE: SIGNLS
C----------------------------------------------------------------
C  PURPOSE:
C     TO CALCULATE THE RECEIVED RADAR-SIGNALS.
C
C  INPUT:
C     ARGUMENTS:
C        PSI            =SHIP'S ASPECT ANGLE.
C        NSCATT         =NUMBER OF UNIT-SCATTERERS
C        SCTTYP         =FLAG INDICATING THE TYPE OF SCATTERER.
C                       =0 FOR CONSTANT.
C                       =1 FOR FLAT PLATE.
C        DIAM           =DIAMETER OF THE FLAT PLATES.
C        PHI            =ROLL ANGLE OF THE SHIP.
C        WAVLEN         =RADAR WAVELENGTH.
C        DRLRI          =POSITION VECTOR OF THE ITH SCATTERER, IN EARTH COORDS.
C        XSHIP          =POSITION VECTOR OF THE SHIP, IN EARTH COORDINATES.
C        MPFLAG         =MULTIPATH FLAG.
C                       =.TRUE. IF MULTIPATH EFFECTS ARE TO BE CALCULATED.
C                       =.FALSE. OTHERWISE.
C        AMP            =AMPLITUDE OF THE ITH SCATTERER.
C
C  OUTPUT:
C     ARGUMENTS:
C        RCS            =TARGET RCS
C        AZGLNT         =TARGET AZIMUTH-GLINT
C        ELGLNT         =TARGET ELEVATION-GLINT
C
C  AUTHOR: D.Y.NORTHAM.
C  DEVELOPED: 4/82.
C  MODIFIED: 1982, 1983.
C----------------------------------------------------------------
      SUBROUTINE SIGNLS(PSI,NSCATT,SCTTYP,DIAM,PHI,WAVLEN,DRLRI,XSHIP,
     *                  RCS,AZGLNT,ELGLNT,MPFLAG)
$INSERT RCS>ROUTINES>SIZE
$INSERT RCS>ROUTINES>BLOCK1
```

```
$INSERT RCS>ROUTINES>BLOCK2
      DOUBLE PRECISION DP,RATIO,RANGE,DX,DY,DZ
      DOUBLE PRECISION DBLRI
      INTEGER*4 ISEED
      INTEGER SCTTYP(DIMEN)
      LOGICAL MPFLAG
      DIMENSION RANGE(DIMEN2),DBLRI(3,DIMEN),A(DIMEN2),XSHIP(6),
     *          PSI(DIMEN),DIAM(DIMEN),PHASE(DIMEN2),GRDRNG(DIMEN)
      PARAMETER (TWOPI=6.2832)
      DATA ISEED/10.0/
C
C   CALCULATE RADAR-TO-SCATTERER RANGES
      WAVNUM=TWOPI/WAVLEN
      RSHIP=SQRT(XSHIP(1)**2+XSHIP(2)**2+XSHIP(3)**2)
      DO 10 I=1,NSCATT
         DX=DBLRI(1,I)
         DY=DBLRI(2,I)
         DZ=DBLRI(3,I)
         DW=RNGERR*RANDSA(ISEED)
         GNDRNG(I)=DSQRT(DX**2+DY**2)+DW
         RANGE(I)=DSQRT(DX**2+DY**2+DZ**2)+DW
         IF(MPFLAG) RANGE(I+NSCATT)=
     *              DSQRT(DX**2+DY**2+(XYZ(3,I)+XSHIP(3)-RADHGT)**2)+DW
   10 CONTINUE
      SUM1=0.0
      SUM2=0.0
      SUM3=0.0
      IF(MPFLAG) NPTS=2*NSCATT
      IF(.NOT.MPFLAG) NPTS=NSCATT
C
C   CALCULATE SCATTERING AMPLITUDES
      DO 15 J=1,NSCATT
         A(J)=AMP(J)
         IF(SCTTYP(J).EQ.2) CALL FLTPLT(DIAM(J),WAVNUM,PSI(J),PHI,A(J))
         IF(.NOT.MPFLAG) GO TO 13
C
C   CALCULATE MULTIPATH AMPLITUDE AND PHASE EFFECTS
         TARHGT=XSHIP(3)+XYZ(3,J)
         CALL MPMAIN(J,TARHGT,RADHGT,GNDRNG(J),TIME,PSISPC,XREAL,XIMAG)
         F1=SQRT((1.0+XREAL)**2+XIMAG**2)
         F2=F1*SQRT(XREAL**2+XIMAG**2)
         A(J+NSCATT)=F2*A(J)
         A(J)=F1*A(J)
         PHASE(J)=ATAN2(XIMAG,1.0+XREAL)
         PHASE(J+NSCATT)=ATAN2(XIMAG*(1.0+2.0*XREAL),XREAL+XREAL**2-
     *                   XIMAG**2)
         GO TO 15
   13    PHASE(J)=0.0
   15 CONTINUE
C
C   CALCULATE RCS AND GLINT
      DO 25 I=1,NPTS
         IF(I.LE.NSCATT) I1=I
         IF(I.GT.NSCATT) I1=I-NSCATT
         AZCOEF=(XSHIP(2)*DBLRI(1,I1))/RANGE(I)
     *          -(XSHIP(1)*DBLRI(2,I1))/RANGE(I)
         DO 25 J=1,NPTS
```

```
          IF(J.LE.NSCATT) GO TO 21
            J1=J-NSCATT
            RZI=-(XSHIP(3)+DBLFI(3,J)+RADHGT)
            GO TO 22
   21     J1=J
          RZI=DBLRI(3,J)
   22     CONTINUE
          ELCOEF=RZI*(DBLRI(1,J1)*DBLRI(1,I1)+DBLRI(2,J1)*
      *            DBLRI(2,I1))/(RANGE(I)*(RANGE(J)**2))
C
C  CALCULATE PHASE DUE TO RANGE
          DR=RANGE(I)-RANGE(J)
          RATIO=DR/WAVLEN
          ANGLE=2.0*TWOPI*(RATIO-DINT(RATIO))
C
C  ADD MULTIPATH PHASE
          ANGLE=ANGLE+PHASE(I)-PHASE(J)
C
C  CALCULATE SUMMATION TERMS
          TERM=A(I)*A(J)*COS(ANGLE)
          SUM1=SUM1+TERM*ELCOEF
          SUM2=SUM2+TERM*AZCOEF
          SUM3=SUM3+TERM
   25 CONTINUE
      SUM3=SUM3+1.0E-10
      RCS=SUM3
C
C  CALCULATE GLINT IN METERS
      AZGLNT=SUM2/SUM3
      ELGLNT=RSHIP*SUM1/SUM3 - (XSHIP(3)-RADHGT)
      RETURN
      END


C  FILE: FLTPLT
C------------------------------------------------------------------------
C  PURPOSE:
C    TO CALCULATE A FLAT-PLATE-TYPE AMPLITUDE AT
C    NEAR-PERPENDICULAR INCIDENCE.
C
C  INPUT:
C    ARGUMENTS:
C       DIAM    =DIAMETERS OF THE PLATES.
C       WAVNUM  =WAVE NUMBER FOR THE RADAR.
C       AZIMTH  =RADAR-TO-PLATE AZIMUTH ANGLE.
C       ELEV    =RADAR-TO-PLATE ELEVATION ANGLE.
C
C  OUTPUT:
C    ARGUMENTS:
C       AMP     =RESULTING SCATTERED AMPLITUDE.
C
C  AUTHOR: D.Y.NORTHAM.
C  DEVELOPED: 4/82.
C  MODIFIED: 1982.
C------------------------------------------------------------------------
      SUBROUTINE FLTPLT(DIAM,WAVNUM,AZIMTH,ELEV,AMP)
      PARAMETER (TWOPI=6.2832,SQRTPI=1.77245,PION2=1.5708)
```

```
C
      C1=WAVNUM*(DIAM**2)/SQRTPI
C
C CALCULATE AZIMUTH COMPONENT
      IF(AZIMTH.NE.0.0) GO TO 15
        AZMAMP=1.0
        GO TO 20
   15 C2=WAVNUM*DIAM*SIN(AZIMTH-PION2)
      AZMAMP=ABS(SIN(C2)/C2)
C
C CALCULATE ELEVATION COMPONENT
   20 IF(ELEV.NE.0.0) GO TO 25
        ELEAMP=1.0
        GO TO 30
   25 C3=WAVNUM*DIAM*SIN(ELEV)
      ELEAMP=ABS(SIN(C3)/C3)
C
C CALCULATE TOTAL AMPLITUDE
   30 AMP=C1*SQRT(ELEAMP*AZMAMP)
      RETURN
      END


C FILE: SHIP
C--------------------------------------------------------------------
C PURPOSE:
C   TO CALCULATE THE MANEUVERING TRAJECTORY OF THE SHIP
C   IN EARTH COORDINATES.
C
C INPUT:
C   ARGUMENTS:
C     TIME        =CURRENT SIMULATION TIME.
C
C OUTPUT:
C   ARGUMENTS:
C     XSHIP       =EARTH COORDINATES OF THE SHIP DUE TO MANEUVERING.
C
C AUTHOR: D.Y.NORTHAM.
C DEVELOPED: 1982.
C MODIFIED: 1982, 1983.
C--------------------------------------------------------------------
      SUBROUTINE SHIP(TIME,XSHIP)
      LOGICAL FIRST
      DIMENSION XSHIP(6)
      DATA XO,YO,ZO,VX,VY,VZ/6*0.0/,FIRST/.TRUE./,OMEGA,PSIO/2*0.0/
C
      IF(.NOT.FIRST) GO TO 10
        FIRST=.FALSE.
    5   CALL TNOUA('ENTER INITIAL SHIP COORDS: ',27)
        READ(1,*,ERR=5) XO,YO,ZO
    7   CALL TNOUA('ENTER SHIP SPEED: ',18)
        READ(1,*,ERR=7) V
    8   CALL TNOUA('ENTER INITIAL SHIP ROTATION ANGLE (DEG): ',41)
        READ(1,*,ERR=8) PSIO
        PSIO=PSIO/57.3
        VX=V*COS(PSIO)
        VY=V*SIN(PSIO)
```

107

```
      9   CALL INCUA('ENTER SHIP TURNING RATE (RAD): ',31)
          READ(1,*,ERR=9) OMEGA
     10 XSHIP(1)=X0+VX*TIME
        XSHIP(2)=Y0+VY*TIME
        XSHIP(3)=Z0+VZ*TIME
        XSHIP(4)=0.0
        XSHIP(5)=0.0
        XSHIP(6)=PSIO+OMEGA*TIME
        RETURN
        END


C  FILE: ASPECT
C-----------------------------------------------------------------
C  PURPOSE:
C    TO CALCULATE A SCATTERER'S ASPECT ANGLE RELATIVE TO THE RADAR.
C
C  INPUT:
C    ARGUMENTS:
C       X        =X-COORDINATE OF THE SCATTERER.
C       Y        =Y-COORDINATE OF THE SCATTERER.
C       PSI      =SHIP ROTATION ANGLE.
C       SCTNUM   =INDEX TO THE SCATTERERS (I).
C       FIRST    =FIRST-PASS FLAG.
C                =.TRUE. FOR THE FIRST PASS THROUGH THE SIMULATION.
C                =.FALSE. OTHERWISE.
C
C  OUTPUT:
C    ARGUMENTS:
C       ASPECT   =SCATTERER'S ASPECT ANGLE (RAD).
C
C  AUTHOR: D.Y.NORTHAM.
C  DEVELOPED: 4/82.
C  MODIFIED: 1982.
C-----------------------------------------------------------------
        FUNCTION ASPECT(X,Y,PSI,SCTNUM,FIRST)
$INSERT PCS>ROUTINES>SIZE
        LOGICAL FIRST
        INTEGER*4 ISEED
        INTEGER SCTNUM
        DIMENSION ASPCTO(DIMEN)
        PARAMETER (DEGREE=2.0)
        DATA ASPCTO/DIMEN*0.0/,ISEED/1/
C
C  ASSIGN RANDOM INITIAL ASPECT
        IF(.NOT.FIRST) GO TO 10
           ASPCTO(SCTNUM)=2.0*(RANDSA(ISEED)-0.5)*(DEGREE/57.296)
C
C  CALCULATE ASPECT
     10 ASPECT=ASPCTO(SCTNUM)+PSI+ATAN2(Y,X)
     20 RETURN
        END


C  FILE: PROCES
C-----------------------------------------------------------------
C  PURPOSE:
```

```
C     TO REALIZE THE SHIP-CG MOTION PROCESSES.
C
C  INPUT:
C    ARGUMENTS:
C       II       =INDEX TO THE SHIP-CG PROCESSES.
C       CNTFRQ   =CENTER FREQUENCIES OF THE SPECTRA (RAD/S).
C       BNDWTH   =BANDWIDTHS OF THE SPECTRA (RAD/S).
C       ISEED    =RANDOM NUMBER GENERATOR SEEDS (I*4).
C       FIRST    =FIRST-PASS FLAG.
C                =.TRUE. FOR THE FIRST PASS THROUGH THE SIMULATION.
C                =.FALSE. OTHERWISE.
C       TIME     =CURRENT SIMULATION TIME (S).
C
C  OUTPUT:
C    ARGUMENTS:
C       RNDVAR   =CURRENT VALUE OF THE DESIRED PROCESS.
C
C  AUTHOR: D.Y.NORTHAM.
C  DEVELOPED: 4/82.
C  MODIFIED: 1982.
C-----------------------------------------------------------------
      SUBROUTINE PROCES(II,CNTFRQ,BNDWTH,ISEED,FIRST,RNDVAR,TIME)
      PARAMETER (TWOPI=6.2832,RMSFAC=0.4499,MAXFRQ=31)
      LOGICAL FIRST
      INTEGER*4 ISEED
      COMMON/RVBLK/S(MAXFRQ,6),W(MAXFRQ,6),DW(6),PHI(MAXFRQ,6),
     *             PARAMS(10),NFREQ(6)
C
      IF(.NOT.FIRST) GO TO 100
C
C  INITIALIZE RANDOM PHASES
      DO 5 I=1,MAXFRQ
        PHI(I,II)=TWOPI*RANDSA(ISEED)
    5 CONTINUE
C
C  INITIALIZE PARAMETERS
      PARAMS(1)=CNTFRQ
      PARAMS(2)=BNDWTH
      WMIN=CNTFRQ-BNDWTH
      PARAMS(3)=WMIN
      NFREQ(II)=MAXFRQ
      DW(II)=BNDWTH/10.
C
C  CALCULATE THE SPECTRA
      CALL SPCTRM(1,PARAMS,NFREQ(II),DW(II),W(1,II),S(1,II))
C
C  STORE NORMALIZED SPECTRUM
      MAX=NFREQ(II)
      DO 20 I=1,MAX
        S(I,II)=SQRT(2.0*S(I,II)*DW(II))
   20 CONTINUE
      GO TO 200
C
C  CALCULATE THE CURRENT VALUE OF THE PROCESS
  100 SUM=0.0
      MAX=NFREQ(II)
      DO 110 I=1,MAX
```

```
       COSINE=COS(PHI(I,II)+W(I,II)*TIME)
       SUM=SUM+S(I,II)*COSINE
110 CONTINUE
    ENDVAR=RMSFAC*SUM
200 RETURN
    END


C  FILE: SPCTRM
C-------------------------------------------------------------------------
C  PURPOSE:
C    TO GENERATE THE SPECTRUM OF A PROCESS OVER A RANGE OF
C    POSITIVE FREQUENCIES.
C
C  INPUT:
C    ARGUMENTS:
C      TYPE        =FLAG INDICATING TYPE OF SPECTRUM TO BE GENERATED (I).
C      PARAMS(1)   =CENTER FREQUENCY OF THE (UNIMODAL) SPECTRUM (RAD/S).
C      PARAMS(2)   =BANDWIDTH OF THE SPECTRUM (RAD/S).
C      PARAMS(3)   =LOWEST FREQUENCY AT WHICH THE SPECTRUM IS
C                   TO BE CALCULATED.
C      NFREQ       =NUMBER OF FREQUENCIES AT WHICH THE SPECTRUM
C                   IS TO BE CALCULATED.
C      DW          =FREQUENCY INCREMENT (RAD/S).
C
C  OUTPUT:
C    ARGUMENTS:
C      W           =FREQUENCIES AT WHICH THE SPECTRUM IS CALCULATED (RAD/S).
C      S           =VALUES OF THE SPECTRUM.
C
C  AUTHOR: D.Y.NORTHAM.
C  DEVELOPED: 4/82.
C  MODIFIED: 1982.
C-------------------------------------------------------------------------
       SUBROUTINE SPCTRM(TYPE,PARAMS,NFREQ,DW,W,S)
       INTEGER TYPE
       DIMENSION PARAMS(1),S(1),W(1)
C
       GO TO (10), TYPE
       WRITE(1,1) TYPE
    1  FORMAT('NO SPECTRUM DEFINED FOR TYPE=',I2,' (SPCTRM).')
       GO TO 20
C
C  BANDPASS SPECTRUM
    10 CNTFRQ=PARAMS(1)
       BNDWTH=PARAMS(2)
       WMIN=PARAMS(3)
       ALPHA=BNDWTH/2.0
       DO 15 I=1,NFREQ
         W(I)=WMIN+(I-1)*DW
         S(I)=ALPHA/(ALPHA**2+(W(I)-CNTFRQ)**2)
         S(I)=S(I)+ALPHA/(ALPHA**2+(W(I)+CNTFRQ)**2)
         S(I)=2.0*S(I)
    15 CONTINUE
    20 RETURN
       END
```

REFERENCES

1. J.W. Crispin, Jr., A.L. Maffett, and T.B. Cruz, "RCS Calculation of Complex Shapes—Methods," in *Methods of Radar Cross-Section Analysis*, J.W. Crispin, Jr. and K.M. Siegel, eds. (Academic Press, New York, 1968), Ch. 9.

2. N.A. Logan, "Survey of Some Early Studies of the Scattering of Plane Waves by a Sphere," Proc. *IEEE* 53 (8), 773-785 (Aug. 1965).

3. J.W. Crispin, Jr. and A.L. Maffett, "The Practical Problem of Radar Cross-Section Analysis," *IEEE Trans.* AES7 (Correspondence), 392-395 (March 1971).

4. C.G. Bachman, *Radar Targets* (Lexington Books, 1982).

5. J.W. Wright and A.H. Haddad, "On the Statistical Modeling of Radar Targets," U.S. Army Missile Command, Tech. Report No. RE-72-19, Nov. 1972.

6. J.I. Marcum, "A Statistical Theory of Target Detection by a Pulsed Radar," The Rand Corp., Santa Monica, CA, Report No. RM-754, Dec. 1947.

7. P. Swerling, "Probability of Detection for Fluctuating Targets," The Rand Corp., Santa Barbara, CA, Rand Memo-1217, March 1954.

8. P. Swerling, "Detection of Fluctuating Pulsed Signals in the Presence of Noise," *IRE Trans. on IT* 3, 175-178 (Sept. 1957).

9. Special Issue on Radar Reflectivity, Proc. *IEEE* 53 (Aug. 1965).

10. "Target Considerations," in *Guidance*, A.S. Locke et al., eds. (D. Van Nostrand, 1955), pp. 435-444, Ch. 11.

11. R.H. De Lano, "A Theory of Target Glint or Angular Scintillation in Radar Tracking," Proc. *IRE* 41, 1778-1784 (Dec. 1953).

12. D. Howard, "Radar Target Angular Scintillation in Tracking and Guidance Systems Based on Echo Signal Phase Front Distortion," Proc. of *Nat. Elec. Conf.* 15, 840-849 (Oct. 13-15, 1959).

13. R.B. Muchmore, "Aircraft Scintillation Spectra," *IRE Trans.* AP-8 (1), 201 (Jan. 1960).

14. R.B. Muchmore, "Reply to Comments by Leon Peters, Jr., and F.C. Weimer," *IRE Trans.* AP-9, 112-114 (March 1961).

15. L. Peters, Jr. and F.C. Weimer, "Concerning the Assumption of Random Distribution of Scatterers as a Model of an Aircraft for Tracking Radars," *IRE Trans.* AP-9, 110-111 (Jan. 1961).

16. L. Peters, Jr. and F.C. Weimer, "Reply to Comments by R.H. De Lano," *IRE Trans.* AP-9, 228 (March 1961).

17. L. Peters, Jr. and F.C. Weimer, "Reply to Comments by R.B. Muchmore," *IRE Trans.* AP-9, 229 (March 1961).

18. N.S. Gubonin, "Fluctuation of the Phase Front of the Wave Reflected From a Complex Target," *Radio Engineering and Electron Physics* 10, 718-725 (May 1965).

111

19. M.L. Mumford, "Studies of Radar Target Glint," NWC Tech. Memo-3222, Oct. 1977.

20. N.C. Mohanty, "Modeling Radar Reflections from Randomly Moving Scatterers," Proc. *IEEE* **66** (1), 86-88 (Jan. 1978).

21. W.J. Gruner, ed., "Time-Varying RCS Modeling Algorithms," Teledyne Brown Engineering Tech. Report MSB81-WIC-0033, Dec. 1981.

22. R.L. Mitchell, "Models of Extended Targets and Their Coherent Radar Images," Proc. *IEEE* **62** (6), 754-758 (June 1974).

23. R.L. Mitchell, *Radar Signal Simulation* (Artech House, 1976).

24. M.L. Varshavik, "The Relationship Between the Statistical Amplitude Angles and Phase Characteristics of Signals, Scattered by a Complex Target," *Radio Eng. and Elect. Phys.* **14** (1), 70-76 (1969).

25. B.H. Borden, "A Statistical Glint/RCS Target Model," NWC Tech. Memo 3911/BHB:rlc, Reg 3911-51, 2 June 1981.

26. J.S. Baras, "Statistical Models of Angle Noise for Ship Targets," LOCUS Inc. Report, 14 June 1982.

27. E. Jakeman, "On the Statistics of K-Distributed Noise," *J. Phys. A: Math. Gen.* **13**, 31-48 (1980).

28. E. Jakeman, "A Simple Multiscale Scattering Model," *OPTICA ACTA* **28** (4), 435-441 (1981).

29. E. Jakeman and P.N. Pusey, "The Statistics of Light Scattered by a Random Phase Screen," *J. Phys. A* Math. Gen. **6**, L88-L92 (July 1973).

30. E. Jakeman and P.N. Pusey, "Non-Gaussian Fluctuations in Electromagnetic Radiation Scattered by a Random Phase Screen. 1. Theory," *J. Phys. A: Math. Gen.* **8** (3), 369-391 (1975).

31. E. Jakeman and P.N. Pusey, "A Model for Non-Rayleigh Sea Echo," *IEEE Trans.* AP-24 (6), 806-814 (Nov. 1976).

32. E. Jakeman and P.N. Pusey, "Photon Counting Statistics of Optical Scintillation," in *Inverse Scattering Problems in Optics*, H.P. Baltes, ed. (Springer-Verlag, New York, 1980).

33. J.W. Crispin, Jr. and K.M. Siegel, eds., *Methods of Radar Cross-Section Analysis* (Academic Press, New York, 1968).

34. M.E. Bechtel and R.A. Ross, "Radar Scattering Analysis," Cornell Aeronautical Laboratory Report No. ERIRIS-10, August 1966.

35. J.J. Bowman, T.B.A. Senior, and P.L.E. Uslenghi, eds., *Electromagnetic and Acoustic Scattering by Simple Shapes* (North-Holland, Amsterdam, 1969).

36. G.T. Ruck, D.E. Barrick, W.D. Stuart, and C.K. Kirchbaum, *Radar Cross-Section Handbook*, Vols. 1 and 2 (Plenum Press, 1970).

37. J.B. Keller, "A Geometrical Theory of Diffraction," Proc. of *Symposium in Applied Math* VIII (McGraw-Hill, New York, 1958).

38. F.K. Oshiro, F.P. Torres, and H.C. Heath, "Numerical Procedures for Calculating Radar Cross Section of Arbitrarily Shaped Three-Dimensional Geometries," Air Force Avionics Lab., Tech. Report No. AFAL-TR-66-162, May 1966.

39. F.K. Oshiro, K.M. Mitzner, R.G. Cross, H.C. Heath, T. Gold, and Torres, "Calculation of Radar Cross Section," Air Force Avionics Lab., Tech. Report No. AFAL-TR-67-308, Part 1, Vol. 1, Dec. 1967.

40. H.L. Toothman, "Radar Target Signature Program Performance Specification," NRL Memorandum Report 4515, June 1981.

41. B. Radza and A. Stenger, "Simulation of Ship Radar Signatures," Workshop on Ship Survivability Enhancement by Signature Control, NRL, Dec. 1978.

42. J.E. Lindsay, "Angular Glint and the Moving, Rotating, Complex Radar Target," *IEEE Trans.* AES 4 (2), 164-173 (March 1968).

43. J. Dunn and D. Howard, "Radar Target Amplitude, Angle, and Doppler Scintillation from Analysis of the Echo Signal Propagating in Space," *IEEE Trans.* MTT, 715-728 (Sept. 1968).

44. A.V. Mrstik and P.G. Smith, "Multipath Limitations on Low-Angle Angle Radar Tracking," *IEEE Trans.* AES-14 (1), 85-102 (Jan. 1978).

45. P.G. Smith and A.V. Mrstik, "Multipath Tracking Errors in Elevation-Scanning and Monopulse Radars," *IEEE Trans.* AP-4, 162-167 (Apr. 1956).

46. C.I. Beard, I. Katz, and L.M. Spetner, "Phenomenological Vector Model of Microwave Reflection from the Ocean," *IEEE Trans.* AP-4, 162-167 (Apr. 1956).

47. C.I. Beard and I. Katz, "The Dependence of Microwave Radio Signal Spectra on Ocean Roughness and Wave Spectra," *IRE Trans.* AP-5, 183-191 (Apr. 1957).

48. C.I. Beard, "Coherent and Incoherent Scattering of Microwaves from the Ocean," *IRE Trans.* AP-9, 470-483 (Sep. 1961).

49. D.Y. Northam, "A Stochastic Simulation of Low-Grazing Angle, Forward Scatter, Over-Water Multipath Effects," NRL Report 8568, Feb. 1983.

50. P. Beckman and A. Spizzichino, *The Scattering of Electromagnetic Waves from Rough Surfaces* (Pergamon, New York, 1963).

51. D.K. Barton, "Low-Angle Radar Tracking," Proc. *IEEE* 62, 687-704 (June 1974).

52. J.S. Baras, "Multipath Effects Modeling," LOCUS Inc. Report, 25 Feb. 1980.

53. W-M. Boerner, "Polarization Utilization in Electromagnetic Inverse Scattering," in *Inverse Scattering Problems in Optics*, H.P. Baltes, ed. (Springer-Verlag, New York, 1980).

54. A.L. Maffett, "Scattering Matrices," in *Methods of Radar Cross-Section Analysis*, J.W. Crispin, Jr. and K.M. Siegel, eds. (Academic Press, New York, 1968), Ch. 3.

55. A.V. Alongi, R.E. Kell, and D.J. Newton, "A High Resolution X-Band FM/CW Radar for RCS Measurements," Proc. *IEEE* 53, 1072-1076 (Aug. 1965).

56. A.V. Alongi, R.E. Kell, and D.J. Newton, "A High Resolution X-Band FM/CW Radar for RCS Measurements," Cornell Aeronautical Laboratory Report No. ER/RIS-5, March 1964.

57. "The Delta Radar System—A Wide Bandwidth FM/CW X-Band Radar for RCS Measurements," Cornell Aeronautical Lab., Report No. VB-1571-P-1, 31 July 1962.

58. D.E. Foreman and D.F. Sedivec, "Experimental Observation of the Creeping-Wave Phenomenon in Backscatter Using a Short-Pulse Radar System," Proc. *IEEE* 53, 1102-1104 (Aug. 1965).

59. "Reflectivity Studies of Naval Radar Targets," Naval Missile Center Tech. Publication TP-73-24, Point Magu, CA, Apr. 1973.

60. R.E. Kell, "On the Derivation of Bistatic RCS from Monostatic Measurements," Proc. *IEEE* 53 (8), 983-988 (Aug. 1965).

61. D.R. Brown, R.J. Newman, and J.W. Crispin, Jr., "RCS Enhancement Devices," in *Methods of Radar Cross-Section Analysis*, J.W. Crispin, Jr. and K.M. Seigel, eds. (Academic Press, New York, 1968), Ch. 8.

62. A. Erdelyi, *Asymptotic Expansions* (Dover Publications, New York, 1958).

63. R.D. Kodis, "A Note on the Theory of Scattering from an Irregular Surface," *IEEE Trans.* AP-14 (1), 77-82 (Jan. 1966).

64. C.G. Bachman, "Some Recent Developments in RCS Measurement Techniques," Proc. *IEEE* 53 (8), 962-972 (Aug. 1965).

65. E.M. Kennaugh and D.L. Moffatt, "Transient and Impulse Response Approximations," Proc. *IEEE* 53 (8), 893-901 (Aug. 1965).

66. M.R. Wohlers, S. Hsiao, J. Mendelsohn, and G. Gardner, "Computer Simulation of Synthetic Aperture Radar Images of Three-Dimensional Objects," *IEEE Trans.* AES-16 (3), 258-271 (May 1980).

67. J. Moore, ed., *Janes's Fighting Ships* (Jane's Pub. Co., 1974).

68. M.I. Skolnik, *Introduction to Radar Systems* (McGraw-Hill, New York, 1980).

69. W.E. Norris and E.H. Hackney, "Radar Cross-Section Measurements of a Ship Model," Naval Missile Center Tech. Memo TM68-35, Point Magu, CA, June 1968.

70. R.A. Ross, "Radar Cross Section of Rectangular Flat Planes as a Function of Aspect Angle," *IEEE Trans.* AP 14 (3), 329-335 (May 1966).

71. D.R. Rhodes, *Introduction to Monopulse* (McGraw-Hill, New York, 1959).

72. M.I. Skolnik, ed., *Radar Handbook* (McGraw-Hill, New York, 1970).

73. B.L. Lewis, A.J. Stecca, and D.D. Howard, "The Effect of an Automatic Gain Control on the Tracking Performance of a Monopulse Radar," NRL Report 4796, July 1956.

74. J.S. Baras, Consultant at NRL, personal communication.

75. R.V. Ostrovityanov, "Angular Noise," *Radio Eng. and Elect. Physics* 11 (4), 507-515 (1966).

76. M.L. Varshavchik, "Statistical Characteristics of a Signal Scattered by an Extended Oscillating Body," *Radio Eng. and Elect. Physics* 13 (10), 1531-1534 (1968).

77. F.E. Brooks, Jr., G.P. DuBose, Jr., and C.W. Tolbert, "Preliminary Survey Report of the 1955 Gulf of Mexico Propagation Tests," Electrical Engineering Research Laboratory, University of Texas, Report No. 3-17 (CM-857), 31 Jan. 1956.

78. A.E. Baitis, W.G. Meyers, and T.R. Applebee, "A Non-Aviation Ship Motion Data Base for the DD963, CG26, FF1052, and the FF1040 Ship Classes," David Taylor Naval Ship R&D Center Report SPD-738-01, Dec. 1976.

79. S.L. Bales, A.E. Baitis, and W.G. Meyers, "Rigid Body Ship Responses and Associated Periods for a Series of Liquid Natural Gas (LNG) Ships," David Taylor Naval Ship R&D Center Report SPD-517-04, Apr. 1975.

80. M. St. Denis and W.J. Pierson, "On the Motions of Ships in Confused Seas," *Trans. Soc. Naval Arch. and Marine Eng.*, pp. 280-357 (1953).

81. W. Froude, "On the Rolling of Ships," *Trans. Institution of Naval Architects* 2, 180-229 (1861).

82. A. Krilov, "A New Theory of the Pitching Motion of Ships on Waves and of the Stresses Produced by this Motion," *Trans. Institution of Naval Architects* 37, 326-368 (1896).

83. Z.G. Wachnik and E.E. Farnick, "Ship Motions Prediction in Realistic Short-Crested Seas," *Trans. Soc. of Naval Arch. and Marine Eng.* 73, 100-134 (1965).

84. W.J. Pierson, "A Unified Mathematical Theory for the Analysis, Propagation, and Reflection of Storm Generated Ocean Surface Waves," Parts I and II, New York University College of Engineering Res., Department of Meteorology and Oceanography, 1953.

85. G. Neumann, "On Wave Spectra and a New Method of Forecasting Wind-Generated Sea," Beach Erosion Board, Tech. Memorandum No. 43.

86. C.L. Bretschneider, "Wave Variability and Wave Spectra for Wind Generated Gravity Waves," Dept. of the Army, Corps of Engineers Tech. Memorandum 118 (1959).

87. W.J. Pierson and L. Muskowitz, "A Proposed Spectral Form for Fully Developed Wind Seas Based on the Similarity Theory of S.A. Kitaigorodskii," *Jour. of Geophysical Research* 69 (24), 5181-5190 (1964).

88. P. Levy, "Processus Stochastiques et Movement Brownien," Monographies Des Probabilities, Fascicule VI, Gauthier-Villars, ed. (Paris, 1948).

89. W.J. Pierson, Jr., "Wind-Generated Gravity Waves," in *Advances in Geophysics* 2, 93, H.E. Landsberg, ed. (Academic Press, New York, 1955).

90. S.O. Rice, "Mathematical Analysis of Random Noise," *Bell System Technical Journal* 23, 282-332, 24, 46-156 (1944).

91. E. Wong, *Stochastic Processes in Information and Dynamical Systems* (McGraw-Hill, New York, 1971).

92. H.J.S. Canham, D.E. Cartwright, G.J. Goodrich, and N. Hogben, "Seakeeping Trials on O.W.S. Weather Reporter," *Trans. Royal Inst. Nav. Arch.* **104**, 447 (1962).

93. W.J. Pierson, G. Neumann, and R. James, "Practical Methods for Observing and Forecasting Ocean Waves," Hydrographic Pub. No. 603 (1971).

94. B. Kinsman, *Wind Waves* (Prentice Hall, 1965).

95. A. Papoulis, *Probability, Random Variables, and Stochastic Processes* (McGraw-Hill, New York, 1965).

96. J.S. Baras and D.Y. Northam, "A Statistical-Data Analysis Package; Theoretical Support," (NRL Memorandum Report, forthcoming).

97. J.H. Dunn and D.D. Howard, "Target Noise," in *Radar Handbook*, M. Skolnik, ed. (McGraw-Hill, New York, 1970), Ch. 28.

98. D.Y. Northam, "Users Guide for a Digital Simulation of Over-Water Multipath Effects," NRL Memorandum Report 5020, March 1983.